Università degli studi del Piemonte Orientale

"Amedeo Avogadro"

Dipartimento di Scienze e Innovazione Tecnologica

High-relaxivity systems and molecular imaging probes for Magnetic Resonance Imaging applications

Giuseppe Gambino

PhD supervisor: Prof. Mauro Botta

PhD Co-supervisor: Dr. Lorenzo Tei

A thesis submitted for PhD degree

January 2014

Contents

1. Introduction

1.1 Magnetic Resonance Imaging

Magnetic resonance imaging (MRI) is a powerful and widely used diagnostic tool in modern clinical medicine because of its many advantages as a diagnostic imaging modality. It is noninvasive, delivers non-ionizing radiation, and has excellent (submillimeter) spatial resolution. The soft tissue contrast is good enough to allow MRI to give detailed anatomical information. Moreover, there are many techniques that can provide contrast in MRI, resulting in markedly different images from the same anatomical region. For instance, pulse sequences can be weighted to highlight differences among tissues that have different proton density ρ, T_1 or T_2 relaxation times (Figure 1.1), different rates of water diffusion, or different chemical shifts (water vs lipids). The overriding challenge with MRI is its relatively low sensitivity. Hydrogen atoms from water, present in tissue at ~90 M concentration, are the main observation in clinical imaging. In order to induce additional contrast, a substance is required that will affect some of the properties of the 90 M water protons as much as an observable effect is achieved. Such substances are called MRI contrast agents. They are paramagnetic, superparamagnetic, or ferromagnetic compounds that catalytically shorten the relaxation times of bulk water protons.

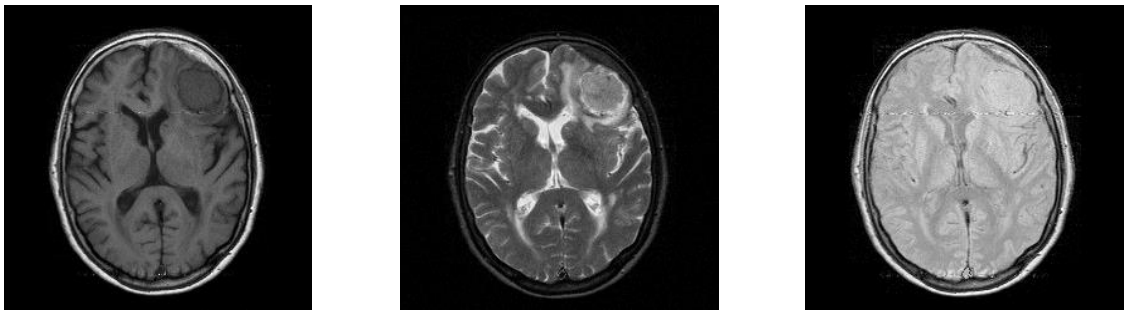

Figure 1.1 T_1 weighted (left), T_2 weighted (centre) and ρ weighted (right) brain images.

All contrast agents shorten both T_1 and T_2. However it is useful to classify MRI contrast agents into two broad groups based on whether the substance increases the transverse relaxation rate ($1/T_2$) by roughly the same amount that it increases the longitudinal relaxation rate ($1/T_1$) or whether $1/T_2$ is altered to a much greater extent. The first category includesas the so-called T_1 agents because, on a percentage basis, these agents alter $1/T_1$ of tissue more than $1/T_2$ owing to the fast endogenous transverse relaxation in tissue. With most pulse sequences, this dominant T_1 lowering effect gives rise to increases in signal intensity; these are positive contrast agents. The T_2 agents largely increase the $1/T_2$ of tissue and cause a reduction in signal intensity; these are negative contrast agents. Paramagnetic gadolinium^{3+} based contrast agents are examples of T_1 agents, while ferromagnetic iron oxide particles are examples of T_2 agents. Although there are some manganese^{2+} and iron-based contrast agents approved for clinical use, the overwhelming majority of contrast enhanced clinical exams are performed with Gd^{3+} complexes.

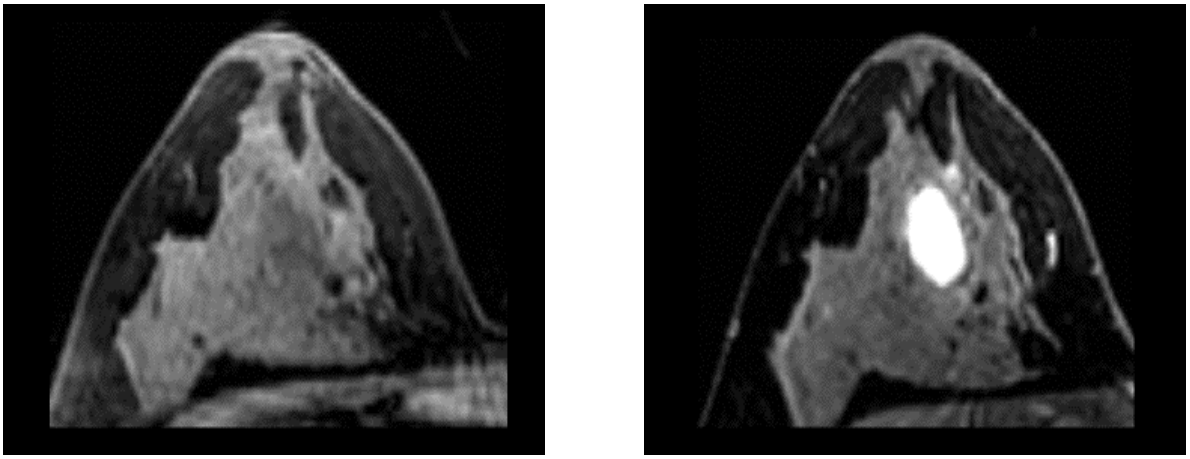

Figure 1.2: MRI images of breast cancer *pre* (left) and *after* (right) contrast agent administration. **[From University of Liverpool website; *http://int.ch.liv.ac.uk/Lanthanide/Ln_Chemistry_folder/MRI%20folder/MRImages.html*]**

More than 10 million MRI studies are performed using Gd^{3+}-based contrast agents each year. It is the action of the contrast agent on the relaxation properties of the water hydrogen nuclei that enhance contrast; this is different from X-ray contrast media and

nuclear imaging agents where the observed effect is more proportional to the concentration of iodine or radionuclide. Since water is present at a much higher concentration than the contrast agent, the latter must act catalytically to relax the water protons in order to observe an effect. The ability of a contrast agent to change a relaxation rate is represented quantitatively as *relaxivity*, r_1 or r_2, where the subscript refers to either the longitudinal ($1/T_1$) or the transverse relaxation rate ($1/T_2$). Relaxivity is simply the change in relaxation rate after the introduction of the contrast agent ($\Delta(1/T_1)$ normalized to the concentration of contrast agent or metal ion [M] (equation 1).

$$r_1 = \frac{\Delta(\frac{1}{T_1})}{[M]} \qquad (1)$$

To enhance the role of MR in molecular and cellular imaging investigations, it is necessary to improve the sensitivity of the involved probes. The sensitivity issue deals with either the intrinsic relaxivity of a given agent or specific features associated with the biological characteristics of the targeting experiments. As far as the intrinsic sensitivity is concerned, the chemist has to design systems endowed with structural and dynamic properties that lead to optimized values for those parameters that are relevant for a given contrast enhancing mechanism. Much work has been done in the last two decades to design structures with high relaxivity; however the theoretical maximum efficiency expected from the optimization of all the parameters involved in the paramagnetic relaxation has not yet been reached. In general, to attain the MR visualization of a given cellular target, one may rely on the exploitation of high-capacity carriers that can be loaded with a huge number of imaging reporters, thus allowing the internalization of a sufficient amount of contrast agent in the target cells. This approach has required the use of macromolecular and supramolecular systems that chemists had primarily developed for the setup of drug delivery experiments. Depending on their characteristics, the carriers may be loaded with commercial Gd agents or specifically tailored probes may need to be prepared in order to be compatible with the structure of the carrier. Interestingly, other than the molecular parameters, it has been envisaged that, for some types of nanocarriers, other contributions may be important for the creation of longitudinal relaxivity values that

would be much higher than the ones that are currently available. These contributions will be discussed in the following chapter.

1.2 Relaxivity, contributions and parameters

The relaxivity enhancement of water protons in aqueous solutions of Gd^{3+} complexes arises from time fluctuation of the dipolar coupling between the electron magnetic moment of the metal ion and the nuclear magnetic moment of the solvent nuclei.

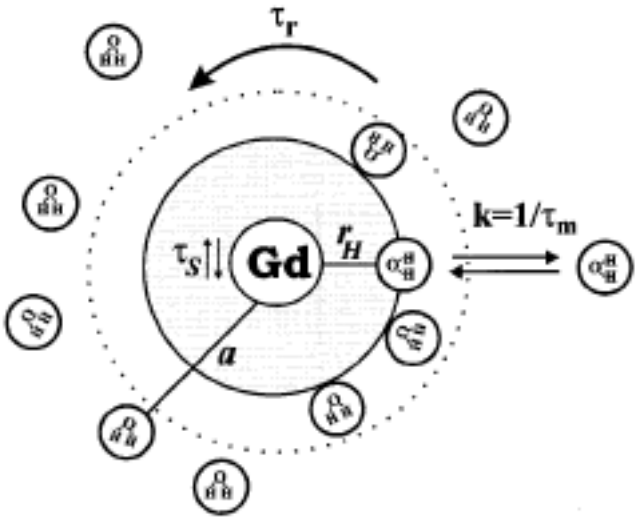

Figure 1.3: Illustration of the three types of hydration layers around a Gd^{3+} complex and the most relevant parameters of paramagnetic relaxation[botta rev2000].

This interaction is traditionally described with a model that considers two contributions (Figure 1.3): inner sphere (IS), due to water molecules present in number q in the coordination sites of the Gd^{3+} ion, and outer sphere (OS), which involves all the solvent molecules diffusing by the complex:

$$R_1^{obs} = R_{1p}^{IS} + R_{1p}^{OS} + R_1^W \qquad (2)$$

where R_1^{obs} is the measured relaxation rate and R_1^W the relaxation rate of the solvent in the absence of the paramagnetic complex.

The inner sphere contribution is the term that most contributes to r_{1p}. This is the reason why large efforts towards contrast agents of improved efficacy have been directed mainly towards its optimization. The large number of experimental data recorded over the last 15 years on small Gd^{3+} chelates have been interpreted on the basis of the Solomom-Bloembergen-Morgan approach, and have provided a good understanding of the role played by the different relaxation parameters, of their mutual relationship, and of their dependence on the structural features of the complexes. The relevant Equations are:

$$R_{1p}^{IS} = \frac{[M]q}{55.6} \frac{1}{T_{1M} + \tau_M} \tag{3}$$

$$\frac{1}{T_{1M}} = \frac{2}{15} \frac{\gamma_H^2 g^2 S(S+1)\beta^2}{r_H^6} \left[\frac{3\tau_{C1}}{1 + \omega_H^2 \tau_{C1}^2} + \frac{7\tau_{C2}}{1 + \omega_S^2 \tau_{C2}^2} \right] \tag{4}$$

$$\frac{1}{\tau_{Ci}} = \frac{1}{\tau_R} + \frac{1}{\tau_M} + \frac{1}{\tau_{Si}} \tag{5}$$

where M is the concentration of the CA, T_{1M} the longitudinal relaxation time of the bound water protons, S is the electron spin quantum number (7/2 for Gd^{3+}), γ_H is the proton nuclear gyromagnetic ratio, β is the Bohr magneton, g is the Landè factor for the free electron, r_H is the distance between the metal ion and the bound water protons; ω_H and ω_S are the proton and electron Larmor frequencies, respectively, and τ_{Ci} (i= 1, 2) are the correlation times of the modulation of the dipolar electron-proton coupling. The overall correlation times τ_{Ci} receive contributions from the reorientation of the paramagnetic species, τ_R, by the residence lifetime of the bound water protons, τ_M and by the electronic relaxation times of the metal ion, τ_S. A marked enhancement of r_{1p} at the magnetic fields currently employed clinically has been primarily obtained by slowing down the molecular tumbling (increasing τ_R) by different approaches.

However, the expected increase of r_{1p} has not been observed because of the limiting effect of the mean water residence lifetime τ_M.[1-5]

A fine tuning of this parameter has emerged as a primary objective of the current research in this field, as only values around 30 ns would allow the full exploitation of the decrease of T_{1M} induced by the lengthening of τ_R.

1.3 Gd^{3+} complexes, an introduction to MRI contrast agents

The sensitivity of a given paramagnetic complex is closely related to its relaxivity (usually measured at 0.5 T and at 298 or 310 K). Relaxivity is the result of a complex interplay between the paramagnetic center's structural, dynamic, and electronic properties. Good estimates of the determinants of the relaxivity of a given paramagnetic complex can be obtained from the analysis of relaxivity data as a function of the applied magnetic field (NMRD profiles). This method gave rise to a prediction that high relaxivities could be attained, at the clinical field strength of 0.5-1.5 T, by lengthening the molecular reorientational time, τ_R.
Therefore, macromolecular systems were addressed by either the covalent or noncovalent binding of paramagnetic chelates to slowly moving substrates. Human serum albumin (HSA), the most abundant protein in serum, has often been an important target for the development of a high-sensitivity agent for magnetic resonance angiography.[6]

The relaxivities observed for HSA adducts were often lower than expected as a consequence of the increase in the residence lifetime (τ_M) of the water molecule at

the metal site.[7] Moreover, it has been recently shown that, in addition to steric hindrance at the coordination metal site, τ_M is strongly modulated by the charge at the metal ion, thus reflecting changes that occur at the level of the donor atoms of the coordination cage.[8]

Thus, the formation of hydrogen bonds between the carboxylic groups of the ligand and basic amino acids on the surface of the protein may result in a significant release of the residual electric charge on the complex that, in turn, yields a marked elongation of the exchange lifetime of the coordinated water molecule(s). Of course, the coordinated water itself may be involved in H-bond formation that directly affects its dissociation kinetics. Thus, upon binding to a protein (or more generally to a macromolecular substrate), the relaxivity of a given paramagnetic complex may vary as a consequence not only of τ_R but also of τ_M. Both parameters are site-dependent. In fact, the complex very seldom assumes the molecular reorientational time of the macromolecule, but rather it experiences a faster reorientation motion superimposed onto the slower motion of the supramolecular adduct. Clearly, the "pincer attack" of the complex at two binding sites endows the system with the τ_R of the macromolecule as shown by Caravan and co-workers.[9]

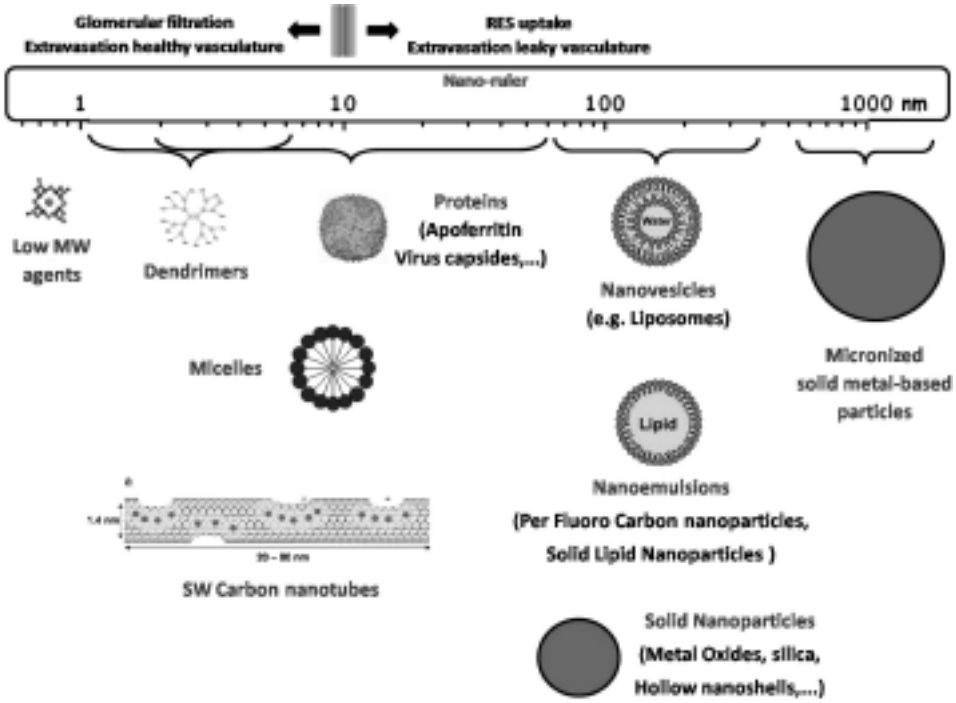

Figure 1.4: Average size of the nanocarriers considered so far for developing highly sensitive Gd(III)-based MRI agents. ***[Aime et al. Vol. 42, No. 7 July 2009 822-831 ACCOUNTS OF CHEMICAL RESEARCH 823]***

Another issue related to the overall sensitivity of Gd^{3+}-based probes is the "clustering" effect. Some years ago, Merbach and co-workers showed that the dilution of Gd^{3+} chelates with diamagnetic Y^{3+} complexes at the surface of micelles resulted in an enhanced relaxivity. [10]

The observed behavior was ascribed to the occurrence of dipolar interactions among the Gd^{3+} ions able to enhance the electronic relaxation rate that, in turn, causes the decrease of the observed relaxation rate in neat Gd^{3+}-containing micelles.

The link between relaxivity and local concentration has also been recently tackled by Sherry and co-workers, who used a Gd-DO3A-peptide chimera able to bind anti-FLAG monoclonal antibodies. [11] The relaxivity of the supramolecular Gd-DO3A-antibody adduct was only ~17 mM^{-1} s^{-1} (likely due to a long τ_M), and the system was MR silent at concentrations below ~9 μM. However, when the antibodies were clustered together to form microdomains of high local concentration at the surface of agarose beads, the MR detection limit of the agent improved down to 4 μM. On the basis of simulated data, the authors concluded that the detection limit of a single highly efficient low molecular weight Gd^{3+} agent (relaxivity of 100 mM^{-1} s^{-1}) targeted in a protein microdomain is ~0.7 μM at 9.4 T, thus suggesting that small sized agents could still have a future in MR molecular imaging applications.

1.4 Enhancing MRI CAs efficiency

Extracellular MRI contrast agents like Magnevist® ($[Gd(DTPA)(H_2O)]^{2-}$ (Figure 1.5) are cheap to produce and have an excellent safety profile. Doses as high as 0.3 mmol kg^{-1} are given clinically for angiography and cerebral perfusion applications. At these doses, T_1 in the presence of contrast agent is much shorter than T_1 in any other tissue and therefore contrast is excellent. The drive for higher relaxivity doesn't come from making a better Magnevist, whereas from increasing the sensitivity of MRI to detect molecular targets.

In order to induce observable contrast in a robust clinical exam, a relaxation rate change of at least 0.5 s^{-1} is required. For extracellular commercial contrast agents with a relaxivity of ~4 mM^{-1} s^{-1} , this means a concentration of ~125 mM. For targeted imaging and assuming a 1 : 1 binding stoichiometry (Gd : target molecule), this would require a biological target present with a concentration at least 125 mM.

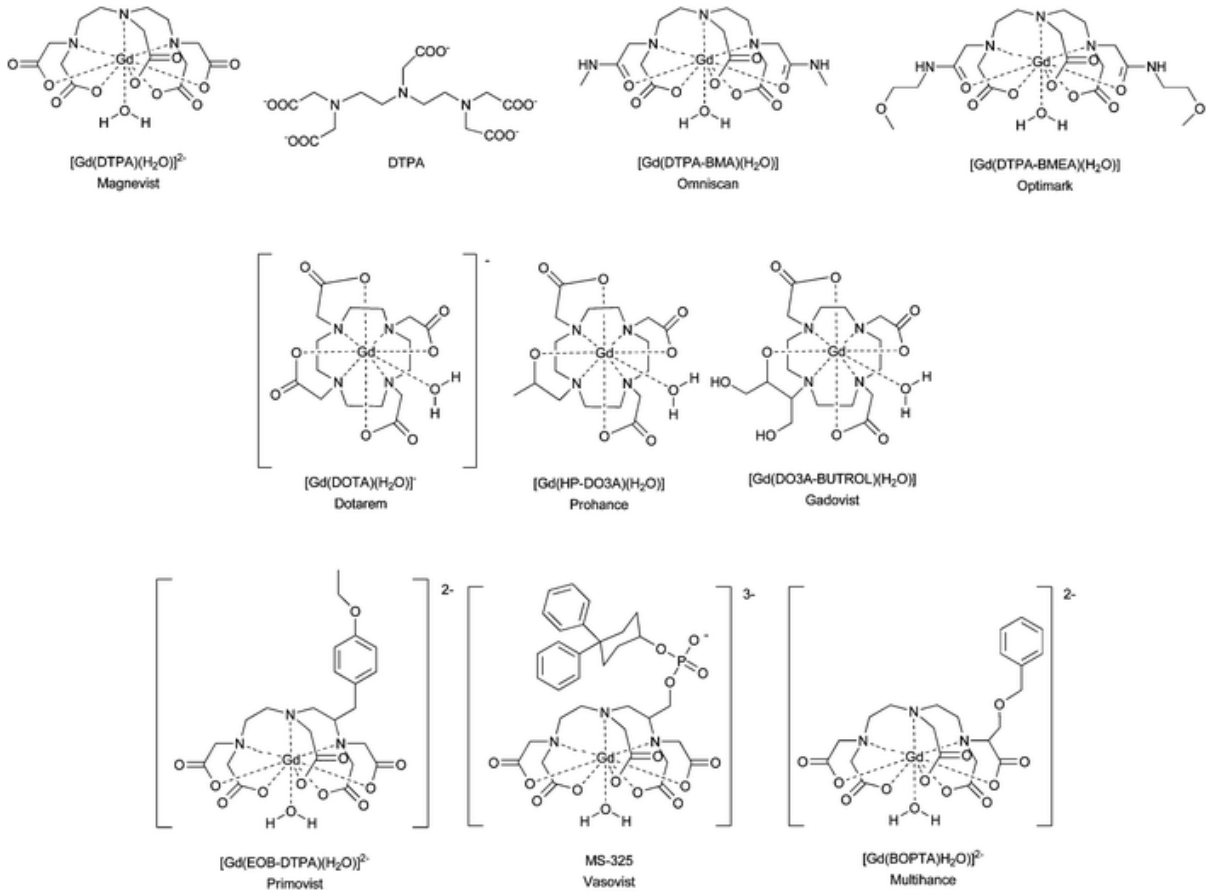

Figure 1.5: Some commercial MRI CAs.

For absolute sensitivity, a more rigorous analysis by Wedeking et al. gave a limit of detection of 30 mM in mouse skeletal muscle for the contrast agent Gd(HPDO3A)(H2O)]. This limits the number of potential biological targets for imaging using current technology. In order to achieve sufficient T_1 change, relaxivity and/or the number of Gd/molecule should be increased. Being relaxivity so dependent on molecular motion, molecular size, rigidity, and a possible protein binding, it must be optimized on a case by case basis. There is no ''high relaxivity'' gadolinium complex that can be conjugated to a targeting vector that will necessarily

give a targeted contrast agent with high relaxivity. The rotational dynamics of the final molecule are critical and there are a lot of ways to obtain a MRI contrast agent suitable for molecular targeting taking advantage of this parameter.

Water proton relaxation by Gd^{3+} occurs via a dipolar mechanism and as such has a $1/r^6$ dependence on the distance between the ion and the nucleus, as described in equation (4). Because of this, it is critical to have one or more exchangeable waters in the inner coordination sphere. However if the hydration number, *q*, is greater than one then the complex should be stable with respect to water displacement by endogenous ligands.

Ultimately for in vivo use, the complex must be stable and kinetically inert with respect to gadolinium loss. Water exchange in and out of the first coordination sphere should be fast. In order to increase the relaxation rate of bulk solvent two things must occur: the paramagnetic ion should efficiently relax the water that comes into contact with it, and the relaxed water should exchange rapidly with the bulk water.

For fast tumbling complexes such as $[Gd(DTPA)(H_2O)]^{2-}$, it is relaxation of the bound water that is the rate limiting process. Water exchange becomes important when rotational motion is slowed. Gadolinium complexes with amide oxygen donor atoms have typically slower water exchange rates. [12]

The gadolinium complex of the bis(N-methyl)amide analog of DTPA, [Gd(DTPA-BMA)(H_2O)], has a water exchange rate about 10 times slower than that of $[Gd(DTPA)(H_2O)]^{-2}$. In the presence of serum albumin, both complexes bind with it, resulting in much slower tumbling and a more efficient relaxation mechanism of the bound water. Now the relative importance of water exchange becomes significant and the slow water exchange at the GdDTPA-BMA derivative limits its relaxivity. Increasing water exchange may improve relaxivity further, but only if the process for relaxing the bound water is very efficient.

For most biological targets of interest for imaging, multiple gadolinium ions are required to provide the necessary relaxation rate change. Linking multiple complexes together necessarily increases the effective correlation time for motion.

However, understanding and controlling rotational flexibility has a large impact on the resultant relaxivity. Linking complexes in a linear fashion gives an oligomer with anisotropic rotation where rotation about the short axis of the molecule is fast and limits relaxivity. Dendrimers linked to gadolinium complexes usually have higher relaxivity because the dendritic structure imposes a more isotropic rotational dynamic optimizing the effect of the increased molecular weight on relaxivity. The different types of motion are illustrated in Figure 1.6.

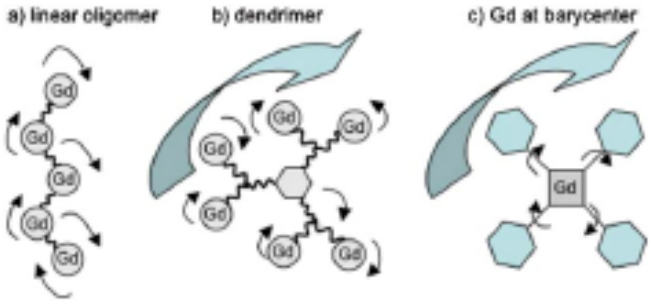

Figure 1.6: Different constructs for increasing relaxivity. a) Linear polymer increases the number of Gd per molecule but low relaxivity because of flexibility/internal motion. b) Dendrimer increases the number of Gd per molecule and introduces more globular structure, slowing rotation and increasing relaxivity; internal motion still present. c) Monomer with Gd at barycenter of molecule; although the non-Gd containing arms are free to rotate, the Gd can only rotate at the rate of the entire molecule resulting in high relaxivity. ***[Caravan, Chem. Soc. Rev., 2006, 35, 512–523]***

An example of a linear polymer is that described by Casali *et al.*[13] who reported a modified dextran polymer with DOTA-monoamide chelates with a total molecular weight of 52 kDa. The per-gadolinium relaxivity of this multimeric compound was 10.6 mM^{-1} s^{-1} (37 °C, 0.47 tesla). The same type of gadolinium chelate appended 24 times to a polyamide dendrimer gives the compound Gadomer (also called Gadomer-17 because of its 17 kDa molecular weight). Under similar conditions (40 °C, 0.47 tesla), Gadomer has a relaxivity of 16.5 mM^{-1} s^{-1} per gadolinium.[14]

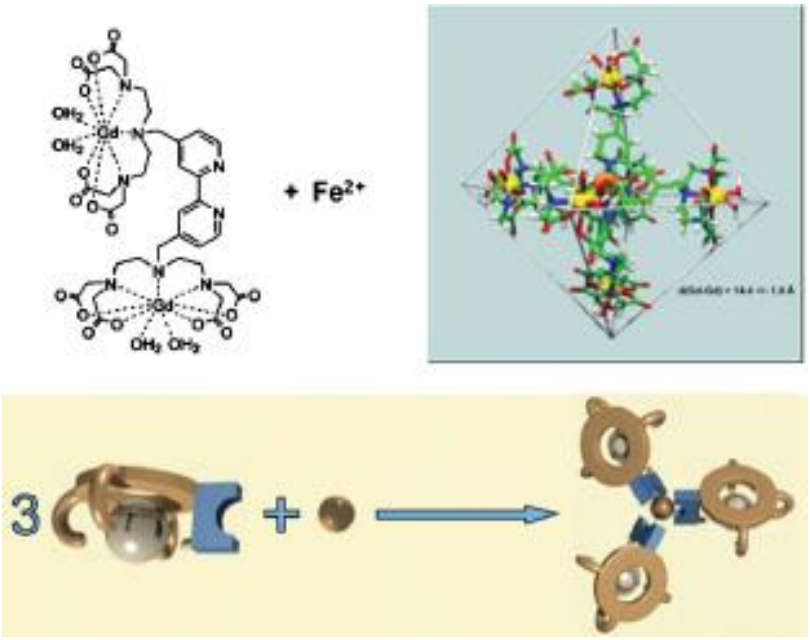

Figure 1.7: Rigid self-assembly to increase relaxivity. Bottom: 3 Gd complexes with pendant bidentate ligands assemble around transition metal ion to increase molecular weight and increase relaxivity. Top: Example from Livramento et al.[18] where three bipy ligands with two q = 2 Gd complexes coordinate Fe(II) to yield a compact assembly with high relaxivity.

The gadolinium chelates in the dendrimer can also undergo internal motion about the linkages to the dendrimer core. Another approach to optimizing the effect of motion on relaxivity is to place the gadolinium at the barycenter of the molecule. The Guerbet group synthesised and studied a Gd-agent called gadomelitol (also called P792 or Vistarem) that can be described as a GdDOTA complex with large hydrophilic groups appended to each of the α-carbons on the acetate arms.[15] Although there is flexibility within the hydrophilic arms, the Gd-H_{water} vector cannot rotate independently of the entire molecule. This lack of internal motion results in a remarkably high relaxivity, r_1 = 39.0 mM^{-1} s^{-1} (37 °C, 0.47 tesla) for a molecule of its size, 6.4 kDa. Parker and coworkers[16] have showed that this rotational effect can be modulated by adjusting the size of the hydrophilic ''arms''.

Another approach for controlling rotational flexibility is the metal templated self-assembly approach described by Jacques and Desreux.[17] They proposed to to append gadolinium complexes to rigid bidentate or tridentate ligands, and then

using a transition metal to assemble the gadolinium complexes in a rigid, compact space, (Figure 1.7 bottom). Livramento *et al.*[18] extended this by using q = 2 gadolinium complexes. Two complexes are covalently linked to a bipyridyl ligand. Three of these bipyridyl ligands coordinate Fe^{2+} in an octahedral fashion resulting in a high relaxivity per Gd^{3+} and per molecule, especially impressive given its high Gd^{3+} content and relatively low molecular weight. The per Gd^{3+} relaxivity of the starting material bipyridyl Gd^{3+} dimer (Figure 1.7, top left) is 12.5 mM^{-1} s^{-1} (40 MHz, 37 °C), which is extremely good compared to the r_1 value of 3.8 mM^{-1} s^{-1} for [Gd(DTPA)(H2O)] measured under the same conditions. The increased relaxivity stems from having two exchangeable waters and an increased molecular weight. In the presence of Fe^{2+}, the bipy ligands coordinate and the Gd^{3+} ions are now part of a rigid molecule with a much longer correlation time and the relaxivity doubles to 26.5 mM^{-1} s^{-1} . This is a very efficient relaxation agent from a synthetic perspective as well; it is a high relaxivity complex that is about 25% Gd^{3+} by weight.

1.4.1 Supramolecular systems

The obvious way to enhance relaxivity is to increase the system τ_R. It is likely that rigidity will play a role in optimizing τ_R as a function of molecular weight. The limitations of slow water exchange on relaxation rate have been recognized, and there is a growing body of evidence to aid in optimizing τ_M. Increasing the hydration number poses some interesting challenges to maintain thermodynamic stability/kinetic inertness and, at the same time, to be resistant to formation of ternary complexes with endogenous ligands such as phosphate and carbonate. However, increasing q offers a large reward in terms of obtainable relaxivities. Another interesting field in the way to increase MRI contrast agents relaxivity is the choose of ligand coordinating donor atoms, because they are intrinsically responsible of the second sphere of coordination of water molecules. Outer-sphere relaxation is still quite a misunderstood entity receiving little attention. This bias is

understandable considering the composition of the clinically available complexes coupled with the need for thermodynamically stable complexes.

The conjugation of low molecular weight chelates such as GdDTPA or GdDOTA to macromolecules alters the biophysical and pharmacological properties of low molecular weight agents.[19] From the biophysical point of view, the conjugation of Gd^{3+} chelates to polymeric materials was anticipated to increase the rotational correlation time and, hence, to improve the relaxivity per Gd^{3+} atom. Combined with tissue-specific targeting moieties, macromolecular conjugates were also envisioned to provide MRI with the ability to image low-concentration receptors by delivering a large payload of Gd^{3+} chelates. High molecular weight conjugates are retained in the vascular space because of their molecular size and thus facilitate blood pool imaging. However, the goal of imaging receptors using MRI in the clinic has been elusive.[20] The most common approaches used to prepare macromolecular structures containing Gd^{3+} chelates involve conjugation of functionalized chelates to polymers, dendrimers, or biological molecules. In addition, macromolecules with multiple ligands were prepared by polymerization.

Conjugation methods for linking chelates to macromolecules are well established in the literature.[21] Typical chemistries include the functionalization of primary amines using acylation, alkylation, ureas or thiourea formation, and reductive amination. The majority of papers have been published using commercially available reagents, such as DTPA itself or DTPA-dianhydride, to functionalize macromolecules. Reaction of these molecules with a reactive primary amine on the macromolecule generates an amide bond using one of the DTPA carboxylates. Although the number of donor atoms is unchanged,, the donor set has been modified as compared with DTPA itself: one acetate donor has been replaced with an amide oxygen.

The advantage over the covalently bound conjugates is that the reversible binding implies the constant presence of small amounts of the “free” monomeric complex that maintains its typical excretory pathway (elimination through the kidneys), thus minimizing the possible toxic effects associated with a long retention time.

The noncovalent interaction promotes an increased residence lifetime of the contrast agent in the vascular system, making it suitable for MRI angiographic applications. In general, it is well recognized that the relaxivities of the HSA-bound complexes (r_1^b) are significantly lower than those expected on the basis of the pronounced slowing down of the molecular motion. Whereas the calculated values of r_1^b for nearly immobilized complexes are of the order of 100 mM^{-1} s^{-1} (20 MHz and 298 K), the experimentally measured values fall in the range 12–55 mM^{-1} s^{-1}.[22]

Much evidence has been collected that demonstrates that the relaxation enhancement of the inner sphere term (r_1^{IS}) is severely limited by a relatively long exchange lifetime (τ_M) of the coordinated water molecule(s). Apart from detailed relaxometric studies, the occurrence of a slow-exchange condition is clearly illustrated by the good linear correlation between the observed r_1^b and k_{ex} values for a series of q = 1 DTPA- and DOTA-like Gd^{3+} complexes (Figure 1.8).

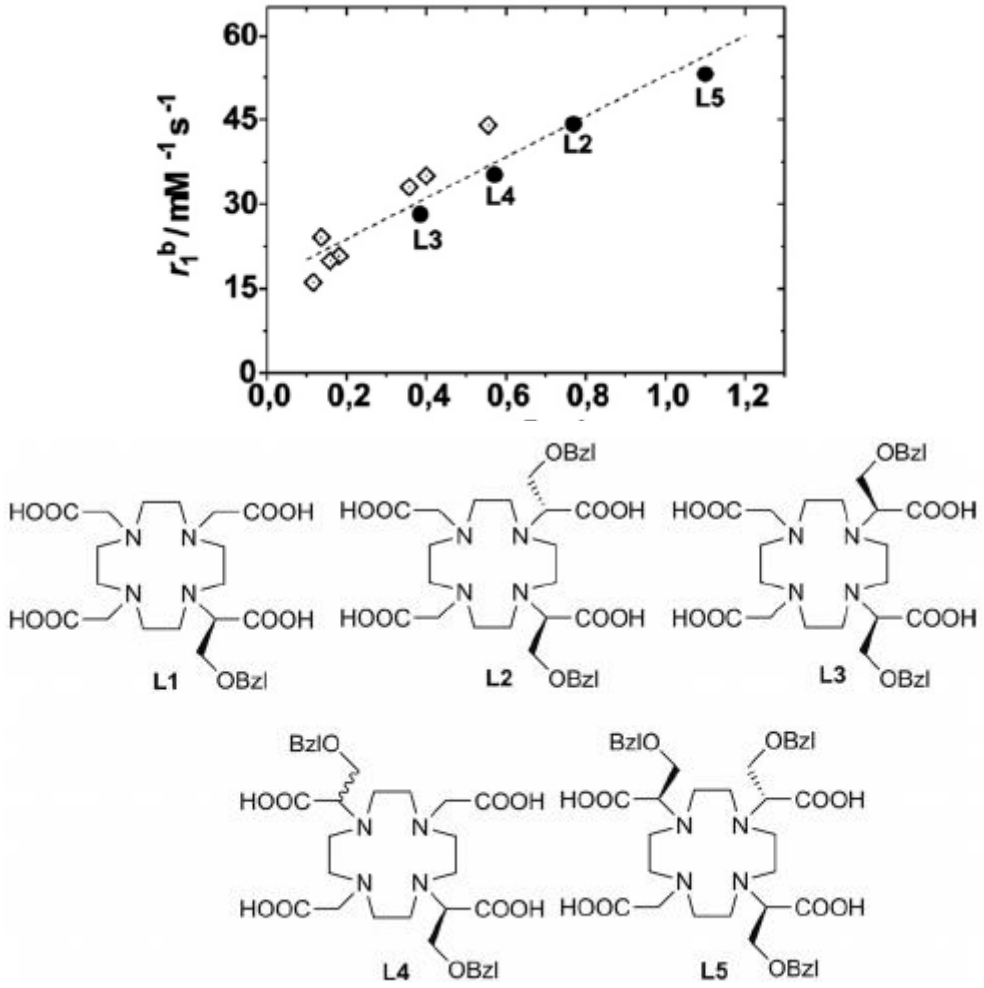

Figure 1.8. top) Correlation between the relaxivity values (20 MHz, 25 °C) of HSA-bound Gd^{3+} complexes with q = 1 and their rate of water exchange. Data not labeled corresponds to data for DOTA and DTPA derivatives; bottom) DOTA-benzyloxymethy derivatives. [*Botta M., Tei L., Eur. J. Inorg. Chem. 2012, 1945–1960*]

The higher relaxivity is associated with the faster rate of water exchange, although still far from the optimal value, of a Gd–DOTA derivative bearing three pendant benzyl groups (Figure 1.8, GdL5).[23]

Complex	r_1 /mM^{-1}s^{-1}	τ_M /ns	TSAP/SAP	$r_1{}^b$ /mM^{-1}s^{-1}
Gd**L1**	5.2	175	0.31	33
Gd**L2**	6.4	120	0.40	40
Gd**L3**	6.8	250	<0.1	22
Gd**L4**	6.6	200	0.19	28
Gd**L5**	7.5	102	0.59	54

Table 1: Relaxometric parameters of complexes GdL1–GdL5.

A more thorough analysis of the properties of this latter complex provides important insights for further relaxivity enhancement. Let us consider five related derivatives of DOTA, containing one, two (two cis isomers and one trans isomer), and three benzyloxymethyl substituents, whose basic relaxometric properties have been previously investigated. Their r_1 values increase from GdL1 to GdL5, simply reflecting the increase in τ_R. The water residence lifetimes, calculated from ^{17}O NMR spectroscopic data, are found to be in the range 100– 250 ns, but they do not show a clear trend. On the other hand, it is well known that two diastereoisomeric pairs of enantiomers are present in the solution of Ln–DOTA complexes.[24] These are referred to as square antiprismatic (SAP or M) and twisted square antiprismatic (TSAP or m) forms. Furthermore, the water exchange rates in TSAP isomers of Gd–DOTA derivatives are about one order of magnitude faster than those of a SAP isomer. Then, the differences in the average or effective τ_M values found for GdL1–GdL5 are likely to reflect a differential distribution of the isomers in each chelate. These distributions have been determined from the integration of the low field axial peaks in the ^1H NMR spectra of the corresponding Eu^{3+} complexes.[24] Knowing the isomer population

makes it possible to fit the ^{17}O data to a sum of the two species, the SAP and TSAP isomers. This procedure enabled the extraction of the τ_M values for both the SAP and TSAP isomers of each complex, which are the same, within the limits of experimental error: τ_M (SAP) = 245.1 ns; τ_M (TSAP) = 41.2 ns. From the data in Table 1, a linear dependence of the relaxivity of the HSA-bound complexes on the isomeric ratio is evident. It is then possible to calculate the corresponding values of the hypothetical single-coordination isomers: r_1^b (SAP) ≈ 15 mM^{-1} s^{-1}; r_1^b (TSAP) ≈ 80 mM^{-1} s^{-1}.

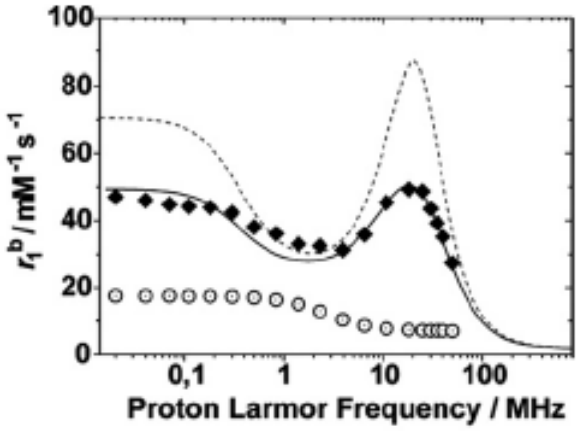

Figure 1.9. NMRD profiles for GdL5 free (.) and bound to HSA (♦). The solid line through the experimental data was calculated with the following parameters: Δ^2 = 4.6 x 10^{18} s^{-2} , τ_v = 23 ps, τ_R = 11 ns, τ_M = 180 ns, r = 3.1 Å, *q* = 1. The upper dashed curve is the simulated NMRD profile with τ_M = 41 ns.

This is illustrated by Figure 1.9, which shows the experimental NMRD profile of GdL5 bound to HSA and the simulated curve with τ_M = 41 ns. Thus, a careful selection of the coordination isomer in DOTA-like complexes may yield relaxivity values for the protein-bound adducts close to those predicted by theory.

In a recent systematic study, Caravan and co-workers have thoroughly investigated the properties of 38 Gd– DOTA derivatives and their binding to serum albumin.[25] Complexes in this series present a distinct protein-binding moiety and differ in the nature of the coordinating arm on one of the macrocyclic nitrogen atoms. At 20 MHz

and 310 K, the r_1^b values were found to be in the range from approximately 12 to 56 mM^{-1} s^{-1}. The important results of this report are: (1) it is possible to modulate the water exchange rate over three orders of magnitude by the proper choice of the donor group (the relaxivities vary accordingly); (2) the second-sphere relaxivity, that is a contribution attributable to water molecules hydrogen-bonded to the polar group of the chelator, plays a role and accounts for differences in r_1^b in similar complexes with identical donor atoms; (3) fast internal motions limit the relaxivity also in the case of complexes characterized by an optimal water exchange rate. In a related study, the importance of the second-sphere relaxivity is further highlighted and shown to be largely increased by introducing amide groups.[26]

The presence of internal flexibility along the chain that connects the metal chelate to the targeting group represents an important limiting effect on the relaxivity of the protein-bound CA even with the optimization of the others parameters. In fact, the internal rotation about the linker does not allow the increase in molecular size to translate into a proportional decrease in the tumbling motion and hence into a relaxivity enhancement. To understand the extent of such an effect on r_1^b, is possible to consider a simple model system consisting of a small and compact Gd^{3+} complex (Gd–NpEGTA) featuring a single fast exchanging bound water molecule, and a rigid targeting moiety for HSA binding (Scheme 1).[27] The rigid naphthalene backbone does not allow a high degree of local motional freedom, and only very small rotational movements of the complex in the binding pocket may take place. As a result, relaxivity values very close to those predicted by theory (68 and 78 mM^{-1} s^{-1}, at 20 and 30 MHz respectively) are reported.

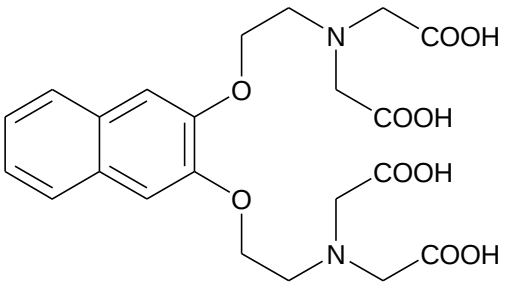

Scheme 1. NpEGTA: a naphthalene rigidified EGTA derivative.

An important approach has been discussed by Caravan et al., who combined the advantages of multimeric Gd^{3+} agents with two targeting vectors.[28] The idea is that two points of attachment help to rigidify the molecule upon binding. A tetrameric Gd–DTPA-based system was functionalized with two HSA-binding moieties; it showed a large relaxivity enhancement (>30 %) as compared to the related agent containing a single binding moiety. Multilocus binding greatly reduces the internal flexibility; thus, making the complex more rigid and the obtained relaxivity value higher.

Another successful strategy to enhance the relaxivity is the use of q = 2 complexes. Doubling the inner sphere water molecules translates into a doubling of r_1^{IS}, the most relevant contribution to relaxivity in macromolecular systems. The Gd^{3+}–hydroxypyridonate (Gd–HOPO) family of contrast agents with q = 2 exhibits optimum water exchange rates (τ_M typically 10 to 20 ns) and high thermodynamic stability (Scheme 2). A poly(ethylene glycol) (PEG) moiety of average molecular weight 5000 Da was attached to the ligand TREN–HOPO–TAM because of the known ability of PEG chains to bind to HSA across a wide pH range.[29] The corresponding Gd^{3+} complex was found to weakly bind HSA with a formation constant k_a = 186 ± 50 M^{-1}. The relaxivity of the protein-bound complex was calculated to be 74 .14 $mm^{-1}s^{-1}$ (20 MHz and 298 K), a value considerably higher than those typically reported.[30] More recently, an analogous approach was followed by attaching a long aliphatic chain to the AAZTA coordination cage (Gd–AAZTAC17), that will be described in the next paragraph.[31]

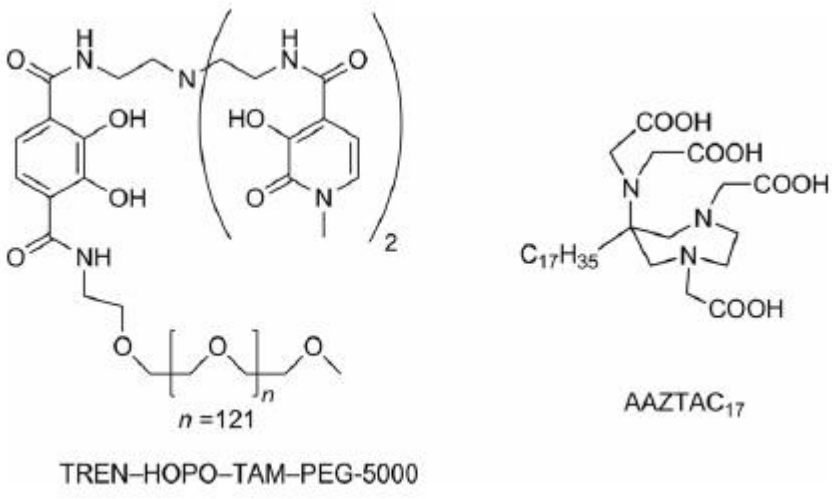

Scheme 2. HOPO and AAZTA derivatives.

This complex (q = 2 and τ_M = 67 ns) was found to have a higher affinity for fatted HSA than for defatted HSA, whereas the relaxivities of the macromolecular adducts were reversed. The relaxivity of the defatted-HSA bound complex (r_1^b= 84 mM^{-1} s^{-1} at 20 MHz and 298 K) is the highest value reported so far for noncovalent paramagnetic adducts with slow-tumbling substrates.

1.4.2 Nanosized lipidic systems

Paramagnetic micelles have often been considered as contrast agents for MRI applications [32]. These molecules form aggregates in which the hydrophobic portions are oriented within the cluster and the hydrophilic moieties (containing the Gd-probe) are exposed to the solvent. Depending on the length and the number of hydrophobic chains and on the nature of the hydrophilic heads, the obtained micelles are characterized by different size and shape (spherical, cylindrical, vesicular). The observed relaxivities (expressed as mM_{Gd}^{-1} s^{-1} are basically determined by the number (q) of water molecules in the inner coordination sphere of the paramagnetic metal ion. In fact, almost all the q = 1 systems have relaxivity values in the range 18–23 mM_{Gd}^{-1} s^{-1} and the q = 2 systems 29 mM_{Gd}^{-1} s^{-1}. Basically, the relatively low relaxivity values shown by the paramagnetic micelles depend on the non-optimal dynamic regime of

these systems, which is characterized by the occurrence of a fast local motion of the Gd-containing cage at the surface of the micelle overlapped to a slower global motion of the supramolecular aggregate.

An accurate determination of the parameters governing the reorientational dynamic may be pursued through the quantitative analysis of the NMRD (Nuclear Magnetic Relaxation Dispersion) profiles. The fitting procedure of the NMRD profiles of Gd-based micelles is frequently performed by using the Solomon–Bloembergen–Morgan equations modified according to the model-free approach developed by Lipari and Szabo for non-extreme narrowing conditions [33,34]. This approach allows to distinguish between a local faster motion (governed by τ_{Rl}) and a global slower motion (governed by τ_{Rg}).

1.4.2.1 Self-assembling aggregates of amphiphilic Gd(III) complexes

Amphiphilic Gd-complexes consist of a chelating agent covalently bound to one or more hydrophobic moieties such as long alkyl chains or organic residues that promotes the aggregation process in a water-based solution. Generally, the kind of aggregate obtained by self-assembly of amphiphilic Gd-complexes without the use of external molecules are micelles. In micelles, the Gd^{3+} complexes are exposed to the hydrophilic exterior spacewith easy access of the bulk water to the paramagnetic center.

The structural properties of the hydrophobic chain such as its length and its nature can influence the stability, the size and the aggregation number of monomers in the micelle. Moreover, the relaxivity behaviour of micelles can dramatically change as a function of the hydrophobic moiety.

Several studies were carried out on amphiphilic chelating agents in order to determine the most accurate mathematical approach to study the rotational dynamics of the aggregates, and to justify the relaxivity values. Between 1999 and 2002, Merbach and co-workers[35,36] described the synthesis and relaxometric characterization of five

potential Gd^{3+}-based MRI contrast agents which are capable of micellar self-organization. They mainly differ in the length of their side chain, varying from 10 to 18 carbon atoms.

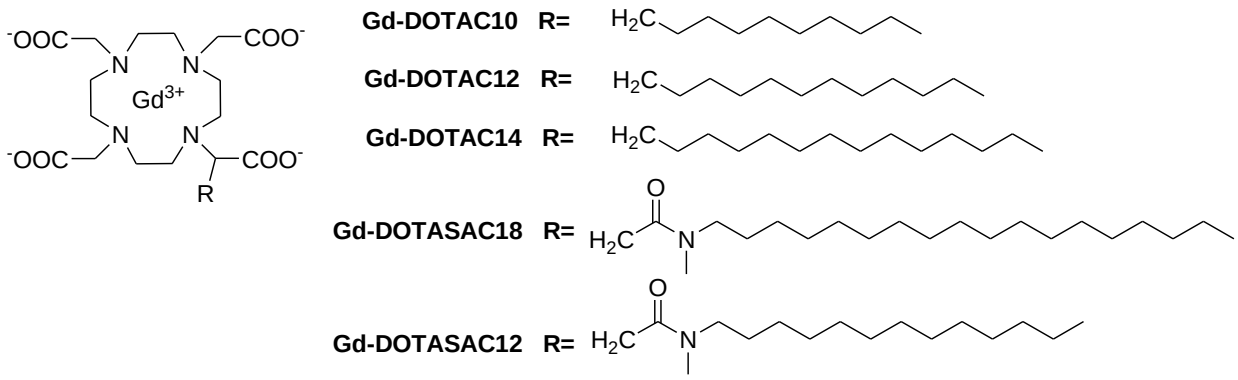

Scheme 3: GdDOTA-like amphiphilic complexes studied by Merbach and coworkers.

Three of them, $[Gd(DOTAC10)(H_2O)]^-$, $[Gd(DOTAC12)(H_2O)]^-$ and $[Gd(DOTAC14)(H_2O)]^-$ are DOTA-like chelates bearing an alkyl chain with 10, 12 and 14 carbon atoms. The other two, $[Gd(DOTASAC12)(H_2O)]$ and $[Gd(DOTASAC18)(H_2O)]$ have a DOTA chelating unit and a monoamide-dodecyl or a monoamideoctadecyl carbon side chain, respectively (Scheme 3). As stated above, for the analysis of the longitudinal ^{17}O and ^{1}H relaxation rates of the aggregates, the authors used the Solomon–Bloembergen–Morgan model, modified according to the Lipari–Szabo approach. The relaxivity values of the five micellar systems are reported in Table 2.

	r_1 (mM^{-1} s^{-1})
Gd-DOTAC10	**9.3**
Gd-DOTAC12	**17.2**
Gd-DOTAC14	**21.5**
Gd-DOTASAC18	**20.7**
Gd-DOTASAC12	**18.0**

Table 2: relaxivity values of the five micellar systems reported in Scheme X

It is interesting to underline that the relaxivity increases with increasing chain length within the series, with the exception of $[Gd(DOTASAC18)(H_2O)]^-$. This effect can be explained by the different rotational motions (global and local) and by the model-free parameter S^2 of the five systems. As expected, the global rotational correlation time, τ_g, increases with increasing length of the side chain (τ_g = 1600, 2220, 2810 ps, for $[Gd(DOTAC12)(H_2O)]^-$, $[Gd(DOTAC14)(H_2O)]^-$, $[Gd(DOTASAC18)(H_2O)]^-$, respectively). On the other hand, the local motions, that are also influenced by length and the hydrophobicity of the side chain, do not follow the expected behaviour: in fact in $[Gd(DOTASAC18)(H_2O)]^-$ micelles the additional amide function, prevents strong hydrophobic interactions between the long chains and reduces its internal flexibility (short τ_l value and low S^2).

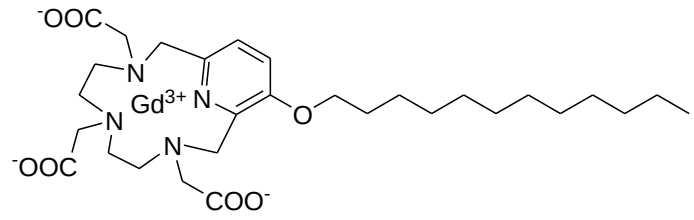

Gd-PCTA-[12]

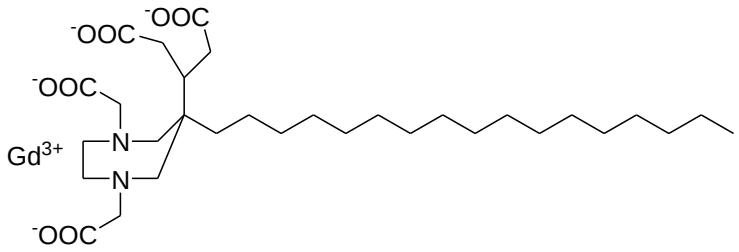

Gd-AAZTAC17

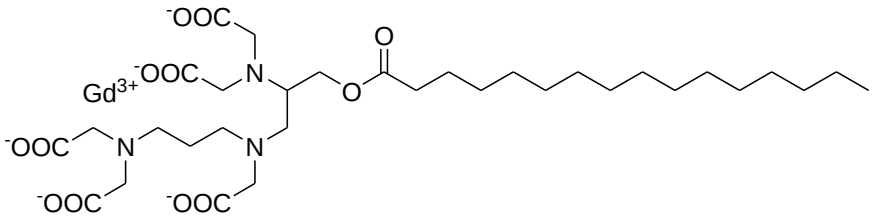

Gd-EPTPA-C16

Scheme 4: Some amphiphilic Gd^{3+} complexes.

The relaxivity value of the supramolecular aggregate is influenced not only by their hydrophobic moiety, but also by the chelating agent on the head-group. For example, the relaxivity value strongly increases from 18.0 to 29.2 $mM^{-1}s^{-1}$ by replacing DOTA-

like ligands with PCTA [37], a $q = 2$ chelate, notwithstanding the two monomers Gd-PCTA-[C12] and DOTASAC12 (indicated in Scheme 3 and 4) have the same hydrophobic chain, the same coordination geometry on the gadolinium ion and aggregation properties (micelles with a similar critical micellar concentration in the 1.5–3.4 × 10^{-4} M range). This means that the enhancement in terms of relaxivity is mostly ascribable to the increase of the number of inner sphere coordinated water molecules.

	r_1 (mM^{-1} s^{-1})
Gd-PCTA[12]	**29.2**
Gd-AAZTAC17	**30.0**
Gd-EPTPA-C16	**22.6**

Table 3: relaxivity values of the micellar systems represented in Scheme 4.

Clearly the micellization of amphiphilic gadolinium complexes gives rise to a system with slower molecular tumbling with respect to the monomeric complex, but the resulting relaxivity appears still lower than the expected values as internal motions are faster than the overall tumbling of the micellar system. Merbach and coworkers proposed that interactions between nearby paramagnetic centers in micellar systems increase the transverse electronic relaxation of the electronic spin of Gd^{3+} and, therefore, reduce the attainable water proton relaxivity [38]. This drawback can be removed by diluting the Gd^{3+} ions with diamagnetic Y^{3+} ions in order to increase the distance between the neighbouring Gd^{3+} ions. This theory was also recently confirmed by Aime et al. for micellar aggregates obtained by self-assembling of the Gd-AAZTAC17 amphiphilic gadolinium complex 7. They studied how the relaxivity value of micellar aggregates of Gd-AATZAC17 (30.0 mM^{-1} s^{-1}) changes when 98% of the Gd^{3+} complexes on the external surface of the micelles is replaced by the corresponding Y^{3+} complexes. The result observed was an enhancement in relaxivity of around 40% over the entire frequency range (41.4 mM^{-1} s^{-1} at 20 MHz [39].

In 2006 Geraldes *et al.* [40] reported an "in vitro" characterization and "in vivo" animal imaging studies on self-assembling micelles of Gd-EPTPA-C16 monomer. The in vivo results were compared with the commercially available low molecular weight Magnevist® [41]. The critical micellar concentration (3×10^{-4} M) of the amphiphilic $[(Gd\text{-}EPTPA\text{-}C16)(H_2O)]^{2-}$ chelate was determined by variable-concentration proton relaxivity measurements. The rotational dynamics of the micelles, analyzed by using the Lipari–Szabo approach, suggested that micelles formed in aqueous solution show considerable flexibility, with a local rotational correlation time of τ_l = 330 ps and a global rotational correlation time τ_g = 2100 ps. These values are in good agreement with the results above described for the five compounds reported in Scheme 3. The in vivo evaluation of the micellar $[Gd(EPTPA\text{-}C16)(H_2O)]^{2-}$ compound in Wistar rats shows a persistent hepatic positive-contrast effect in T_1-weighted images, which is qualitatively similar to that of the clinically established Gd^{3+}-based hepatobiliary agents, Gd-EOB-DTPA [42] and Gd-BOPTA [43]. The possibility of using this type of micellar compound for imaging disease depends on the degree of stability of the imaging agent in the body relative to its critical micellar concentration. The amphiphilic gadolinium complexes above described have only one hydrophobic chain. Critical micellar concentration of mono-tailed surfactants is usually in the range of 0.1–0.01 mM. Upon dilution in the blood following injection, these aggregates may not be sufficiently stable and disassemble immediately following administration. Hence, there is a need to find a new class of surfactant molecules able to form more stable micelles with lower critical micellar concentration values. One of the possible candidates for this role, can be represented by aggregates obtained by self-assembling of monomers with two or more alkyl chains.

Recently, Paduano et al. reported supramolecular aggregates, constituted basically by the DTPAGlu moiety bound to a hydrophobic double-tail (18 carbon atoms), [43]. The amphiphilic molecule behaves as an anionic surfactant, and is capable of forming aggregates of different sizes and shapes (rodlike micelles, threadlike micelles, and vesicles) in aqueous solution by varying the method of preparation and the environmental conditions such as pH and ionic strength. A micelle-to-vesicle transition was observed by decreasing the pH value from 7.4 to 3.0; and/or by

increasing the ionic strength. Relaxivity values of Gd-$(C18)_2$DTPAGlu aggregates at pH 7.4 in the presence and absence of NaCl at physiological ionic strength were 21.5 and 24.0 mM^{-1} s^{-1} , respectively [44,45].

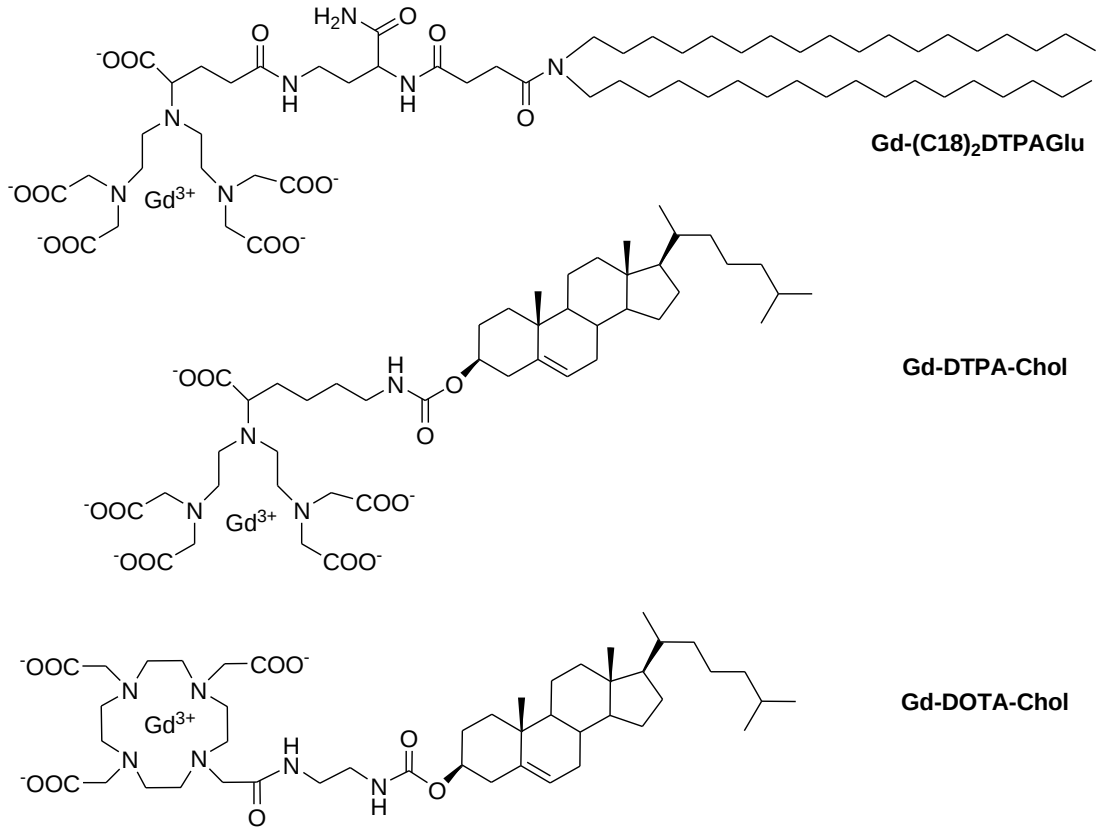

Scheme 5. Some DOTA- and DTPA-like Gd^{3+} amphiphilic complexes.

An alternative approach to prepare physiologically stable aggregates include the use of Gd-labelled polymerized liposomes, prepared by using a polymerizable amphiphilic Gd–DTPA derivative [46].

In the literature there are few examples of supramolecular aggregates obtained also by starting from amphiphilic Gd-complexes in which the hydrophobic moiety is not represented by an alkyl chain, but from an organic molecule such as cholic acid.

In 2003 Lattuada et al. reported the synthesis of Gd-DTPA-Chol. Its relaxivity value in water (27.2 mM^{-1} s^{-1}), extremely high compared to the relaxivity of the Gd-DTPA (3.7 mM^{-1} s^{-1}), is an indirect evidence of micellar self-organization [47]. In 2006 Jorgensen et al. synthesized and studied the relaxometric behaviour of another cholesterol-based Gd-complex, Gd-DOTA-Chol, in which the chelating agent is represented by a DOTA-monoamide. This complex was designed to be easily embedded into the membrane of

standard cationic liposomes in order to develop a liposome cell labelling system, which would be amenable to labell a variety of cells, and could serve other purposes such as delivery of plasmid DNA or other nucleic acid derived therapeutics. The relaxivity of Gd-DOTAMA-Chol (4.42 mM^{-1} s^{-1}, 298 K and 20 MHz) is in the same order of values of the clinically used Dotarem (5.25 mM^{-1} s^{-1}, 298 K and 20 MHz), thus indicating the Gd-DOTAMA-Chol is unable to self-aggregate [48]. The uncapability of Gd-DOTAMA-Chol to self-aggregate can be ascribed to the lack of anionic charges on the complex that reduces the amphiphylic character of the complex.

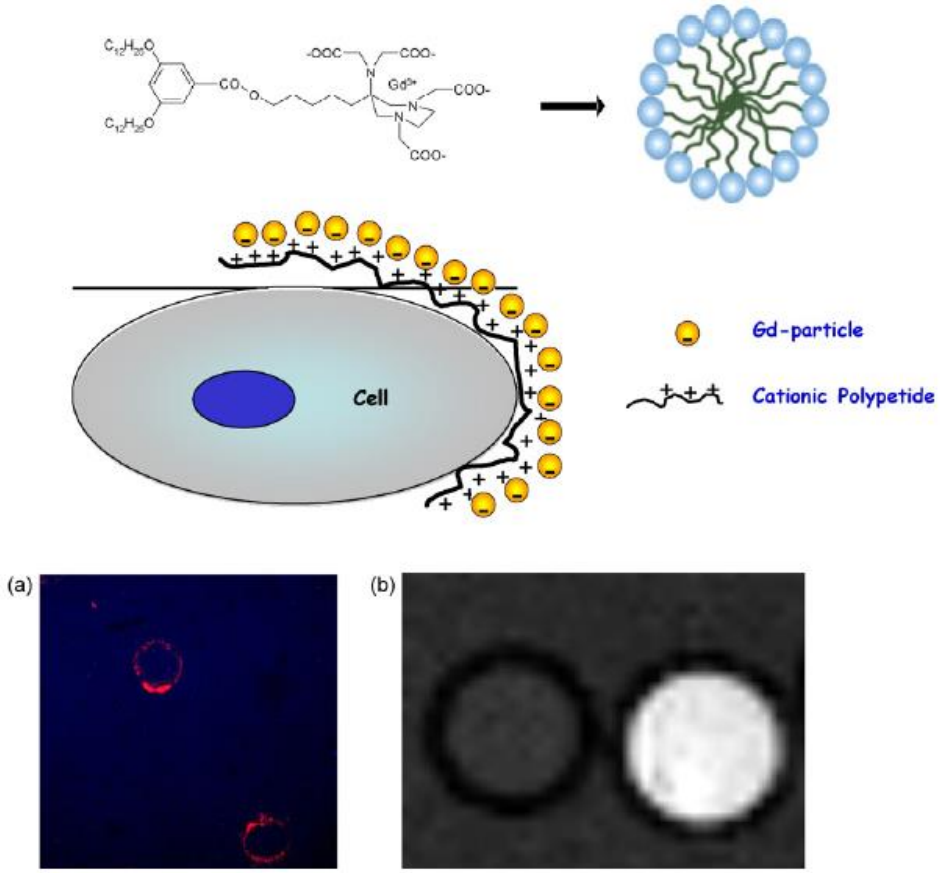

Figure 1.10. The design of the high sensitivity MR-imaging reporter. (a) The binding of the supramolecular adduct at the cell membrane through the intermediation of the cationic linker is validated by the confocal microscopy images obtained by using a Gd-containing nanoparticle doped with a rhodamine-phospholipid and polyarginine. (b) MRI of cellular pellets in agar. The cells labeled with polyarginine/Gd-nanoparticles (right) contains approximately 6 × 10^9 Gd per cell and display a T_1 value of 334 ms to be compared with a T_1 of 2064 ms of the

unlabeled cells (left). [*D. Delli Castelli et al. / Coordination Chemistry Reviews 252 (2008) 2424–2443*]

Another interesting system, developed by Aime and co-workers, consists of self-assembled lipophilic Gd-AAZTA(C16)$_2$ complexes (Figure 1.10) interacting with the cell-surface labelled with cationic polyarginine. . The presence of two long aliphatic chains and the aromatic moiety endowed this amphiphilic complex with a very high tendency to aggregate in aqueous media. Already at monomer concentration as low as 1×10^{-5} M the system appears to be present in an aggregated form (likely discoidal aggregates) characterized by a relaxivity of 25 mM_{Gd}^{-1} s^{-1} at 298 K and 20 MHz, a diameter of ca. 80 nm (with a very low polydispersity index) and an aggregation number of ca. 850.

1.4.2.2 Lipid nanoparticles: micelles

Another class of supramolecular aggregates containing amphiphilic Gd-complexes could be obtained by their co-assembling with one or more commercial surfactants such as phospholipids, non-ionic surfactants or cholesterol. Classical phospholipids can be divided in saturated (DPPC, DSPC, DSPE) and unsaturated (DOPC, POPC) molecules.

The most common components of phospholipids are phosphatidyl choline (PC), phosphatidyl glycerol (PG) and phosphatidyl ethanolamine (PE). Generally, the presence of phospholipids within the supramolecular aggregate favours the formation of bilayer structures such as vesicles or liposomes. One of the first examples of supramolecular aggregates obtained by amphiphilic Gd-complexes mixed to phospholipids was reported in 1992 from Elgavish et al. They synthesized several

amphiphilic Gd-complexes based on DTTA ligand (DTTA = diethylenetriaminotetraacetic acid; 1MP-DTTA; 4MP-DTTA; 4MPD-DTTA; BME-DTTA) and studied the in vitro relaxometric behaviour and the in vivo properties of mixed liposomes as potential contrast agents for MRI of myocardial under-perfusion[49,50–52]. For example, Gd-BME-DTTA (Scheme 6) was obtained by conjugating the DTTA chelating moiety to two long fatty myristoyl chains. Because of its limited solubility in water, Gd-BME-DTTA complex was incorporated into egg lecithin liposomes.

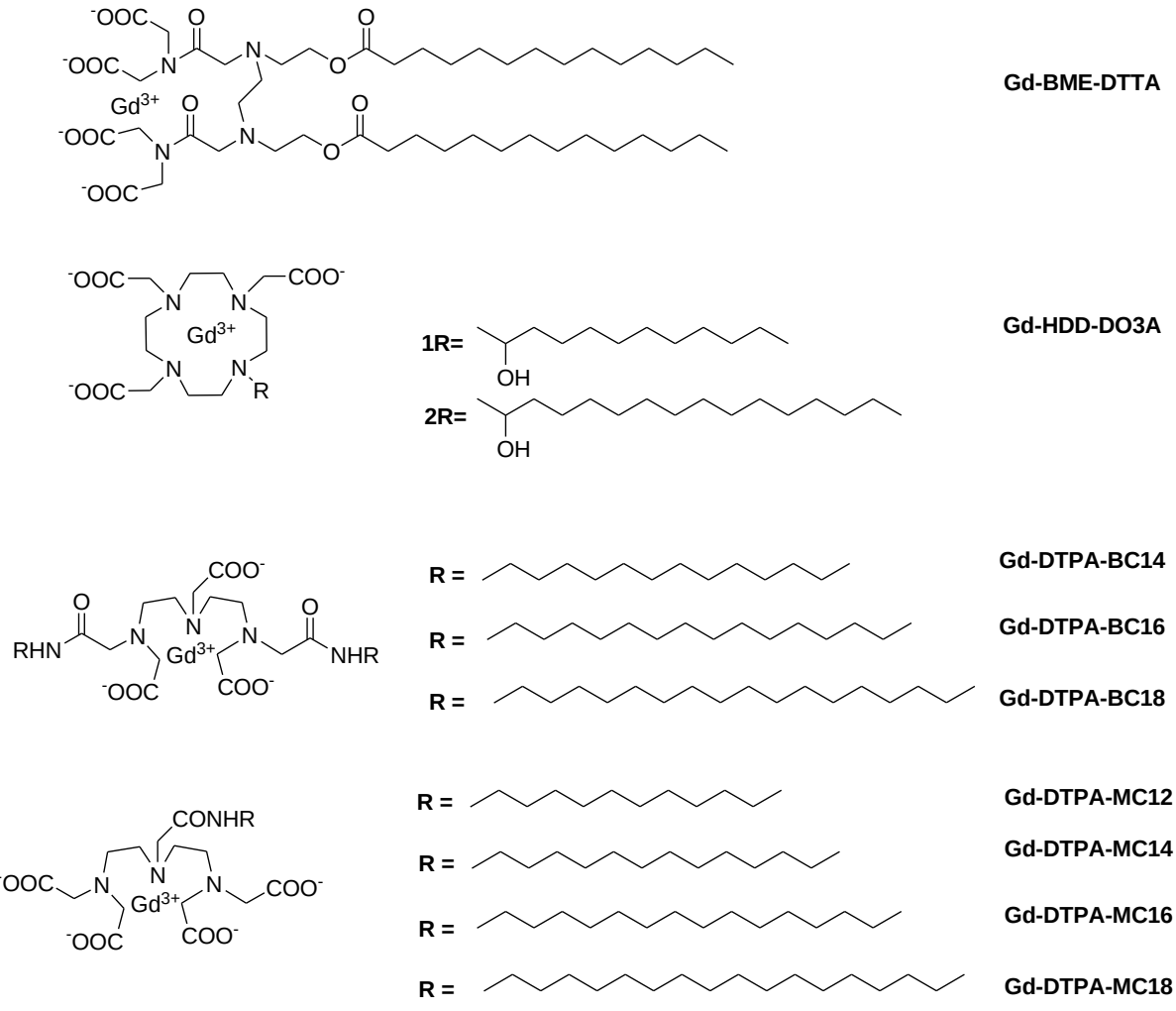

Scheme 6.

The median lethal dose (LD50) of liposomal Gd-BME-DTTA formulation in mice was of 0.56 ± 0.05 mmol/kg and no deleterious effects on heart rate, blood pressure, left ventricular force and AV conductance in ferret hearts in vivo at the magnetic resonance imaging effective dose of 0.05 mmol/kg body weight were detected. In MRI images, a

^{1}H signal intensity enhancement was observed in the following organs in decreasing order of the effect: heart ≈ spleen > kidney > liver. This enhancement remained stable for over 3 h in all organs. Moreover, the incorporation of Gd-BME-DTTA in liposomes produced an increase of the in vitro relaxivity of the contrast agent up to 27.0 mM^{-1} s^{-1} . In anyway, the relaxivity of a liposomal Gd-BME-DTTA sample, stored at 4◦ C, remained stable for over 4 months of observation, but a significant decrease in relaxivity (8.2 mM^{-1} s^{-1} after 40 days) was observed in a sample stored at room temperature. The observed time-dependent reduction in relaxivity can be possibly attributed to the dissociation of Gd-BME-DTTA from the phospholipid bilayer. Thus, liposome stability and relaxivity properties of the aggregate over the time are strongly related to the incorporation degree of amphiphilic gadolinium complex in the liposome membrane.

At this purpose, in 2000 Gløgård et al. investigated the effect on the relaxivity of several parameters including the incorporation degree of the Gd^{3+} amphiphilic chelates on the membrane packing. They studied mixed liposomes formulated by using several phospholipid molecules (DMPC, DPPC, DSPC, DMPG, DPPG, DSPG) in which two amphiphilic Gd-HPDO3A-like derivatives were alternatively introduced [53]. Gd-HDD-DO3A and Gd-HHD-DO3A (Scheme 5) were synthesized by functionalizing DO3A chelating agent with hydroxydodecyl and hydroxyhexadecyl moieties, respectively. In the different formulations, the amount of cholesterol and the type of Gd-chelate, were varied between 0–40 and 1–10% mol/mol, respectively. The incorporation efficacy seems to be directly correlated to the lipophilic moiety of the chelates. In fact, Gd-HHD-DO3A, with the highest partition (P) coefficient between 1-octanol and water, was completely incorporated whereas an incorporation efficacy between 12 and 23% was observed for the less lipophilic Gd-HDD-DO3A. Moreover, larger liposomes showed only a minor positive effect on the incorporation efficacy, while the cholesterol content has no effect on the Gd-chelate loading [54]. In contrast to the expected results, the relaxivity value decreased with the increase of incorporation degree of Gd-complex maybe due to the negative influence of the Gd-chelate on the membrane packing . Likely, the impact of this effect is an increase in the lateral surface motion on the liposome surface, leading to a shortening of τ_R for the Gd-chelates and thereby a decrease in the relaxivity. The same authors also reported on the influence

of the cholesterol content on the structure and relaxivity of aggregates obtained by Gd-HHD-DO3A [55].

The incorporation degree of amphiphilic Gd-complexes in liposomes represents only one of the numerous parameters that can play an important role in the relaxometric behaviour of liposomes. The mobility degree of the amphiphilic Gd-complex depends on the length and on the position of the alkyl chains on the Gd-complex. In this contest, Binnemans et al. between 2003 and 2006 reported the synthesis of three different sets of amphiphilic derivatives of DTPA with alkyl chains of different length. The Gd-complexes of these ligands were incorporated into mixed aggregates of DPPC phospholipid and Tween 80 to obtain supramolecular structures. In the first set, the amphiphilic Gd-complexes are represented by DTPAbisamide derivatives with alkyl chains containing 14, 16 and 18 carbon atoms (Gd-DTPA-BC14, Gd-DTPA-BC16 and Gd-DTPA-BC18 (Scheme 5) [56]. In the second set, DTPA-bisamide derivatives were replaced by the DTPA-monoamides (Gd-DTPA-MC12, Gd-DTPA-MC14, Gd-DTPA-MC16 and Gd-DTPA-MC18, Scheme 5) [57]. Finally, in the last set the DTPA-bisamide derivatives were modified by introducing aromatic side chain groups (DTPA-BPT; DTPA-BPH and DTPA-BPO, Scheme 6) [58]. By comparing τ_M and τ_R values of the three sets of aggregates resulted that the relaxivity values of mixed aggregates incorporating monoamide complexes were higher than aggregates incorporating bisamide compounds with analogous chain length. Both τ_M and τ_R values of Gd-DTPA-MCn monoamide supramolecular aggregates were smaller than those of Gd-DTPA-BCn and Gd-DTPA-BPX. Indeed it is well known that Gd-DTPA derivatives with amide groups are characterized by a decreased exchange rate of the coordinated water molecule and that τ_M is related to the number of amide functions and their substituents[59]. On the other hand the τ_R values decreased as a consequence of a more efficient immobilization of the paramagnetic part of the bisamide derivatives caused by the incorporation of both hydrophobic chains into the micellar or liposomal membrane. These smaller τ_R values were not followed by a decrease but by an increase in relaxivity because of the smaller τ_M values.

The immobilization of bisamide derivatives at eighteen carbon atoms (Gd-DTPA-BC18 and Gd-DTPA-BPO) inside the supramolecular structure was less effective, probably

because the aliphatic chains of the complex were longer than the alkyl chains of DPPC, in which it was inserted, resulting in a relatively high local mobility. The corresponding paramagnetic aggregates with 14 carbon atoms chains DTPA-BPT showed the highest relaxivity, most likely because the optimal length match between the hydrophobic chains of the DPPC and the amphiphilic Gd-complex allowed very efficient packing of the paramagnetic complex into the aggregate. Mixed micelles incorporating Gd-DTPA-MC12 amphiphilic monomer show a relaxivity value (5.0 mM^{-1} s^{-1}) more similar to its parent compound Gd-DTPA than the supramolecular aggregates. It can be explained by comparing the τ_R values obtained for the Gd-DTPA-MC12 (0.105 ns) in the micellar solution with respect to those of the other complexes of the series (0.91–1.12 ns). This result indicates that this complex is either very loosely incorporated inside the micellar membrane or not incorporated at all. It was suggested that the aliphatic chain of this complex was too short and the hydrophobic character of the complex too low to allow efficient incorporation into the micellar structures. Finally, the same authors studied a compound (Scheme 7), Gd-DTPA-BC18Aunsat, containing one C=C double bond in each of the two lipophilic chains[60]. The presence of the unsaturations, as reported above, increased the flexibility inside the membrane layers and the water permeability, thus increasing relaxivity.

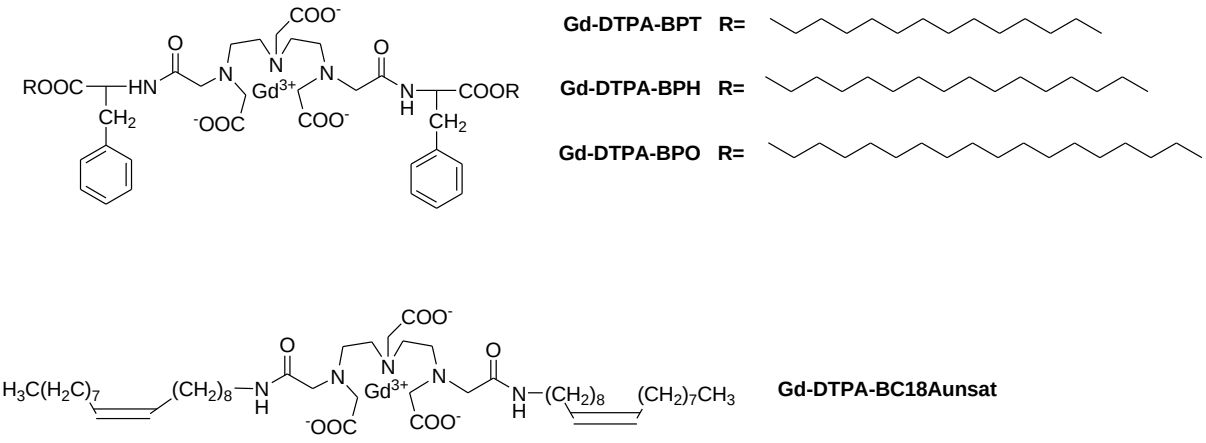

Scheme 7

Another factor influencing relaxivity is represented by the membrane composition of aggregates, such as the saturation level of membrane, the transition phase temperature of phospholipids and the cholesterol content. As above reported, Gd-complexes

incorporated in liposome bilayer can distribute on both sides of the phospholipidic membrane and the two contributions arising respectively from the complexes in the inner and in the outer layers have to be considered. The two contributions depend from liposome membrane permeability which is strictly related to the bilayer composition (saturated or unsaturated phospholipids). Liposomes obtained with saturated phospholipids present a lower membrane permeability with respect to those made by unsaturated phospholipids[61,62]. The reason for such a behaviour is the different packing of the hydrophobic chains in the bilayer. The presence of an unsaturation in the hydrocarbon chain reduces the tightness of the bilayer assembly, thus facilitating the water flux across the bilayer and improving the relaxivity. When the liposome membrane permeability is high, the water exchange is extremely fast and both the complexes in the inner and in the outer layer contribute to the observed paramagnetic relaxation rate[63]. On the contrary, if the membrane permeability is low, water exchange rate through the membrane is very slow and the main relaxation effect is due to the complexes exposed to the external media. This theory was very recently confirmed by Muller et al. who compared the relaxometric behaviour of two unilamellar liposomes (DPPC/Gd-DTPA-BC14 = 10/1), incorporating Gd^{3+} amphiphilic complexes either in their external and internal layers or only at the external one. Mixed liposomes with Gd-complexes located only in the external part were successfully obtained by transmetallation of La^{3+} by Gd^{3+} ions of DPPC/La-DTPA-BC14 liposomes. The relaxivity of these liposomes (16.98 mM^{-1} s^{-1}) is increased as compared to that of the liposomes containing the complex in both sides of the membrane (9.86 mM^{-1} s^{-1}), thus indicating that the complexes located in the internal layer contributes less to the global relaxivity[64].

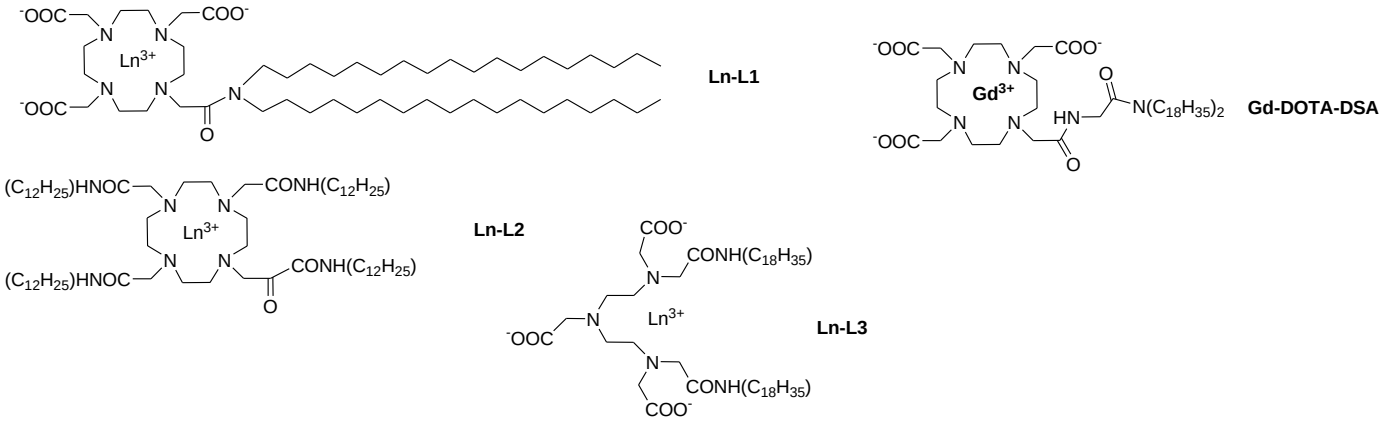

Scheme 7.

The water permeability (P_W) of liposomes can also be strongly influenced by the incorporation of amphiphilic Gd-complexes in the lipid bilayer, as reported by Aime et al. Two liposome formulations (DPPC/DSPE-PEG2000 and POPC/Chol/DSPE-PEG2000) were selected in order to compare the variation of P_W between the saturated and unsaturated liposomes. The amphiphilic complexes used for the experiments (Scheme 7) were previously proposed by Lattuada et al. as a new class of stable blood pool MRI/MRA contrast agents after incorporation in mixed aggregates[65,66]. The incorporation in DPPC-based liposomes of La**L1** complex, bearing two saturated C18 chains, did not affect so much the water permeability of the membrane, while the incorporation of La**L2** complex (Scheme 7), bearing one saturated C12 chain for each coordination arm of the chelate, significantly accelerated the water mobility across the membrane. This result suggests that the incorporation modality adopted by the latter amphiphilic compound destabilizes the compact packing of the DPPC bilayer.

On the other hand, when the amphiphilic complexes are incorporated in unsaturated liposomes (POPC-based liposomes) a stabilization of the aggregate occurs and the water permeability of the membrane decreases proportionally to the amount of the incorporated compound[67].

Another extremely important parameter influencing the relaxivity is represented by the transition phase temperature. Liposome bilayers present a liquid-crystalline state and a high water exchange rate between the interior and exterior liposome comparments, allowing bulk water to experience magnetic interaction with the Gd-chelates located on the inner surface. On the contrary, liposome bilayers in the solid–

gel state have a low water exchange rate, making the inner surface chelates less accessible for the bulk water and thereby decreasing their contribution to the overall relaxivity[49]. Also the lateral motion on the liposome surface is about twice as high in a liquid-crystalline membrane compared to a gel state membrane[68]. This should give rise to a longer τ_R for the Gd-chelates incorporated into a gel state-membrane with respect to complexes incorporated in liquid-crystalline state, thereby increasing their relaxivity.

The cholesterol introduction in the formulation has always a positive effect on the relaxivity. The influence of cholesterol on the liposome membrane is associated to the phase transition temperature of the latter. With its incorporation into a solid–gel liposome cholesterol fluidises the membrane, leading to increased transmembrane water permeability and hence to an increased relaxivity of the Gd-chelates present inside the liposomes. In liquid-crystalline liposomes, the positive effect of cholesterol incorporation is most likely related to an increase in the membrane rigidity leading to an increase of the rotational correlation time (τ_R) of the Gd-chelate. According to these considerations, the highest relaxivity was obtained for DMPC-based liposomes (24–42 mM^{-1} s^{-1}) compared to the DSPC-ones (20–28 mM^{-1} s^{-1}). According to Gløgård assumption, Strijkers et al. verified that unsaturated lipidbased liposomes (DOPC/DSPE-PEG2000/Gd-DTPABSA) have higher relaxivity with respect to liposomes based on saturated phospholipids (DSPC/DSPE-PEG2000/Gd-DTPABOA), and the adding of cholesterol leads to a further, although smaller, increase of the relaxivity[69].

Moreover, Aime et al.[70], proposed systems based mixed liposomes in which Gd-complexes are conjugated to phospholipids by a disulfide bond, that is sensitive to the presence of radicals: when the disulfide bond is cleaved upon radical attach the T_1-relaxivity of the system decreases to give the r_1 value of the free Gd chelate.

Nowadays, the research is devoted to find new multifunctional liposomes, able to address at the same time two or more targets, such as pDNA transfection or diagnosis and treatment of diseases. For example, in the last year Miller et al. reported bimodal paramagnetic and fluorescent liposomes both for in vitro cell labelling and in vivo tumour imaging [71]. The amphiphilic Gd-DOTA·DSA complex (Scheme 7) and a small amount of the fluorescent lipid DOPE-Rhodamine (0.5–1.0 mole%)were incorporated

in DOPC/Chol/DSPE-PEG2000 liposomes. This method permits to quantify uptake and internalization of liposomes into cells. Liposomal surface was also modified with PEG chains to prolong their circulation time in the body[72]. In fact, surface modification with PEG polymers produces changes in biodistribution and body retention of liposomes preventing their opsonisation by macrophages[73-75].

1.4.2.3 Lipid nanoparticles: Liposomes

Liposomes are nanosized vesicles in which an aqueous core is encapsulated by one (unilamellar) or more (multilamellar) phospholipidic bilayers. A further sub-classification divides the unilamellar vesicles (UV) in small (SUV, diameter of 50–150 nm) and large (LUV, 150–800) liposomes according to their size. As soon as they were discovered [76], it was immediately recognized the great relevance that such systems could have in the biomedical field as model systems for studying biological membranes and as drug carriers. As far as concern the latter application, the main strong points in favour of liposomes are: (i) high biocompatibility, (ii) easiness of preparation, (iii) possibility to carry hydrophilic, amphiphilic and lipophilic molecules, (iv) possibility of modulating the pharmacokinetic properties by changing the chemical composition of the bilayer. In addition to all these properties that make liposomes excellent nanocarriers for MRI applications, they can also greatly improve the contrastographic efficiency of the transported agent.

The first reports about the use of liposomes loaded with T_1-shortening MRI agents were published in the late 1980s and dealt with the encapsulation of high amounts (hundreds of millimolar) of hydrophilic paramagnetic ions as Mn^{2+} [77] or Mn^{2+}- and

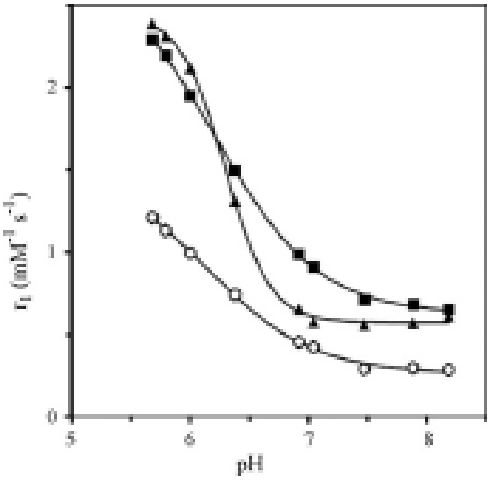

Figure 1.13. r_1 relaxometric pH dependence of dipalmitoylPE/DPGS liposomes encapsulating Gd-DTPA-BMA containing 10 mol% (filled squares) and 30 mol% (upper triangles) of DPSG, and distearylPE/DPGS containing 10 mol% of DPGS (open circles) after 20 min of incubation in buffered human whole blood (0.47 T, 310 K). Adapted from ref. [84].

Gd^{3+}-complexes [78-81] in the aqueous core of the vesicle. The resulting paramagnetic vesicles were mainly used as carriers for the delivery of the imaging agents to pathological tissues, mostly tumors, where the liposomes are expected to passively accumulate thanks to the Enhanced Permeability and Retention (EPR) mechanism [82,83].

The successful MRI visualization of several tumors on animal models (including the detection of liver metastasis) after the i.v. injection of T_1-shortening liposomes is primarily the result of the high relaxivity of the nanosized vesicles that carries hundreds of thousands of imaging reporters. However, it is worth noting that the relaxation enhancing efficacy of a single imaging reporter is considerably "quenched" when it is encapsulated in the liposome. As an illustrative example, the millimolar relaxivity of the clinically approved Gd-HPDO3A complex decreases of about one order of magnitude from 3.75 mM_{Gd}^{-1} s^{-1} to 0.3 mM_{Gd}^{-1} s^{-1} (values measured at 0.47 T and 310 K) when the imaging reporter is entrapped in the liposome cavity [81]. It has been demonstrated that this "quenching" effect is inversely proportional to the water permeability of the liposome bilayer and to the size of the vesicle, and it is directly dependent on the concentration of the paramagnetic system inside the vesicle.

The relaxivity "quenching" caused by the encapsulation of the imaging reporter has been exploited for designing responsive agents in which the water permeability of the bilayer or the overall integrity of the vesicles is made sensitive to physicochemical variables of theragnostic relevance. Two representative examples can be found in the classes of pH and temperature responsive agents. In the former case, the imaging reporter is encapsulated in liposomes whose bilayer contains components that change their structure (and charge) as a function of pH. A typical combination of amphiphiles that confer to the bilayer a pH-responsiveness tuned at the physio-pathological values

is represented by phosphatidylethanolamine (PE)-based phospholipids and dipalmitoylglycerosuccinate (DPGS).

As far as the temperature reporters is concerned, liposomal MRI probes able to switch on the T_1 contrast in a narrow temperature range were designed by selecting phospholipides with a well-defined gel-to-liquid crystalline transition phase temperature (T_m), like distearylphosphatidylcholine (DSPC, T_m ~329 K) or dipalmitoylphosphatidylcholine (DPPC, T_m ~314 K) [85]. At temperature higher than T_m the liposome bilayer increases its fluidity as well as the water diffusivity and thus the relaxivity..

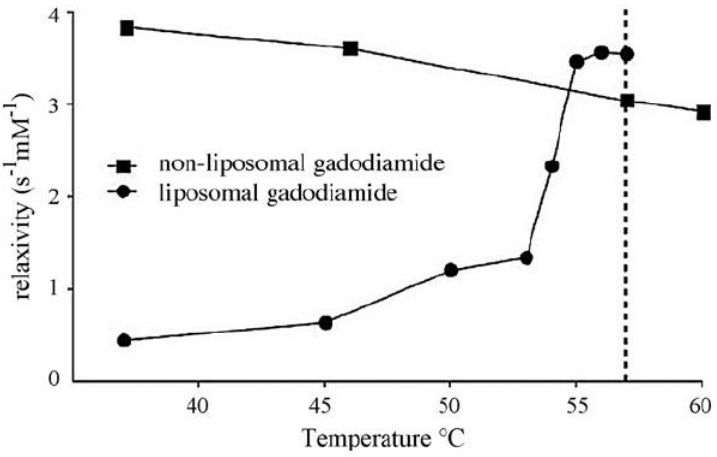

Figure 1.14. Temperature dependence of the relaxivity for Gd-DTPA-BMA free (squares) and encapsulated in DSPC-based liposomes (circles). The vertical dashed line indicates the T_m value of the bilayer. Adapted from ref. [86].

In addition, also the stability of the vesicle decreases and the consequent release of the encapsulated imaging reporter accounts for the observed relaxivity enhancement.
Figure 1.14 reports the comparison between the temperature dependence of the relaxivity of Gd-DTPA-BMA free and encapsulated in DSPC-based liposomes [80]. The data highlights the relaxivity "quenching" occurring at $T < T_m$ due to the low water permeability of the DSPC bilayer, and its increase when the temperature is approaching the phase transition temperature. This temperature-sensitive liposomal MRI agent was also successfully tested in vivo with the aim at guiding hyperthermia

ablation in a tumour model on rabbit liver [86]. Figure 1.15 reports a series of T_{1w} MR images obtained during the localized RF heating of the tumour (indicated by a white arrow), which clearly indicate the appearance of a bright region in the surrounding of the treated lesion caused by the release of the Gd^{3+} chelate from the temperature-sensitive liposomal agent.

A more exhaustive list of examples illustrating the great potential of the so called thermosensitive liposomes (TSL) for guiding heating-based therapies is reported in the review by Lindner et al. [87]. An improvement of the potential of TSL has been recently reported by Terreno et al., who proposed a method, based on the measurement of the ratio between the paramagnetic contributions to the transverse (R_{2p}) and the longitudinal (R_{1p}) relaxation rates, which allows of the idenpendent evaluation of the actual concentration of TSL [88].

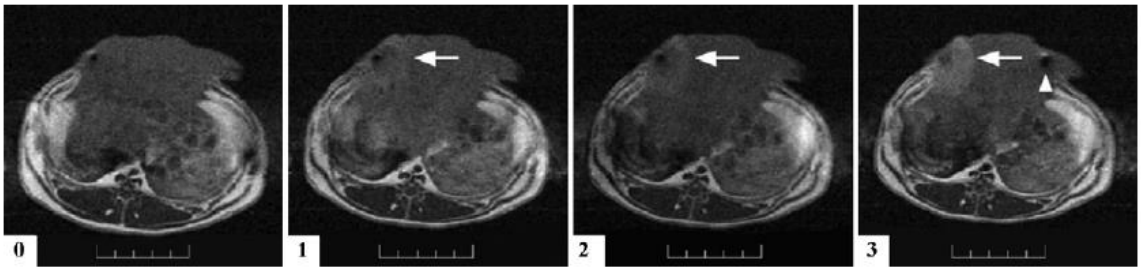

Figure 1.15. T_{1w} MR images of RF ablation in rabbit liver after i.v. injection of the liposomal contrast agent at different steps: prior heating (t_0), during heating (t_1), after normalization of tissue temperature (t_2), and 15–20 min after normalization of tissue temperature (t_3). Note the increasing of the signal intensity in the periphery of the lesion (white arrow). Adapted from ref. [86].

In principle, the improvement of the T_1-relaxing efficiency of liposomes encapsulating the imaging reporter can be pursued by using small sized vesicles (SUV) endowed with high water permeability, but, unfortunately, the increase of the water diffusivity of the membrane is usually accompanied with a significant decrease of the in vivo stability of the liposome.

An alternative approach consists of designing liposomes in which the imaging reporter is incorporated in the vesicle bilayer. The relaxivity enhancement of the incorporated probe with respect to the encapsulated one relies on the lengthening of the

reorientational correlation time, τ_R, of the former system, that improve the efficiency of the dipolar coupling between the unpaired electrons of the paramagnetic ion and the water protons. Since this coupling varies as a function of the magnetic field strength, the NMRD profiles of liposomes incorporating Gd^{3+}-complexes are characterized by the typical relaxivity hump, centred at about 1 T, usually observed for slow-tumbling paramagnetic systems [89,90]. The relaxation enhancement of liposomes incorporating Gd^{3+}-complexes is determined by the structural and dynamic properties of the coordination cage of the metal complex. The most relevant parameter is the water exchange rate, k_{ex}, of the metal coordinated water that has to be finely tuned in order to maximize the overall relaxivity of the system. It has been calculated that k_{ex} values of 10^8 to 10^9 s^{-1} are optimal to achieve high relaxivities [91]. Two routes have been followed for conjugating the lipophilic chains to the coordination cage of the metal complex: (i) through the formation of amide bonds involving the carboxylic groups of the acyclic ligand DTPA, and (ii) through linkages that minimize the chemical characteristics of the donor atoms of macrocyclic (DOTA-based) ligands. The first approach has been extensively used, mainly for the relative easiness in the ligand synthesis, but it has two major disadvantages: (i) the thermodynamic and kinetic stabilities of DTPA amides appear too low for the set-up of safe in vivo applications as those required in typical Molecular Imaging protocols[92], and (ii) the k_{ex} values for this type of coordination cage is much lower than optimal ($\leq 10^6$ s^{-1}), thus "quenching" the relaxivity attainable with these nanoprobes. Conversely, DOTA-like macrocyclic structures, besides a much higher chemical stability, display k_{ex} values closer to the optimum, even if one of the carboxylate groups is functionalized with the lipophilic tail/s through an amidic bond. Support to this view is nicely gained by comparing the relaxivities measured at 0.47 T for the membrane incorporated Gd^{3+}-complexes of bis-stearylamide DTPA (ranging from 8 to 12 mM_{Gd}^{-1} s^{-1} depending on temperature and liposome formulation) [93,94] and for the corresponding systems incorporating the amphiphilic DOTA-based compounds (from 25 to 45 mM_{Gd}^{-1} s^{-1}) [90,95].

Liposomes incorporating Gd^{3+}-complexes have been successfully used in many in vivo MRI applications on animal models including the visualization of tumors either by passive [93] or active [96,97] targeting (Figure 1.16), detection of atherosclerotic plaques [98], lymph nodes [99], inflammation sites [100], and visualization of myocardium infarcted areas [101].

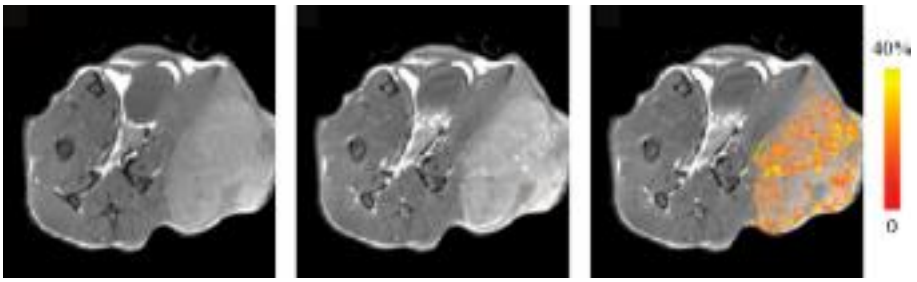

Figure 1.16. MR images on a xenografted tumor animal model before (left image) and after (middle image) injection with paramagnetic liposomes targeting a neo-angiogenesis marker ($\alpha_v\beta_3$ integrin) and incorporating a Gd^{3+}-complexes. Pixels in tumor with signal enhancement of at least 5 times the noise level were color coded (right image). Adapted from ref. [97].

Interestingly, the selective tumor distribution of paramagnetic liposomes targeting an angiogenesis marker ($\alpha_v\beta_3$ integrin) has been recently exploited for in vivo monitoring the therapeutic efficacy of antiangiogenetic drugs by MRI[102]. An additional advantage of using nanosized assembled systems deals with the novel frontier of multimodal imaging. Liposomes appear excellent systems for designing probes containing imaging reporters that can be visualized with different imaging modalities.

Most of the work in this field has been carried out by combining MRI and Optical imaging probes and it has been recently reviewed by Mulder *et al.* [103].

In the late 1980s, it was reported that paramagnetic low molecular weight Dy^{3+}-complexes can act as T_2-susceptibility agents in MRI images when they are unequally distributed in vessels and in the surrounding tissues [104,105]. The effect can be further enhanced when the paramagnetic complexes are entrapped in vesicles such as liposomes[81,106]. The observed behavior is well accounted for in terms of the field gradients created by the compartment containing the paramagnetic ions that induce

the spin dephasing of the water protons diffusing in the outer region of the compartment.

It is straightforward to note that any nanosized system containing paramagnetic metal ions would act as a T_2-susceptibility agent. In this context, paramagnetic liposomes have a high potential owing to the high payload of paramagnetic complexes that can be either entrapped in their inner cavities or, upon suitable functionalization with lipophilic substituent, be incorporated in their membrane bilayer[107].

Figure 1.17 (on the left) compares the R_2 values measured for an aqueous suspension of paramagnetic liposomes encapsulating DyHPDO3A and an aqueous solution containing the same total concentration of the paramagnetic metal ion. The transverse relaxation rate of the nanosized system is almost one order of magnitude higher at the magnetic field strength of 7 T. The R_2-enhancement generated by the susceptibility effect is also evident in the in vitro MR image (Figure 1.17 on the right).

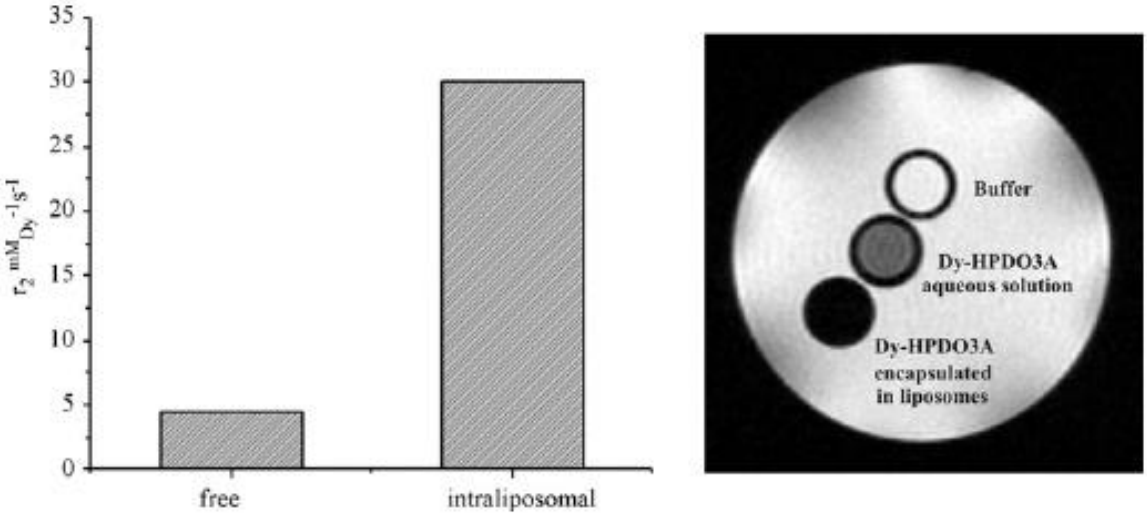

Figure 1.17. Left: Effect of the liposome compartmentalization of a paramagnetic complex (Dy-HPDO3A) on the transverse rates at 7 T and 312 K. Right: In vitro RARE T_{2w} MR image obtained at 7 T and 312 K.

When normalized to the liposome concentration (in mmol/L), the transverse relaxivity ranges from 10^6 to 10^9 $(mM_{Lipo}\ s)^{-1}$ (depending on the size and on the amount of

paramagnetic complex) at 7 T and 298 K. The high T_2-relaxing efficiency displayed by these nanoprobes makes them very suitable for Molecular Imaging purposes.

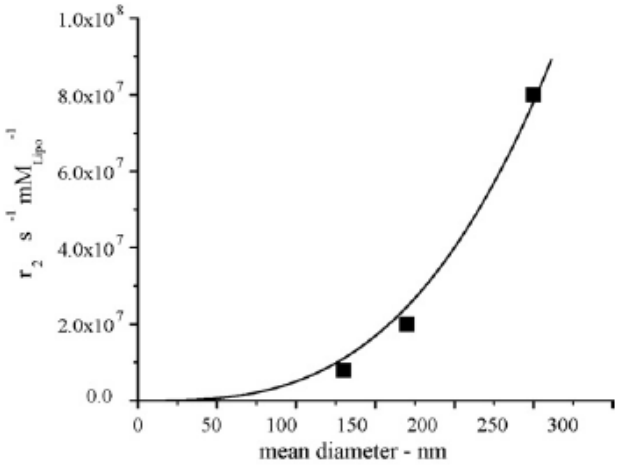

Figure 1.18. Size dependence of the transverse relaxivity (normalized to the liposome concentration) of POPC/Chol/DSPE-PEG2000 (55/40/5 in moles) liposomes encapsulated with a 200 mM solution of Gd-HPDO3A (14 T, 298 K). The line was only drawn for guiding eyes.

The T_2-susceptibility effect is also markedly dependent on the size of the vesicle entrapping the paramagnetic species as reported in Figure 1.18, where the transverse relaxivities of liposomes with different size, but filled up with the same concentration of Gd-HPDO3A, are compared. The reported R_2-enhancement results from the increase of the number of paramagnetic centres encapsulated in the liposome cavity, which is proportional to vesicle volume.

1.4.3 Blood pool agents

Blood pool agents (BPA) or intravascular agents are significantly larger in size than ECF agents and have higher r_1 relaxivities. Because of these characteristics, they offer many advantages in MRA relative to ECF agents. Their high molecular weight (>20 kDa) prevents leakage into the interstitium and they remain in the intravascular system for a prolonged time compared with conventional ECF agents. The long intravascular half-life and the high r_1 relaxivity allow imaging of the vasculature with

higher vessel-to-background signal ratio[108]. At the same time, their r_2 relaxivity must be low enough to avoid excessive signal loss due to T_2/T_2 * relaxation. By selectively reducing the T_1 of blood, high-quality angiograms can be obtained, including coronary artery imaging [109]. The concentration of the CA in the plasma remains stable over one hour, as its mainly renal elimination requires the previous degradation of the macromolecule. This extends the imaging window from about 1 min to about 1 h. This advantage of BPAs over ECF agents of longer image acquisition times allows higher resolution and/or better signal-to-noise ratio and leads to better-quality angiograms of several organs using respiratory or cardiac gating techniques. Vascular abnormalities, associated with certain tumors or atherosclerosis, can be detected and MR mammography is feasible [110]. Another advantage of using BPAs is that tissue blood volume and perfusion can be measured. Blood pool-enhanced MRA in the equilibrium phase (or steady state), as opposed to imaging during the initial arterial passage of the CA, offers the advantage of allowing the enhancement of both arteries and veins.

The blood pool CAs can be divided into several classes, according to their mechanism of action: (a) the noncovalent binding of low molecular weight Gd^{3+} -based complexes to human serum albumin (HSA), which is the most abundant plasma protein (0.67 mM or 4.5% concentration in the blood plasma), prevents immediate leakage into the interstitial space; (b) systems based on polymers or liposomes, based on an increase in the size of the CA molecule, which slows down leakage through endothelial pores; and (c) systems based on particles, involving a change in the route of elimination. Other systems that are also being explored are small ECF Gd^{3+} complexes and Mn^{2+} -labeled hydroxyapatite particles.

Albumin-binding gadolinium complexes are the most successful approach so far. In this class, several complexes have been synthesized by attaching a hydrophobic moiety to a chelating agent, such as [Gd(DOTA-BOM3)] [111]. The most successful among these is the Gd^{3+} complex gadofosveset trisodium, previously known as MS-325 (Figure 1.22), which became the first commercial agent in this class (Vasovist, Bayer Schering Pharma AG). It binds strongly and reversibly to serum albumin [112], leading to high relaxivity at clinical field strengths and much longer residence times in the blood compared with extracellular agents [113]. Several clinical studies have demonstrated its

efficacy in enhancing blood vessels, both in first-pass and in delayed steady-state MRA examinations.

The second most valuable compound in this class is B-22956 or gadocoletic acid (Figure 1.19; Bracco SpA) B-22956 is a Gd-DTPA derivative containing a cholic acid moiety with strong albumin binding [114]. This again leads to much longer residence times in the blood and a higher relaxivity compared with the unbound form of the CA. B-22956 has been investigated for MR coronary artery imaging in clinical trials and to follow antiangiogenesis therapy [115], but is not yet commercially available.

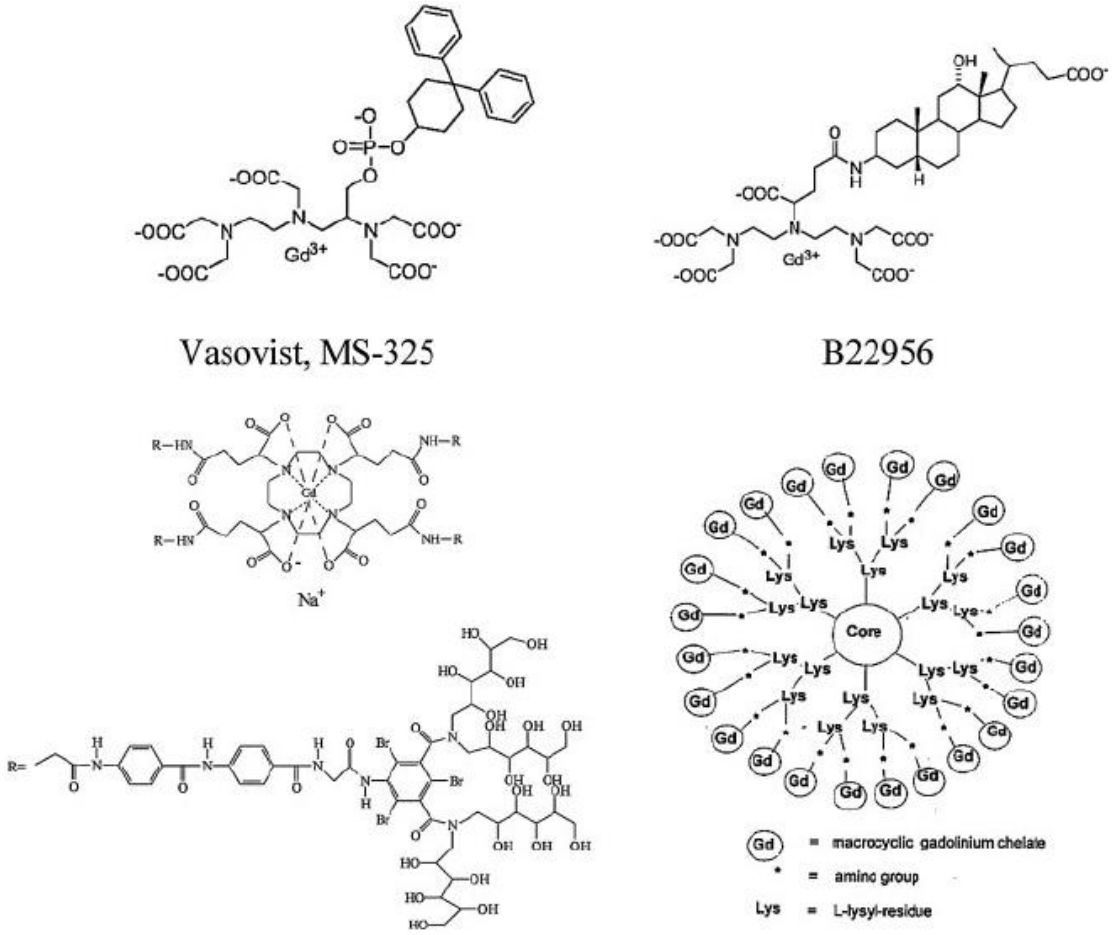

Figure 1.19. Structures of some HSA-binding and polymeric Gd^{3+} complexes, as potential or approved blood pool CAs for MRA (simplified structure for Gadomer 17) (9,46,55). [*Geraldes et al 2009*].

The albumin-binding Gd^{3+} complexes have a wide range of applications besides MRA, e.g. Dynamic Contrast Enhanced (DCE) MRI, breast MRI, perfusion MRI, lung

perfusion, etc. Malignant tumors often show an increased uptake and metabolism of plasma proteins, especially albumin. Macromolecular CAs are delivered to all tissues, but only accumulate in those with leaky vessels near tumor capillaries (tumor neo-vessels). The outcome of tumor therapy can be followed using MRI tumor perfusion studies with Gd^{3+} -labeled albumin using the quantitative decrease in the MR signal of the malignant tissue after therapy.

The large size of polymeric Gd^{3+} chelates is responsible for the slow (or absent) leakage of this class of CAs into the interstitial space through the normal endothelium of the vascular system, thus providing long imaging windows. Various polymeric agents (e.g. dextrans and polylysine derivatives) with molecular weights in the 15–5000 kDa range were evaluated, but did not pass beyond the preclinical stage [116]. Their large size leads to slow rotational dynamics and increased relaxivity at clinical field strengths. Excretion of Gd^{3+} -based macromolecular CAs is related to their size. Since the molecular weight of these large molecules exceeds 40 kDa, glomerular filtration decreases, which could lead to problems with their excretion, even if they are excellent MRA agents.

An example of this class of CAs undergoing clinical trials is Gadomer 17 (Bayer Schering Pharma AG), which carries 24 Gd^{3+} ions [117]. Because of their size (molecular weight 35 kDa), Gadomer 17 molecules are large enough to show much slower leakage through normally functioning endothelium than extracellular agents, but are still small enough to be eliminated via the kidneys. Imaging studies in animals have resulted in excellent angiograms, allowing quantitative perfusion studies of the myocardium. It has been also successfully employed to demonstrate differences in endothelial permeability between tumors and healthy tissue [118].

(Gd-DTPA)45-HSA is another example of this type of CA. Aime et al. [119]]have studied the frequency and temperature dependence of proton and oxygen-17 relaxivities of this CA. The observed behavior is typical of systems whose relaxivity is limited by a long exchange lifetime of the coordinated water molecule [120].

Sieving et al. (50) have synthesized a poly-(L-lysine) containing 60–90 chelating groups (DTPA or DOTA). Complexed with Gd^{3+} ions, the paramagnetic chains were conjugated to HSA. The relatively small relaxation enhancement shown by Gd^{3+} complexes when bound to polylysine is accounted for by the high internal mobility of

the paramagnetic moiety. An analogous result has been observed using the squaric acid unit as a linker between the macromolecule and the Gd chelates [121]. Another agent of this class undergoing clinical trials is P-792 (Gadomelitol, Vistarem1, Guerbet), a hydrophilic high molecular weight derivative of Gd-DOTA. This is a rapid clearance blood pool agent, owing to its limited diffusion across the normal endothelium, with high proton relaxivities r_1 and r_2 in the current range of clinical imaging magnetic fields [122].

The polymeric agent (Gd-DTPA)n-polylysine, under development (PLLGd-DTPA, preclin., Bayer Schering Pharma AG), shows advantages in MRA, in perfusion studies of the myocardium and lung perfusion, and in the differential diagnosis of tumors. However, none of the polymeric Gd^{3+} complex CAs are yet commercially available. The loading of micelles and liposomes with amphiphilic polychelate polymers has been reported also and different paramagnetic agents have been encapsulated into the liposomes [123]. However, these studies did not lead to any agent which passed the preclinical status.

1.4.4.2 Organ-specific agents

The diagnosis of hepatic lesions continues to be a problem even though many diagnostic methods are available. Despite the high contrast resolution of T_2-weighted MRI techniques, a number of pathologies are difficult to detect or differentiate without CAs. ECF agents (e.g. Magnevist) rapidly distribute in the vascular and interstitial space, but do not pass plasma membranes and thus have negligible hepatocellular uptake and biliary excretion. Targeting the hepatocytes or entrapping substances in macrophages of the reticuloendothelial system (RES) are effective approaches for liver-specific agents since both pathways have a high capacity for handling relatively unspecific materials.

Several compounds with different magnetic properties are currently in clinical use, trials, or in preclinical development. They are divided in two main categories: (a) agents targeting hepatocytes—small paramagnetic complexes; and (b) agents targeting the RES— magnetic particles and magnetic liposomes.

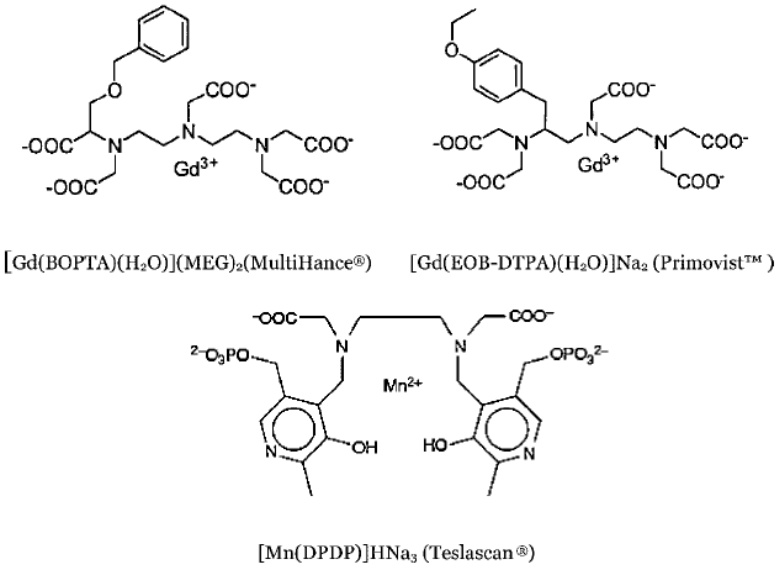

Figure 1.20. Chemical structures of the water-soluble paramagnetic chelates with hepatobiliary uptake in clinical use.

The small water-soluble paramagnetic chelates with hepatobiliary uptake in clinical use (see ligand structures in Figure 1.20) are the Gd-DTPA derivatives [Gd(EOB-DTPA)(H_2O)]Na_2 [gadoxetic acid disodium, PrimovistTM (formerly Eovist 1), Bayer Schering Pharma AG] and [Gd(BOPTA)(H_2O)](MEG)$_2$ (gadobenate dimeglumine, MultiHance, Bracco SpA) and the Mn^{2+} chelate [Mn(DPDP)]HNa_3 (mangafodipir trisodium, Teslascan, GE Healthcare).

The extracellular Gd-DTPA-type derivatives exhibit the most useful characteristics. Both have one lipophilic residue attached to the DTPA backbone that targets the agent to an organic anion transporter in the sinusoidal plasma membrane of the hepatocyte. The uptake by hepatocytes decreases T_1 and increases the signal intensity of normal liver parenchyma, giving a positive contrast relative to other tissues. These CAs display a very pronounced hydrophilic character and relatively low plasma protein binding, despite the presence of the lipophilic moiety, which gives them an acute intravenous tolerance as good as that of Magnevist. [Gd(EOB-DTPA)(H_2O)]$^{2-}$, with the ethoxybenzyl group [124], is completely eliminated from the body, with 50%

hepatobiliary and 50% renal excretion. After entering the intracellular space of the hepatocyte, it is sequestered in the bile. The excretion through the bile and feces causes the bile ducts and the gall bladder to display a very short T_1, which makes contrast-enhanced cholangiography possible. Shortly after administration, the compound distributes in the vascular system in the same way as Magnevist1 , allowing the blood vessels to be seen in dynamic imaging studies. While the Gd^{3+} concentration and the signal intensity in blood decrease, the signal of the liver parenchyma increases, reaching maximum brightness 30–60 min after injection [125]. $[Gd(BOPTA)(H_2O)]^{2-}$ has a benzyloxy lipophilic moiety bound to the DTPA backbone at a different position, providing similar properties to the above described chelate [126]. In addition to the liver, it can be used for MRI of brain and spine. Both Gd^{3+} agents significantly bind to HSA, although with at least one order of magnitude lower affinities than for HSA-binding blood pool agents [127]. Because of the resulting increased relaxivity and half-life in blood, they can be also used in MRA applications [128].

$[Mn(DPDP)]^{4-}$ [129] is the first Mn^{2+} complex to be used as contrast agent in clinical trials [130]. The ion is a powerful T_1 relaxation agent because of its five unpaired electrons. This CA, which demonstrates both biliary and renal excretion, has been shown to be a positive and very effective liver enhancer in T_1-weighted images. Pharmacokinetic studies have shown that, shortly after injection, some Mn^{2+} is released in the plasma and the paramagnetic ion accumulates in the liver and other tissues like pancreas and cardiac muscle. Free Mn^{2+} ions are known to accumulate in hepatocytes, although the chemical similarity of DPDP to vitamin B6 may also contribute to hepatocyte uptake. Since Mn^{2+} is a powerful relaxation enhancer, a very small amount (5 mmol/kg) is sufficient to significantly enhance the contrast between the healthy liver parenchyma and focal liver lesions.

Gadofluorine 8 (Bayer Schering Pharma AG) is a lipophilic but water-soluble gadolinium complex that accumulates in normal lymph nodes, resulting in a pronounced increase in their signal intensity, but not in malignant (metastatic) nodes, thus allowing their differential diagnosis [131].

1.4.4 Targeting and cell labelling

Targeted CAs are probes able to recognize specific molecular sites (e.g. cell-specific receptors or transport proteins) at the cellular membrane and to accumulate at those sites, in most cases by becoming trapped in the intracellular space. The development of approaches able to recognize and image a specific molecular marker of a given pathological process or state (molecular imaging), such as inflammation, atherosclerosis, angiogenesis, apoptosis and tumors, makes the task of diagnosis and therapy much easier [132]. Thus, the development of high affinity ligands as targeting vectors and their conjugation to Gd^{3+} chelates as reporter groups (Figure 1.21, A) is one of the requirements for efficient molecular probes.

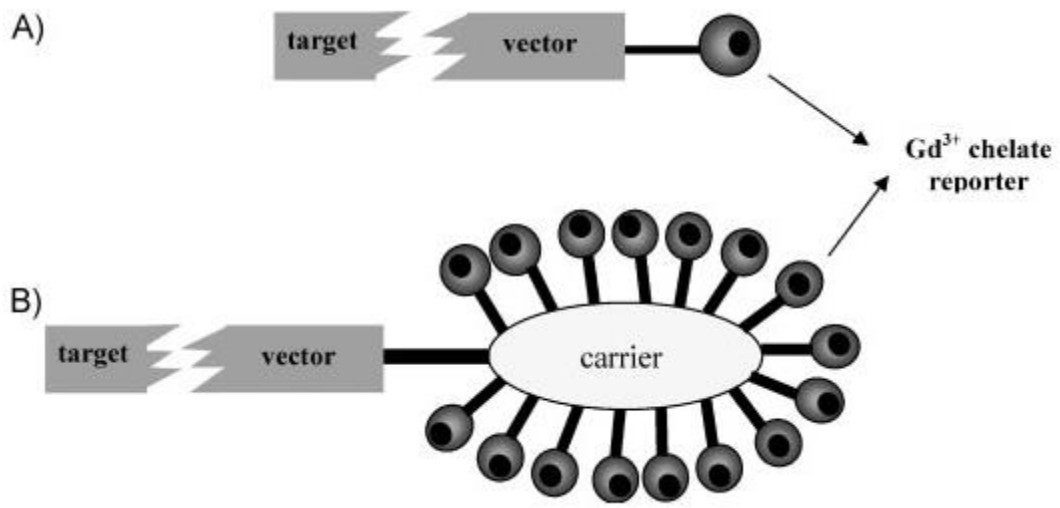

Figure 1.21. General structure of a targeted CA for cell labeling: (A) with a single reporter group; (B) with a carrier of many reporter groups.

However, the main problem of this approach using Gd^{3+} -based contrast agents is MRI's low sensitivity, so that to reach 50% of contrast enhancement it is necessary to have a local concentration of CA of the order of 0.5 mM. It is possible to increase the payload of reporter groups delivered at the target site by using many reporters bound to a single carrier (Figure 1.24, B). However, this combined with the very low concentration of receptors in the cell membrane (10^{-9} –10^{-13} mol/g of tissue) makes it difficult to obtain an image with good contrast. Also, the saturation of all available receptors would interfere with the normal metabolic equilibrium, leading possibly to

cell death [133]. The minimum detectable concentration of a CA depends on its relaxivity. While for [Gd(HPDO3A)] (r_1 = 3.7 mM^{-1} s^{-1} at 90 MHz) this value is too high (5×10^{-7} mol/g or 100 mM), for a sixth-generation dendrimer conjugate substituted with 170 Gd-DTPA chelates (r_1 = 5800 mM^{-1} s^{-1} per dendrimer) it has a manageable value (1.9×10^{-10} mol/g). The main targeting strategies are cell surface or receptor targeting. In the first approach, specific epitopes easily available at the cell surface are targeted. This has been used together with the pretargeting approach to facilitate the detection and imaging of tumor cells (some of which are known to have abnormally high negative charges on their cell surface). This approach consists of two steps, first a positively charged polypeptide, such as polyarginine, interacts on tumor cell surface, then, a negatively charged CA [Gd(DO3A)-R, where R = CH_2–C(=O) N(CH_2–PO_3^{2-})$_2$] is added in order to stick on positively charged polypeptide [134]. The use of low-molecular-weight targeting CAs, able to accumulate quickly at specific cell surface sites, has several advantages with respect to macromolecular agents. One example is the use ofmodified Gd^{3+} chelates able to recognise the abnormal glycosilation of tumor cell surfaces, which have much higher content of sialic acid residues (>10^9 /cell) than normal cells (>10^6 /cell) [135].

Other relevant examples of cell surface targeting result from the well-known nonspecific binding of porphyrins to the interstitial space of tumors, e.g. Dy-TPPS (TPPS = tetraphenylporphyrin sulfonate). One expanded porphyrin (texaphyrin) complex, $[Gd(Tex)]^{2+}$ (PCI-120), selectively accumulates at tumor sites, giving prolonged enhancement of MRI images and the possibility of being used as a radiation sensitizer for brain cancer [136]. Gadophyrin-2 [mesoporphyrin-(GdDTPA)2] (Bayer Schering Pharma AG) targets the necrotic part of tumors, possibly through binding to cell proteins released upon cell death by necrosis. This specific accumulation of necrosis-avid CAs (NACAs) provides a prolonged enhancement of necrotic tissue, especially of myocardial infarcts [136].

The targeting of cell surface receptors can be pursued using labeled antibodies or low-molecular-weight targeting complexes.

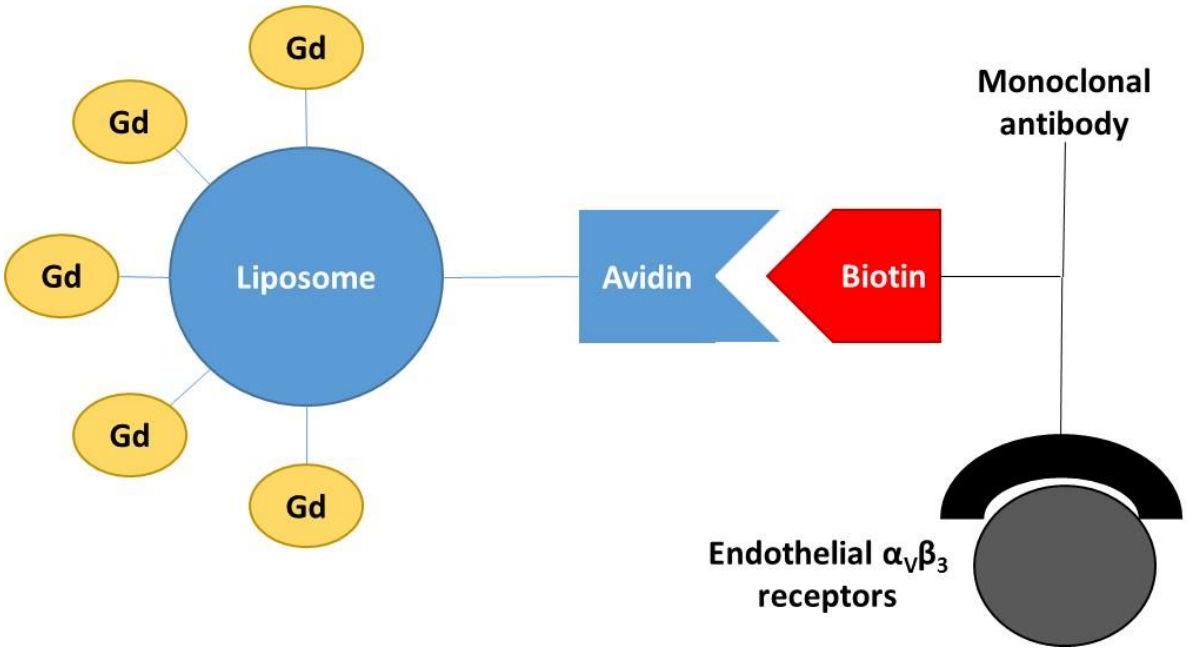

Figure 1.22. Schematic representation of targeting of the endothelial $\alpha_V\beta_3$ angiogenesis marker [138].

In the first approach, due to the slow diffusion of the antibodies, the most accessible targets are those present on the endothelial vessels. A typical example is the targeting of the endothelial integrin receptor $\alpha_V\beta_3$, a specific angiogenesis marker whose concentration correlates with the tumor grade. A Gd^{3+}-containing polymerized liposome was used as an example of an imaging probe containing many reporter groups per carrier. The pretargeting approach was used, where the target was bound first to a biotinylated monoclonal antibody against $\alpha_V\beta_3$, which is well recognized by an avidin moiety present on the liposome surface carrying the Gd^{3+} chelate reporter groups (Figure 1.22) [138].

The same $\alpha_V\beta_3$ target has been addressed with lipidic nanoparticles containing Gd^{3+} chelates [139]. Although the possibility of extensive substitution of some antibodies without loss of immunoreactivity has been demonstrated when they are labeled with liposomes, dendrimers or polymeric chelates, and nanoparticles, the large molecular size and, therefore, the slow delivery of these systems limit the technique.

A more efficient way to accumulate CAs at the target site is by cell internalization processes, which, to be successful, require that the concentration of the agent inside the cell is higher than at the cell surface. These internalization processes may occur via phagocytosis and pinocytosis (or fluid phase endocytosis) mechanisms, which do not require a cell receptor, or receptor mediated endocytosis. Phagocytosis, the process of internalization of particles by cells endowed with phagocytic activity, has been used with Gd-DTPA bis-stearylamide derivatives forming insoluble Gd^{3+} -containing particles that, after internalization, are biodegraded and become soluble and trapped inside the cell [140]. Gd-HPDO3A has been used for labeling stem cells via the pinocytosis mechanism, where the stem cells are incubated in a culture medium containing Gd-HPDO3A in the mM concentration range (10–50 mM) [141]. However, these processes are often very slow and only apply efficiently to undifferentiated, dividing cells. One example of cell internalization by receptor-mediated endocytosis is the entrapment of several units of a CA inside the inner spherical cavity of apoferritin, which after intravenous administration is quickly cleared up by specific receptors on hepatocytes [142]. However, except in the case of internalization by electroporation, where it is delivered to the cytoplasm, the CA is entrapped in the cell endosomic compartment, seriously limiting its relaxivity [143].

Other cell internalization mechanisms have used membrane transporters and transmembrane carrier peptides. These latter have proven useful for the internalization of a number of substrates like proteins, oligonucleotides and plasmid DNA. For instance, translocating signal (MTS) peptides, such as the TAT peptide, made up of a sequence of 10 amino acids from the HIV-1 TAT protein, conjugated to iron oxide nanoparticles or to Gd-DTPA were efficiently internalized [144]. Another interesting development was the synthesis of a bimodal (optical and MRI) imaging probe consisting of a Gd^{3+} /Eu^{3+} -DOTA complex, a PNA (peptide nucleic acid) sequence and a transmembrane carrier peptide. Although the system enters any type of cell, it accumulates only in tumor cells because of the specific binding of the PNA moiety to the c-myc mRNA whose production is upregulated in those cells. This bioshuttle conjugate—transporting the imaging probe into the cytoplasm and then into the nucleus—thus works as a nuclear localization sequence, and has proven to accumulate in the nucleus of DU-145 prostate cancer cells [145].

1.5 Aim of the work

In this introductive chapter, some of the most interesting and applied ways to prepare highly-efficient MRI contrast agents were discussed. The main parameters influencing the relaxivity of a MRI contrast agent were defined and explained, in order to understand which kind of structural requirements a paramagnetic complex must satisfy to optimize its output in terms of r_{1p}, like the number of coordinated water molecules q, the reorientational correlation time τ_R and the residence lifetime of the coordinated water molecules τ_M. A wide overview of systems studying the modulation of these parameters was proposed, with particular attention to those systems that approach the optimization a MRI contrast agent in a similar manner to that reported in the following chapters of this PhD thesis.

As first goal of our work, we will identify, synthesize and characterize an organic ligand to be used as a building block for the development of high-efficiency MRI contrast agents. Thus, the structural, thermodynamic and kinetic properties of the dimeric AAZTA-like complex **Gd_2L** will be described in Chapter 2.

Once detected this well-performing paramagnetic complex, we will use it as a starting point to develop high-relaxivity systems using different approaches.

Focusing our attention on the dependence of relaxivity as a function of τ_R, the dimeric ligand **L** will be functionalized with a hydrophobic group able to form inclusion compounds through non-covalent interactions between the Gd-complex and macromolecules such as β-CDs and poly-β-CDs, or proteins like HSA (Chapter 3).

Furthermore, the covalent binding of this dimeric Gd-complex to a rhodamine functionalized dextran will yield a multimodal imaging probe for *in vivo* neuroanatomical analysis of monosynaptic connections. This work was carried out in collaboration with the Max Planck Institute for Biological Cybernetics, Tubingen, Germany. It will be shown that the derivative containing the dimeric AAZTA moiety gives higher MR contrast enhancement with respect to a mono-AAZTA functionalized dextran (Chapter 4).

Finally, we will synthesize and characterize AAZTA-like mono- and multimeric paramagnetic amphiphilic complexes, bearing lipophilic moieties such as single and/or double aliphatic chains. The development of high-relaxivity lipid nanoparticles including these q = 2 paramagnetic systems will be the target of this Chapter. The aim will be to increase the local rigidity of the amphiphilic complexes by using multimeric complexes and double aliphatic chains to obtain lipidic nanoparticles with optimized efficiency (Chapter 5).

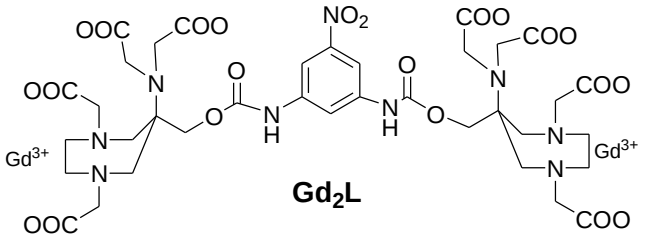

Gd_2L

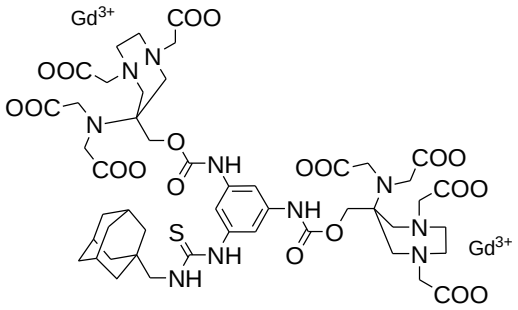

Gd_2L_{Ad}

References

1) S. Aime, M. Botta, M. Fasano, E. Terreno, Chem. Soc. Rev., 1998 , 27, 19–29.

2) S. Aime, M. Botta, M. Fasano, E. Terreno, Acc. Chem. Res., 1999, 32, 941–949.

3) S. Aime, M. Botta, M. Fasano, S. Geninatti Crich, E. Terreno, JBIC 1996, 1, 312–319.

4) E. Toth, D. Pubanz, S. Vauthey, L. Helm, A. E. Merbach, Chem. Eur. J., 1996, 2, 1607–1615.

5) Aime, S.; Botta, M.; Fasano, M.; Terreno, E. Protein-bound metal chelates. In The Chemistry of Contrast Agents in Medical Magnetic Resonance Imaging Merbach, A. E.; Toth, E., Eds.; John Wiley & Sons: Chichester, U.K., 2001; p 969.

6) 4 Aime, S.; Botta, M.; Fasano, M.; Terreno, E. Protein-bound metal chelates. In The Chemistry of Contrast Agents in Medical Magnetic Resonance Imaging Merbach, A. E.; Toth, E., Eds.; John Wiley & Sons: Chichester, U.K., 2001; p 969.

7) Helm, L.; Merbach, A. E. Inorganic and bioinorganic solvent exchange mechanisms. Chem. Rev. 2005, 105, 1923–1959.

8) Baranyai, Z.; Gianolio, E.; Ramalingam, K.; Swenson, R.; Ranganathan, R.; Brucher, E.; Aime, S. The effects of intramolecular H-bond formation on the stability constant and water exchange rate of the Gd(III)-diethylenetriamine-N′-(3-amino-1,1-propylenephosphonic)-N,N,N″,N″-tetraacetate complex. Contrast Media Mol. Imaging 2007, 2, 94–102.

9) Zhang, Z. D.; Greenfield, M. T.; Spiller, M.; McMurry, T. J.; Lauffer, R. B.; Caravan, P. Multilocus binding increases the relaxivity of protein-bound MRI contrast agents. Angew. Chem., Int. Ed. 2005, 44, 6766–6769.

10) Nicolle, G. M.; Helm, L.; Merbach, A. E. S-8 paramagnetic centres in molecular assemblies: Possible effect of their proximity on the water proton relaxivity. Magn. Reson. Chem. 2003, 41, 794–799.

11) Hanaoka, K.; Lubaq, A. J.; Castillo-Muzquiz, A.; Kodadek, T.; Sherry, A. D. The detection limit of a Gd3+ -based T1agent is substantially reduced when targeted to a protein microdomain. Magn. Reson. Imaging 2008, 26, 608–617.
20 21 22 23 24 25

12) 2 D. H. Powell, O. M. Ni Dhubhghaill, D. Pubanz, L. Helm, Y. S. Lebedev, W. Schlaepfer and A. E. Merbach, J. Am. Chem. Soc., 1996, 118, 9333.

13) 4 C. Casali, M. Janier, E. Canet, J. F. Obadia, S. Benderbous, C. Corot and D. Revel, Acad. Radiol., 1998, 5, S214.

14) M. Rohrer, H. Bauer, J. Mintorovitch, M. Requardt and H. J. Weinmann, Invest. Radiol., 2005, 40, 715.

15) M. Port, C. Corot, I. Raynal, J.-M. Idee, A. Dencausse, E. Lancelot, D. Meyer, B. Bonnemain and J. Lautrou, Invest. Radiol., 2001, 36, 445.

16) D. A. Fulton, M. O'Halloran, D. Parker, K. Senanayake, M. Botta and S. Aime, Chem. Commun., 2005, 474.

17) V. Jacques and J. F. Desreux, Top. Curr. Chem., 2002, 221, 123.

18) J. B. Livramento, E. Tòth, A. Sour, A. Borel, A. E. Merbach and R. Ruloff, Angew. Chem., Int. Ed., 2005, 44, 1480.

19) Brasch, R. C. Magn. Reson. Med. 1991, 22, 282-7.

20) Nunn, A. D.; Linder, K.; Tweedle, M. Quart. J. Nuc. Med. 1997, 41, 155-62.

21) Brinkley, M. Bioconjugate Chem. 1992, 3, 2-13.

22) S. Aime, M. Botta, M. Fasano, E. Terreno in The Chemistry of Contrast Agents in Medical Magnetic Resonance Imaging (Eds.: A. E. Merbach, È. Tóth), John Wiley & Sons, Chichester, 2001, ch. 5; b) P. Caravan, Acc. Chem. Res. 2009, 42, 851–862.

23) S. Aime, M. Botta, M. Fasano, S. Geninatti Crich, E. Terreno, J. Biol. Inorg. Chem. 1996, 1, 312–319.

24) a) S. Aime, M. Botta, G. Ermondi, Inorg. Chem. 1992, 31, 4291; b) S. Hoeft, K. Roth, Chem. Ber. 1993, 126, 869; c) S. Aime, M. Botta, M. Fasano, M. P. M. Marques, C. F. G. C. Geraldes, D. Pubanz, A. E. Merbach, Inorg. Chem. 1997, 36, 2059–2068.

25) S. Dumas, V. Jacques, W. C. Sun, J. S. Troughton, J. T. Welch, J. M. Chasse, H. Schmitt-Willich, P. Caravan, Invest. Radiol. 2010, 45, 600–612;

26) V. Jacques, S. Dumas, W. C. Sun, J. S. Troughton, M. T. Greefield, P. Caravan, Invest. Radiol. 2010, 45, 613–624.

27) a) S. Avedano, L. Tei, A. Lombardi, G. B. Giovenzana, S. Aime, D. Longo, M. Botta, Chem. Commun. 2007, 4726–4728; b) M. Botta, S. Avedano, G. B. Giovenzana, A. Lombardi, D.
Longo, C. Cassino, L. Tei, S. Aime, Eur. J. Inorg. Chem. 2011,
802–810.

28) Z. Zhang, M. T. Greenfield, M. Spiller, T. J. McMurry, R. B. Lauffer, P. Caravan, Angew. Chem. 2005, 117, 6924; Angew. Chem. Int. Ed. 2005, 44, 6766.

29) S. Azegami, A. Tsuboi, T. Izumi, M. Hirata, P. L. Dubin, B. Wang, E. Kokufta, Langmuir 1999, 15, 940–947.

30) D. M. J. Doble, M. Botta, J. Wang, S. Aime, A. Barge, K. N. Raymond, J. Am. Chem. Soc. 2001, 123, 10758–10759.

31) E. Gianolio, G. B. Giovenzana, D. Longo, I. Longo, I. Menegotto, S. Aime, Chem. Eur. J. 2007, 13, 5785–5797.

32) W.J.M. Mulder, G.J. Strijkers, G.A.F. van Tilborg, A.W. Griffioen, K. Nicolay, NMR Biomed. 19 (2006) 142.

33) G. Lipari, A. Szabo, J. Am. Chem. Soc. 104 (1982) 4546.

34) G. Lipari, A. Szabo, J. Am. Chem. Soc. 104 (1982) 4559.

35) J.P. Andre, E. Toth, H. Fischer, A. Seelig, H.R. Macke, A.E. Merbach, Chem. Eur. J. 5 (1999) 2977.

36) G.M. Nicolle, E. Toth, K.P. Eisenwiener, H.R. Macke, A.E. Merbach, J. Biol. Inorg. Chem. 7 (2002) 757.

37) R. Hovland, C. Gløgård, A.J. Aasen, J. Klaveness, Org. Biomol. Chem. 1 (2003) 644.

38) G.M. Nicolle, L. Helm, A.E. Merbach, Magn. Reson. Chem. 41 (2003) 794.

39) E. Gianolio, G.B. Giovenzana, D. Longo, I. Longo, I. Menegotto, S. Aime, Chem. Eur. J. 13 (2007) 5785.

40) S. Torres, J. A. Martins, J. P. Andre, C. F. G. C. Geraldes, A. E. Merbach, E. Toth, Chem. Eur. J. 2006, 12, 940–948

41) G. Schuhmann Giampieri, H. Schmitt-Willich, W.R. Press, C. Negishi, H.J. Weinmann, U. Speck, Radiology 183 (1992) 59.

42) G. Vittadini, E. Felder, C. Musu, C. Tirone, Invest. Radiol. 5 (1990) S59.

43) R.B. Lauffer, Chem. Rev. 87 (1987) 901.

44) M. Vaccaro, A. Accardo, D. Tesauro, G. Mangiapia, D. Löf, K. Schillén, O. Söderman, G. Morelli, L. Paduano, Langmuir 22 (2006) 6635.
45) A. Accardo, D. Tesauro, G. Morelli, E. Gianolio, S. Aime, M. Vaccaro, G. Mangiapia, L. Paduano, K. Schillen, J. Biol. Inorg. Chem. 12 (2007) 267.

46) R.W. Storrs, F.D. Tropper, H.Y. Li, C.K. Song, J.K. Kuniyoshi, D.A. Sipkins, K.C.P. Li, M.D. Bednarski, J. Am. Chem. Soc. 117 (1995) 7301.

47) L. Lattuada, G. Lux, Tetrahedron Lett. 44 (2003) 3893.

48) O. Morag, A. Ahmad, N. Kamaly, E. Perouzel, A. Caussin, M. Keller, A. Herlihy, J. Bell, A.D. Miller, M.R. Jorgensen, Org. Biomol. Chem. 4 (2006) 3489.

49) S.K. Kim, G.M. Pohost, G.A. Elgavish, Magn. Reson. Med. 22 (1991) 57.

50) K.S. Kim, G.M. Pohost, G.A. Elgavish, Bioconjugate Chem. 3 (1992) 20.

51) W.J. Chu, T. Simor, G.A. Elgavish, NMR Biomed. 10 (1997) 87.

52) T. Simor, W.J. Chu, L. Johnson, A. Safranko, M.P. Doyle, G.M. Pohost, G.A. Elgavish, Circulation 92 (1995) 3549.

53) C. Gløgård, R. Hovland, S.L. Fossheim, A.J. Aasen, J. Klaveness, J. Chem. Soc. Perkin Trans. 2 (2000) 1047.

54) C. Gløgård, G. Stensrud, R. Hovland, S.L. Fossheim, J. Klaveness, Int. J. Pharm.

233 (2002) 131.

55) C. Gløgård, G. Stensrud, J. Klaveness, Int. J. Pharm. 253 (2003) 39.

56) K. Kimpe, T.N. Parac-Vogt, S. Laurent, C. Pierart, L.V. Elst, R.N. Muller, K. Binnemans, Eur. J. Inorg. Chem. (2003) 3021.

57) T.N. Parac-Vogt, K. Kimpe, S. Laurent, C. Pierart, L.V. Elst, R.N. Muller, Eur. J. Inorg. Chem. 2004 (2004) 3538.

58) T.N. Parac-Vogt, K. Kimpe, S. Laurent, C. Pierart, V.L. Elst, R.N. Muller, K. Binnemans, Eur. Biophys. J. 35 (2006) 136.

59) F. Botteman, G.N. Nicolle, L.V. Elst, S. Laurent, A.E. Merbach, R.N. Muller, Eur. J. Inorg. Chem. 2000 (2002) 2686.

60) S. Laurent, V.L. Elst, C. Thirifays, R.N. Muller, Eur. Biophys. J. 37 (2008) 1007.

61) S.H. Koenig, Q.F. Ahkong, R.D. Brown III, M. Lafleur, M. Spiller, E. Unger, C. Tilcock, Magn. Reson. Med. 23 (1992) 275.

62) D. Huster, A.J. Jin, K. Arnold, K. Gawrisch, Biophys. J. 73 (1997) 855.

63) F. Alhaique, I. Bertini, M. Fragai, M. Carafa, C. Luchinat, G. Parigi, Inorg. Chim. Acta 331 (2002) 151.

64) S. Laurent, L.V. Elst, C. Thirifays, R.N. Muller, Langmuir 24 (2008) 4347.

65) P.L. Anelli, L. Lattuada, V. Lorusso, M. Schneider, H. Tournier, F. Uggeri, MAGMA 12 (2001) 114.

66) H. Tournier, R. Hyacinthe, M. Schneider, Acad. Radiol. 9 (2002) S20.

67) E. Terreno, A. Sanino, C. Carrera, D. Delli Castelli, G.B. Giovenzana, A. Lombardi, R. Mazzon, L. Milone, M. Visigalli, S. Aime, J. Inorg. Biochem. 102 (2008) 1112.

68) C. Tilcock, Adv. Drug Deliv. Rev. 37 (1999) 33.

69) G.J. Strijkers, W.J.M. Mulder, R.B. van Heeswijk, P.M. Frederik, P. Bomans, P.C.M.M. Magusin, K. Nicolay, Magn. Reson. Mater. Phys. 18 (2005) 186.

70) C. Gløgård, G. Stensrud, S. Aime, Magn. Reson. Chem. 41 (2003) 585.

71) N. Kamaly, T. Kalber, A. Ahmad, M.H. Oliver, P.W. So, A.H. Herlihy, J.D. Bell, M.R. Jorgensen, A.D. Miller, Bioconjugate Chem. 19 (2008) 118.

72) V. Weissig, J. Babich, V.P. Torchilin, Colloids Surf. B: Biointerf. 18 (2000) 293.

73) V.S. Trubetskoy, J.A. Cannillo, A. Milshtein, G.L. Wolf, V.P. Torchilin, Magn. Reson. Imag. 13 (1995) 31.

74) A.L. Klibanov, K. Maruyama, V.P. Torchilin, L. Huang, FEBS Lett. 268 (1990) 235.

75) H.M. Patel, S.M. Moghimi, in: G. Gregoriadis, A.C. Allison, G. Poste (Eds.), Targeting of Drugs – Optimization Strategies, Plenum Press, New York, 1990, p. 87.

76) A.D. Bangham, M.M. Standish, J.C. Watkins, J. Mol. Biol. 13 (1965) 238.

77) S.H. Koenig, R.D. Brown III, R. Kurland, S. Ohki, Magn. Reson. Med. 7 (1988) 133.

78) C. Tilcock, E. Unger, P. Cullis, P. MacDougall, Radiology 171 (1989) 77.

79) V.J. Caride, H.D. Sostman, R.J. Winchell, J.C. Gore, Magn. Reson. Imaging 2 (1984) 107.

80) S.L. Fossheim, K.A. Il'asov, J. Hennig, A. Bjornerud, Acad. Radiol. 7 (2000) 1107.

81) S.L. Fossheim, A.K. Fahlvik, J. Klaveness, R.N. Muller, Magn. Reson. Imaging 17 (1999) 83.

82) E.C. Unger, T. Winokur, P. MacDougall, J. Rosenblum, M. Clair, R. Gatenby, C. Tilcock, Radiology 171 (1989) 81.

83) M.R. Niesman, G.C. Bacic, S.M. Wright, H.J. Swartz, R.L. Magin, Invest. Radiol. 25 (1990) 545.

84) K.E. Lokling, R. Skurtveit, K. Dyrstad, J. Klaveness, S.L. Fossheim, Int. J. Pharm. 274 (2004) 75.

85) G. Kong, M.W. Dewhirst, Int. J. Hyperthermia 15 (1999) 345.

86) L. Frich, A. Bjornerud, S. Fossheim, T. Tillung, I. Gladhaug, Magn. Reson. Med. 52 (2004) 1302.

87) L.H. Lindner, H.M. Reinl, M. Schlemmer, R. Stahl, M. Peller, Int. J. Hyperthermia 21 (2005) 575.

88) E. Terreno, A. Bert, W. Dastr ` u, A. Sanino, S. Aime, Proc. Joint Annual Meeting ISMRM-ESMRMB, Berlin, Germany, 2007, p. 252.

89) C. Tilcock, Q.F. Ahkong, S.H. Koenig, R.D. Brown III, M. Davis, G. Kabalka, Magn. Reson. Med. 27 (1992) 44.

90) C. Glogard, G. Stensrud, R. Hovland, S.L. Fossheim, J. Klaveness, Int. J. Pharm. 233 (2002) 131.

91) S. Aime, M. Botta, M. Fasano, E. Terreno, Acc. Chem. Res. 32 (1999) 941.

92) C. Cabella, S. Geninatti Crich, D. Corpillo, A. Barge, C. Ghirelli, E. Bruno, V. Lorusso, F. Uggeri, S. Aime, Contr. Media Mol. Imaging 1 (2006) 23.

93) I. Bertini, F. Bianchini, L. Calorini, S. Colagrande, M. Fragrai, A. Franchi, O. Gallo, C. Gavazzi, C. Luchinat, Magn. Res. Med. 52 (2004) 669.

94) G.J. Strijkers, W.J.M. Mulder, R.B. Heeswijk, P.M. Frederik, P. Bomans, P.C. Magusin, K. Nicolay, MAGMA 18 (2005) 186.

95) L. Tei, S. Geninatti Crich, B. Bussolati, A. Ciampa, C. Grange, D. Alberti, S. Lanzardo, G. Camussi, S. Aime, Proc. Joint Annual Meeting ISMRM-ESMRMB, Berlin, Germany, 2007, p. 256.

96) D.A. Sipkins, D.A. Cheresh, M.R. Kazemi, L.M. Nevin, M.D. Bednarski, K.C. Li, Nat. Med. 4 (1998) 623.

97) W.J. Mulder, G.J. Strijkers, J.W. Habets, E.J. Bleeker, D.W. van der Schaft, G. Storm, G.A. Koning, A.W. Griffioen, K. Nicolay, FASEB J. 19 (2005) 2008.

98) W.J.M. Mulder, K. Douma, G.A. Koning, M.A. van Zandvoort, E. Lutgens, M.J. Daemen, K. Nicolay, G.J. Strijkers, Magn. Reson. Med. 55 (2006) 1170.

99) V.S. Trubetskoy, J.A. Cannillo, A. Milshtein, G.L. Wolf, V.P. Torchilin, Magn. Reson. Imaging 13 (1995) 31.

100) D.A. Sipkins, K. Gijbels, F.D. Tropper, M. Bednarski, K.C. Li, L. Steinman, J. Neuroimmunol. 104 (2000) 1.

101) W.J. Chu, T. Simor, G.A. Elgavish, NMR Biomed. 10 (1997) 87.

102) W.J. Mulder, D.W. van der Schaft, P.A.I. Hautvast, G.J. Strijkers, G.A. Koning, G. Storm, K.H. Mayo, A.W. Griffionen, K. Nicolay, FASEB J. 21 (2007) 378.

103) W.J. Mulder, A.W. Griffionen, G.J. Strijkers, D.P. Cormode, K. Nicolay, Z.A. Fayad, Nanomedicine 2 (2007) 307.

104) B.R. Rosen, J.W. Belliveau, H.J. Aronen, D. Kennedy, B.R. Buchbinder, A. Fischman, M. Gruber, J. Glas, R.M. Weisskoff, M.S. Cohen, F.H. Hochberg, T.J. Brady, Magn. Reson. Med. 22 (1991) 293.

105) L.M. Hamberg, R. MacFarlane, E. Tasdemiroglu, P. Boccalini, G.J. Hunter, J.W. Belliveau, M.A. Moskowitz, B.R. Rosen, Stroke 24 (1993) 444.

106) S.L. Fossheim, K.E. Kellar, A.H. Fahlvik, J. Klaveness, Magn. Reson. Imaging (1997) 193.

107) E. Terreno, C. Cabella, C. Carrera, D. Delli Castelli, S. Lanzardo, R. Mazzon, S. Rollet, M. Visigalli, S. Aime, Proc. Joint Annual Meeting ISMRM-ESMRMB, Berlin, Germany, 2007, p. 248.

108) Knopp MV, von Tengg-Koblingk H, Floemer F, Schoenberg SO. J. Magn. Reson. Imag. 1999; 10: 314–331.

109) Saeed M, Wendland MF, Higgins CB., J. Magn. Reson. Imag. 2001; 12: 890–898.

110) Daldrup-Link H, Brasch RC, Eur. Radiol. 2003; 13: 354–365.

111) Aime S, Botta M, Fasano M, Crich SG, Terreno E. J. Biol. Inorg. Chem. 1996; 1: 312–319.

112) Lauffer RB, Parmelee DJ, Dunham SU, Ouellet HS, Dolan RP, Witte S, McMurry TJ, Walovitch RC. Radiology 1998; 207: 529–538.

113) Rohrer M, Bauer H, Mintorovitch J, Requardt M, Weinmann H-J. Invest. Radiol. 2005; 40: 715–724.

114) Cavagna FM, Lorusso V, Anelli PL, Maggioni F, de Hae ¨n C. Acad. Radiol. 2002; 9: 491–494.

115) Preda A, Novikov V, Mo ¨ glich M, Turetschek K, Shames DM, Brasch RC, Cavagna FM, Roberts TPL, J. Magn. Reson. Imag. 2004; 20: 865–873.

116) Dong Q, Hurst DR, Weinmann HJ, Chenevert TJ, Londy FJ, Prince MR. Invest. Radiol. 1998; 33: 699–708.

117) Misselwitz B, Schmitt-Willich H, Ebert W, Frenzel T, Weinmann HJ., MAGMA 2001; 12: 128–134.

118) Kobayashi H, Brechbiel MW., Curr. Pharm. Biotechnol. 2004; 5: 539–549.

119) Aime S, Fasano M, Terreno E, Botta M., Merbach AE, Tçth E (eds). Wiley: Chichester, 2001; 193–241.

120) Berthezèe Y, Vexler V, Price DC, Wisner-Dupon J, Moseley ME, Aicher KP, Brasch RC., Invest. Radiol, 1992; 27: 346–351.

121) Aime S, Botta M, Crich SG, Giovenzana G, Palmisano G, Sisti M., Bioconjug. Chem. 1999; 10: 192–199.

122)vCorot C, Violas X, Robert P, Gagneur G, Port M., Invest. Radiol. 2003; 38: 311–319.

123) Lokling KE, Fossheim SL, Skurtveit R, Bjornerud A, Klaveness, Magn. Reson. Imag. 2001; 19: 731–738.

124) Schmitt-Willich H, Brehm M, Evers CLJ, Michl G, Muller-Fahrnow A, Petrov O, Platzek J, Raduchel B, Sulzle D., Inorg. Chem. 1999; 38: 1134–1144.

125) Schuhmann-Giampieri G, Schmitt-Willich H, Press WR, Negishi C, Weinmann HJ, Speck U., Radiology 1992; 183: 59–64.

126) Uggeri F, Aime S, Anelli PL, Botta M, Brocchetta M, Dehaen C, Ermondi G, Grandi M, Paoli P., Inorg. Chem. 1995; 34: 663–642.

127) Henrotte V, Vander Elst L, Laurent S, Muller RN., J. Biol. Inorg. Chem. 2007; 12: 929–937.

128) Knopp MV, Schoenberg SO, Rehm C, Floemer F, von Teregg-Kobling KH, Bock M, Hentrich HR., Invest. Radiol. 2002; 37: 706–715.

129) Saini S, Nelson RC., Radiology 1995; 197: 575–577.

130) Lim KO, Stark DD, Leese PT, Pfefferbaum A, Rocklage SM, Quay SC., Radiology 1991; 178: 79–82.

131) Misselwitz B, Platzek J, Radu¨ chel B, Oellinger JJ, Weinmann H-J., MAGMA 1999; 8: 1352–8661.

132) Bogdanov AA, Lewin M, Weissleder R., Adv. Drug Deliv. Rev. 1999; 37: 279–293.

133) Nunn AD, Linder KE, Tweedle MF., Q.J. Nucl. Med. 1997; 41: 155–162.

134) Aime S, Botta M, Garino E, Crich SG, Giovenzana G, Pagliarin R, Palmisano G, Sisti M., Chem.Eur. J. 2000; 6: 2609–2617.

135) Frullano L, Rohovec J, Aime S, Maschmeyer T, Prata MIM, de Lima JJP, Geraldes CFGC, Peters JA., Chem. Eur. J. 2004; 10: 5205–5217.

136) Young SW, Quing F, Harriman A, Sessler JL, Dow WC, Mody TD, Hemmi GW, Hao Y, Miller RA, Proc. Natl Acad. Sci. USA. 1996; 93: 6610–6615.

137) Ni Y, Pislaru C, Bosmans H, Pislaru S, Miao Y, Bogaert J, Dymarkowski S, Yu J, Semmler W, Van de Werf F, Baert AL, Marchal G., Eur. Radiol. 2001; 11: 876–883.

138) Sipkins DA, Cheresh DA, Kazemi MR, Nevin LM, Bednarski MD, Li KC.. Nat. Med. 1998; 4: 623–626.

139) Winter PM, Caruthers SD, Kassner A, Harris TD, Chinen LK, Allen JS, Lacy EK, Zhang H, Robertson JD, Wickline SA, Lanza GM., Cancer Res. 2003; 63: 5838–5843.

140) Aime S, Cabella C, Colombatto S, Geninatti Crich S, Gianolio E, Maggioni F., J.Magn. Reson. Imag. 2002; 16: 394–406.

141) Crich SG, Biancone L, Cantaluppi V, Duo D, Esposito G, Russo S, Camussi G, Aime S., Magn. Reson. Med. 2004; 51: 938–944.

142) Aime S, Frullano L, Crich SG., Angew. Chem. Int. Edn Engl. 2002; 41: 1017–1019.

143) Terreno E, Crich SG, Belfiore S, Biancone L, Cabella C, Esposito G, Manazza AD, Aime S., Magn. Reson. Med. 2006; 55: 491–497.

144) Bhorade R, Weissleder R, Nakakoshi T, Moore A, Tung CH., Bioconjug. Chem. 2000; 11: 301–305.

145) Heckl S, Pipkorn R, Waldeck W, Spring H, Jenne J, von der Lieth CW, Corban-Wilhelm H, Debus J, Braun K., Cancer Res. 2003; 63: 4766–4772.

2. AAZTA-Dimer, a novel building block for high relaxivity systems

In the introduction chapter some of the most known and common ways to obtain high-efficiency contrast agents are reported.

Often, to obtain a suitable probe, a functionalization of the paramagnetic complex is required. Consequently, in first istance is necessary to design a well-performing paramagnetic core as a substrate for the functionalization. In this PhD project a dimeric AAZTA-like complex, **L** (Scheme 2.1), was synthesised and characterized, as a promising building block for the preparation of high-relaxivity systems.

AAZTA and its derivatives have been proposed for diagnostic and therapeutic applications for several reasons: they are relatively easy to synthesise [1] and form thermodynamically stable and kinetically inert complexes with divalent and trivalent metal ions.[2,3] In our earlier work, we found that Gd^{3+}-complexes of the multimeric AAZTA ligands shows excellent relaxation enhancement of the solvent water protons, which can be attributed to the slow reorientational correlation time of the multimeric complexes and the fast exchange between the bulk and two water molecules directly coordinated to the Gd^{3+} ion.[4]

The metal complexes used in the medical diagnosis and therapy must have high thermodynamic stability and kinetic inertness since the free metal ions and ligands are toxic. The detailed equilibrium and kinetic characterization of Gd_2L was performed in order to predict the distribution and the dissociation rate of the Gd^{3+}-complex near physiological conditions.

2.1 Synthetic procedure

The synthesis of the dimeric lignad was carried out starting from 5-nitro-isophthalic acid which was transformed into a bis-acyl azide passing through the acyl chloride . and then performing a substitution with sodium azide in a mixture of NaOH (1.0 mol L^{-1}) and CH_2Cl_2 (Scheme 2.1). The acyl azide was then converted into the isocyanate through Curtius rearrangement refluxing in toluene for 3h.

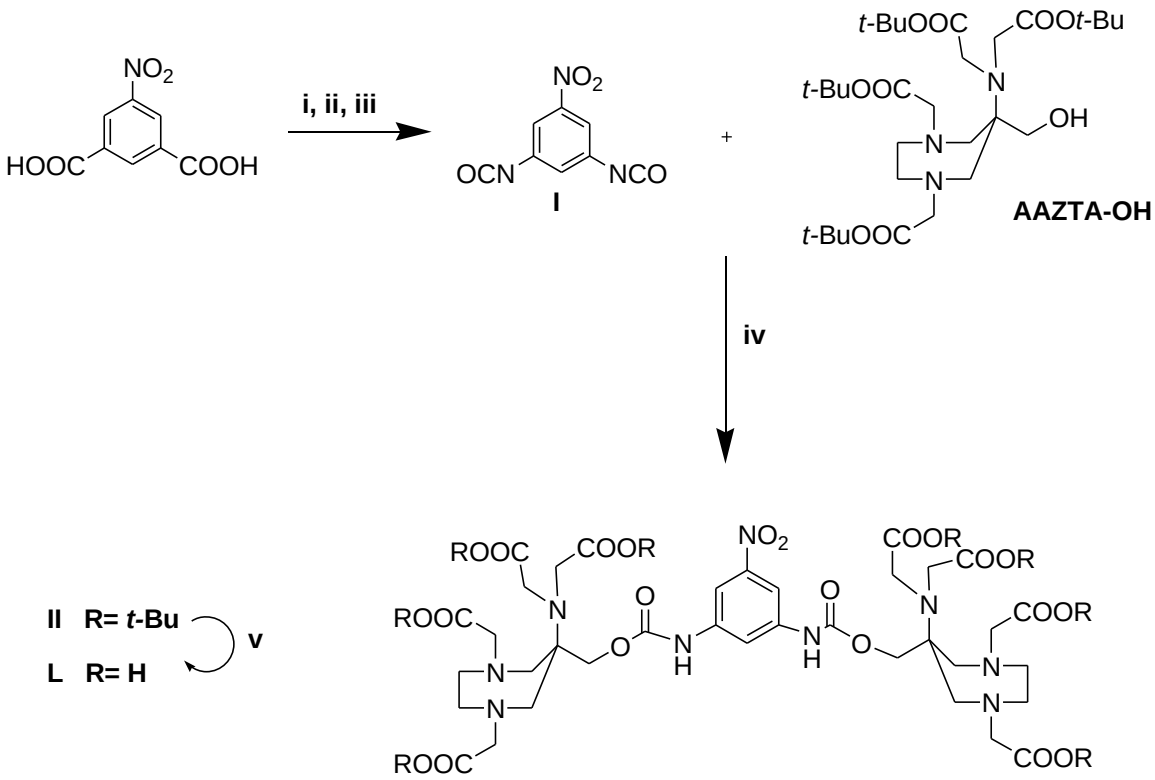

Scheme 2.1: Synthetic procedure to obtain L. Reagents and conditions: i: $SOCl_2$, reflux, 18 h; ii: NaN3, NaOH 1 M/CH_2Cl_2, rt, 1 h; iii: Toluene, reflux, 3 h; iv: CH_2Cl_2, rt, overnight; v: TFA/CH_2Cl_2, rt, overnight.

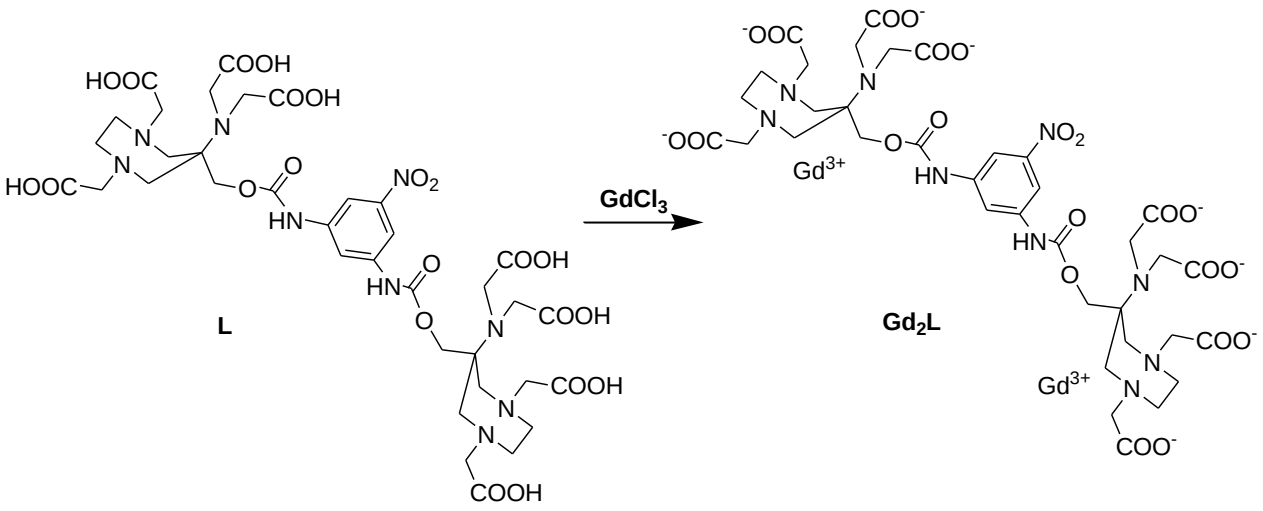

Scheme 2.2: Complexation of L with $GdCl_3$.

The 5-nitro isophthaloyl diisocyanate was then reacted with two equivalents of AAZTA- OH, whose synthesis is reported in literature[gugliotta tei 2009], to obtain the dimeric ligand (**II**) after column chromatographic purification. After purification the final dimeric lingad **L** was obtained by deprotection of the *t*-Bu esters with trifluoroacetic acid in CH_2Cl_2 1:1 v/v.

Eventually, the dimeric Gd^{3+} complex **Gd_2L** was obtained trough relaxometric titration with $GdCl_3$. Once reached the equivalence point, and some free Gd^{3+} is in solution, the complex generates some kind of aggregates that precipitate. To resolubilize the complex a small amount of solid ligand was added, being sure this way that all the Gd^{3+} in solution is complexed.

2.2 Thermodynamic study

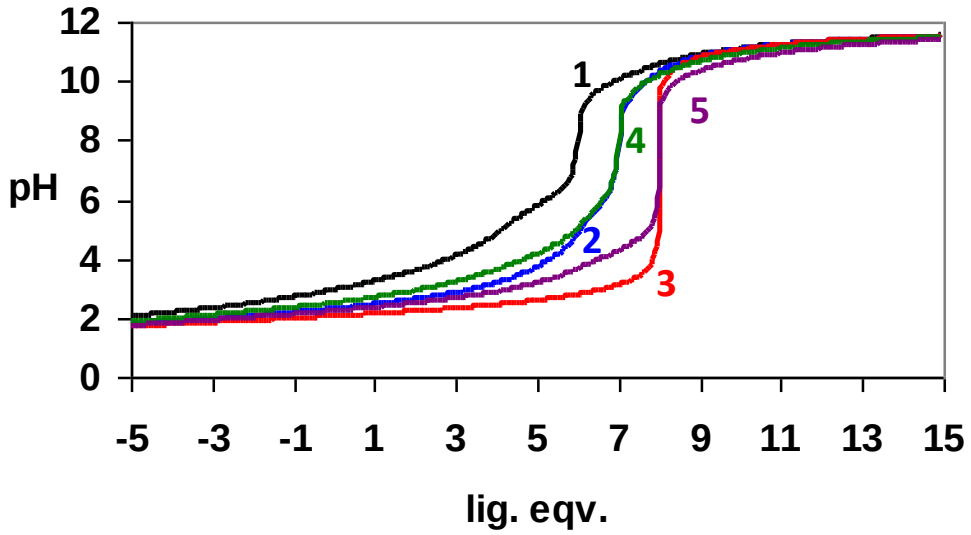

Figure 2.1. pH-potentiometric titration curve of L in the absence (1) and presence of Gd^{3+} and Cu^{2+} ions. ([L]=2.0 mM, [Gd^{3+}]=2.0 mM (2), [Gd^{3+}]=4.0 mM (3), [Cu^{2+}]=2.0 mM (4) and [Cu^{2+}]=4.0 mM (5), [HCl]=10 mM, 0.1 M KCl, 25°C).

In the frame of the Hungarian – Italian Intergovernmental Science & Technology Cooperation Program, a period was spent at the Department of Inorganic and Analytical Chemistry, University of Debrecen were the protonation constants of the dimeric AAZTA ligand **L** were determined and the complexation equilibria of **L** with Gd^{3+} and Cu^{2+} ions investigated.

The detailed equilibrium and kinetic characterization of **Gd_2L** was performed in order to predict the distribution and the dissociation rate of the Gd^{3+}-complex near physiological conditions. In particular, the protonation constants of **L**, the stability and protonation constants of the Gd^{3+} and Cu^{2+}-complexes formed with **L** were determined by pH-potentiometric titrations. The metal-to-ligand concentration ratios used as conditions for the titrations were 1:1 and 2:1 (the concentration of the ligand was generally 0.002 M). For the pH measurements and titration, a *Metrohm 785 DMP Titrino* workstation and a *Metrohm-6.0233.100* combined electrode were used. Equilibrium

measurements were carried out at constant ionic strength (0.1M KCl) in 6 ml samples at 25 °C. The titrations were performed in the pH range 1.7-11.7 stirring the solutions under N_2 atmosphere. The protonation and stability constants were calculated with the program PSEQUAD. The pH-potentiometric titration curve of the **L**, the Gd^{3+}-**L** and Cu^{2+}-**L** systems are shown in Figure 2.1.

	L	**AAZTA**
$\log K_1^H$	10.36 ± 0.01	11.23
$\log K_2^H$	9.96 ± 0.01	6.52
$\log K_3^H$	6.06 ± 0.01	3.78
$\log K_4^H$	5.49 ± 0.02	2.24
$\log K_5^H$	4.20 ± 0.02	1.56
$\log K_6^H$	3.88 ± 0.02	-
$\log K_7^H$	3.12 ± 0.03	-
$\log K_8^H$	2.90 ± 0.03	-
$\log K_9^H$	2.04 ± 0.02	-

Table 2.1: The protonation constants calculated for L.

The comparison of the related log*K* values(Table 2.1), that are a quantitative measure of the strength of an acid in solution, indicates that the protonation behavior of **L** and AAZTA is similar due to the presence of identical protonation sites. However, the log*K* values of the two AAZTA units of **L** are slightly different (by 0.5 log*K* unit) indicating an interaction between the two independent AAZTA units. By taking into account the protonation constants of **L**, the stability and protonation constants of the Gd^{3+} and Cu^{2+}

complexes were calculated from the pH-potentiometric titration curves obtained at 1:1 and 2:1 metal-to-ligand concentration ratios.

	L	**AAZTA**
$\log K_{GdL}$	19.80 ± 0.02	20.24
$\log K_{GdHL}$	9.65 ± 0.02	1.89
$\log K_{GdH2L}$	5.65 ± 0.02	-
$\log K_{GdH3L}$	3.96 ± 0.02	-
$\log K_{GdH4L}$	3.01 ± 0.02	-
$\log K_{GdH5L}$	2.05 ± 0.02	-
$\log K_{Gd2L}$	18.60 ± 0.03	-
$\log K_{Gd2LH}$	2.12 ± 0.03	-

Table 2.2: The protonation constants calculated for GdL and Gd_2L.

The lower stability constant of the dinuclear Gd_2**L** complex with respect to GdAAZTA is probably caused by the lower protonation constants of the second AAZTA unit. On the other hand, because of the high stability of the Cu**L** and Cu_2**L** complexes, the $\log K_{CuL}$ and $\log K_{Cu2L}$ values could not be calculated from the pH-potentiometric data (the complex formation was completed at pH=2.0). However, the lower limit of the $\log K_{CuL}$ and $\log K_{Cu2L}$ values could be evaluated by the simultaneous fitting of the V_{mL} – pH data pairs obtained at 1:1 and 2:1 metal-to-ligand concentration ratios. The estimated stability constants of Cu**L** and Cu_2**L** are: $\log K_{CuL} \sim \log K_{Cu2L} > 21$. The protonation constants of the Cu**L** and Cu_2**L** complexes calculated from the pH-potentiometric titration curves are in line with expected values for similar systems. The protonation constants of the mononuclear Gd**L** and Cu**L** complexes and the $\log K_2^H$, $\log K_4^H$, $\log K_6^H$ and $\log K_8^H$ values of the free **L** ligand are similar confirming the formation of the mononuclear complexes and a free AAZTA unit in the systems of 1:1 metal-to-ligand concentration ratio. However, the pH-potentiometric method is not

able to discriminate if the 1:1 complex formation between **L** and Gd^{3+} or Cu^{2+} ions takes place via the mononuclear Gd**L** and Cu**L** complexes with one free AAZTA unit or via the dimeric Gd_2**L** and Cu_2**L** complexes leaving half equivalents of **L** free.

2.3 Kinetic study

In collaboration with the Department of Inorganic and Analytical Chemistry of the University of Debrecen, a kinetic study of Gd_2**L** was also performed following the transmetallation reaction of the Gd^{3+} complex in presence of Cu^{2+}.

To avoid the typical precipitation that occurs to this system when in presence of free Gd^{3+}, the transmetallation reactions of the Gd_2**L** complex with Cu^{2+} were studied in a citrate (Cit) solution. Citrate is contained in human serum and is expected to coordinate any Gd^{3+} ion released from the CA giving Gd^{3+}-citrate complexes. The transmetallation/exchange reactions studied can be described by the Equations (1) and (2):

$$Gd_2L + 2Cu(Cit)H_{-1} \rightleftharpoons 2Gd(Cit) + Cu_2L + 2OH^- \quad (1)$$

$$Gd_2L + 2Cu(Cit)H_{-1} \rightleftharpoons 2Gd(Cit)H_{-1} + Cu_2L \quad (2)$$

The stability constants of the $Cu(AAZTA)^{2-}$ and $(Cu_2\mathbf{L})^{4-}$ complexes are significantly higher than those of the Gd(AAZTA) and Gd_2**L**, so the reactions (1 and 2) take place quantitatively.

The rates of the reactions (1 and 2) were studied by spectrophotometry (Figure 2.2) by recording the absorption spectra for the reactions between Gd_2**L** and $Cu(Cit)H_{-1}$ as a function of time. The spectra of $Cu(Cit)H_{-1}$ and Cu_2**L** differ considerably in the wavelength range 270 – 320 nm and so the progress of the reactions (1 and 2) was monitored at 290 nm with a Cary 1E spectrophotometer at 25°C.

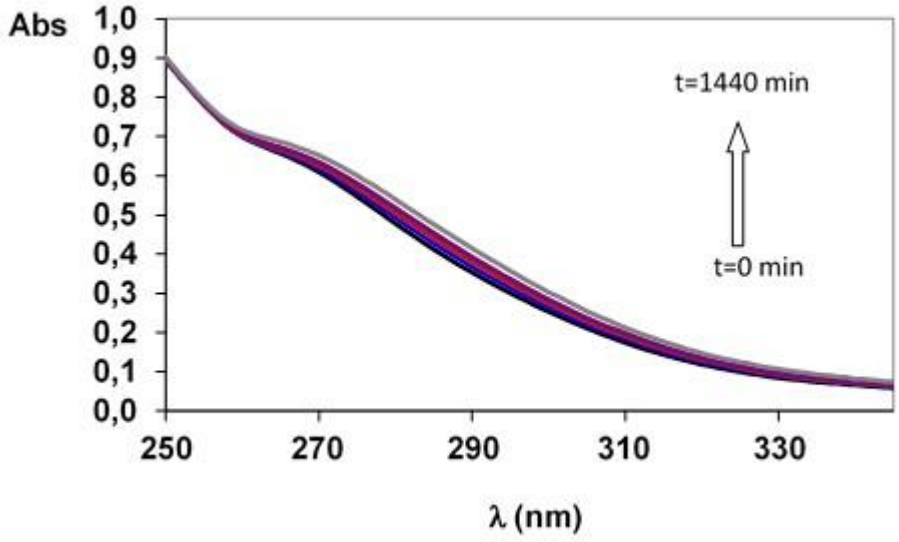

Figure 2.2. The absorption spectra of the Gd_2L – Cu(Citrate) reacting system ([Gd_2L^1]=2.0×10^{-4} M, [$Cu(Cit)H_{-1}$]=0.01 M, pH=5.5, l=0.1 cm, 0.1 M KCl, 25°C)

The absorbance values vs time trace of Gd_2**L** / $Cu(Cit)H_{-1}$ reacting system (Figure 2.3) can be fitted with the mono-exponential equation ($A_t=A_e + (A_0 - A_e) \times e^{-kd\times t}$, where k_d, A_0, A_e and A_t are the pseudo-first-order rate constant, the absorbance values at the start, at equilibrium and at the time t of the reaction, respectively), which indicates that the exchange reactions of both Gd(AAZTA) units of Gd_2**L** with $Cu(Cit)H_{-1}$ are similar.

The rates of the exchange reactions between the complexes Gd_2**L** and Cu^{2+}-citrate were studied in the pH range 5.5–7.5 and the k_d values could be obtained by fitting the data reported in Figure 2.4 and 2.5.

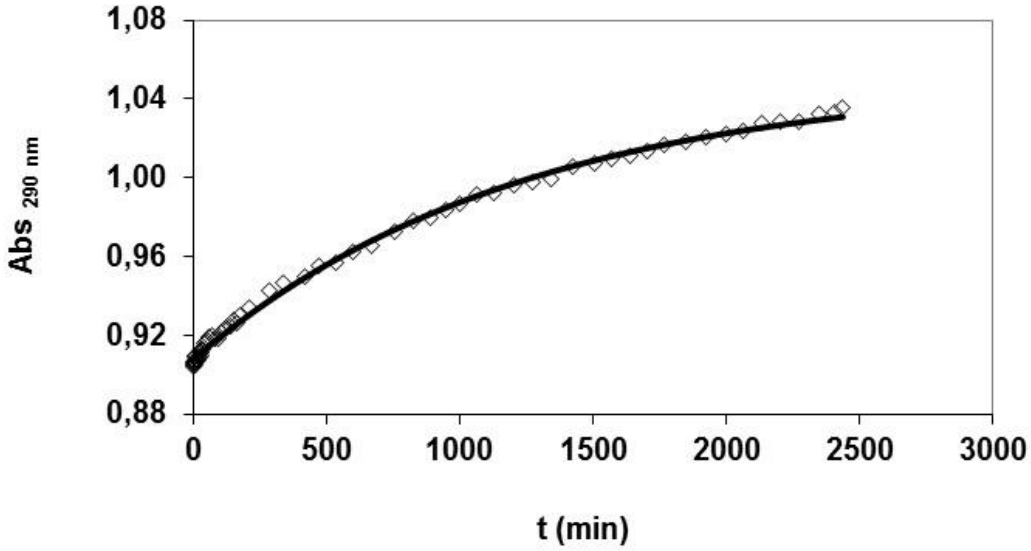

Figure 2.3. Absorbance values of the Gd_2L / $Cu(Cit)H_{-1}$ reaction system at 290 nm ([Gd_2L]=2×10^{-4} M, [Cu(Cit)]= 1.0×10^{-3} M, [MES]=0.01 M, pH=5.55, 0.1 M KCl, l=0.2 cm, 25°C).

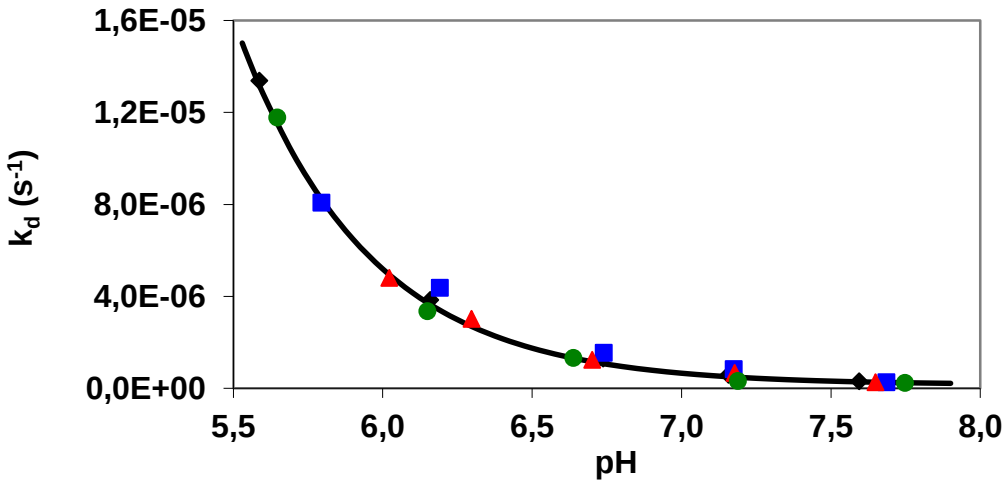

Figure 2.4. Rate constants (k_d) for the transmetallation reactions between Gd_2L and $Cu(Cit)H_{-1}$ ([Gd_2L]=2×10^{-4} M, [$Cu(Cit)H_{-1}$]=4×10^{-3} M (♦), 6×10^{-3} M (■), 8×10^{-3} M (▲) and 1×10^{-2} M (●), 0.1 M KCl, 25°C).

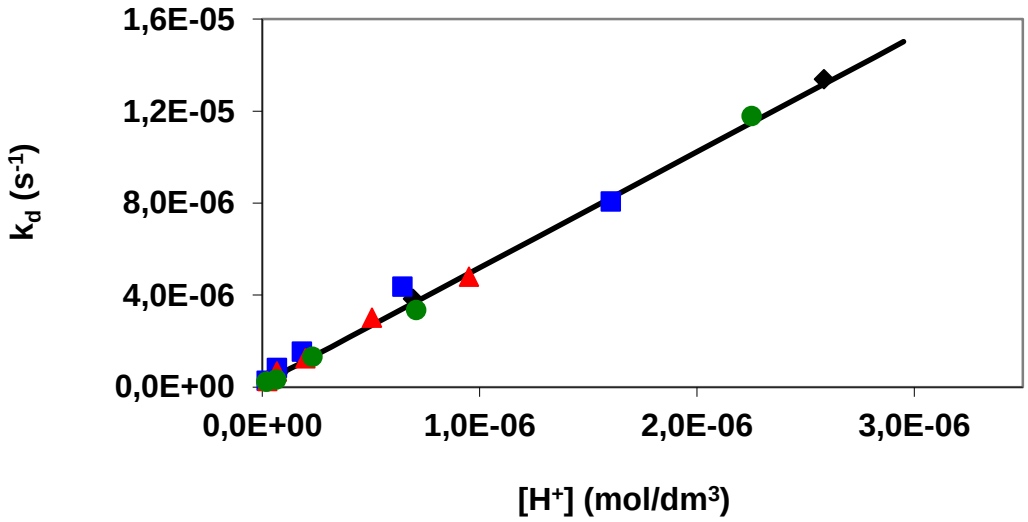

Figure 2.5. Rate constants (k_d) for the transmetallation reactions between Gd_2L and Cu(Cit)H_{-1}. ([Gd_2 L]=2×10^{-4} M, [Cu(Cit)H_{-1}]=4×10^{-3} M (♦), 6×10^{-3} M (■), 8×10^{-3} M (▲) and 1×10^{-2} M (●), 0.1 M KCl, 25°C).

The kinetic data presented in Figures 2.4 and 2.5 indicate that the rates of the exchange reactions are not [Cu(Cit)H_{-1}] dependent and increase linearly with the increase of the H^+ concentration. These findings show that under such conditions the reactions occur through the dissociation of complexes. The rate determining step is probably the spontaneous and proton assisted dissociation of the Gd_2**L** complex which is followed by the fast reaction between the free **L** ligand and Cu^{2+} with the formation of Cu_2**L**. So, the rate of the exchange reactions is directly proportional to the concentration of the Gd^{3+} complex and can be expressed by Equation (3):

$$-\frac{d[GdL]_t}{dt} = k_d[GdL]_t \qquad (3)$$

where $[GdL]_t$ and k_d are the total concentration of the Gd^{3+} complex and the pseudo-first-order rate constant, respectively.

The k_d values presented in Figure 2.5 can be given as follows:

$$k_d = k_0 + k_1[H^+] \quad (4)$$

where k_0 and k_1 are the rate constants characterizing the spontaneous and proton assisted dissociation, respectively. The k_0 and k_1 values were calculated from the k_d data presented in Figure 2.5, but only k_1 value is reported in Table 2.3, because a significant evaluation of k_0 was not possible. Unlikely, **Gd_2L** shows a lower kinetic intertness, if compare with the monomeric GdAAZTA or the q = 1 complex GdDTPA. Anyway its stability is higher than amidic systems as Gd(DTPA-BMA) is.

	Gd_2L	**Gd(AAZTA)[a]**	**Gd(DTPA)[b]**	**Gd(DTPA-BMA)[c]**
k_1 ($M^{-1}s^{-1}$)	5.03 ± 0.03	1.12	0.58	12.7

2.4 ^{1}H relaxometric properties

The ^{1}H NMR relaxometric characterization of Gd_2**L** was also carried out in order to obtain the relaxometric parameters and to confirm the good performance expected for such a probe.

The obtained data confirms, first of all, a good outcome in terms of r_{1p} of the dimeric complex, with a value of 14.1 mM^{-1} s^{-1}, consistent with values reported in literature for similar dimeric complexes[diaazta tei].

In Figure 2.6 the relaxometric titration of **L** with $GdCl_3$ is reported. The slope of the obtained line is 14.6, very close with the r_{1p} value confirmed through magnetic susceptibility measurement of 14.1 mM^{-1} s^{-1}.

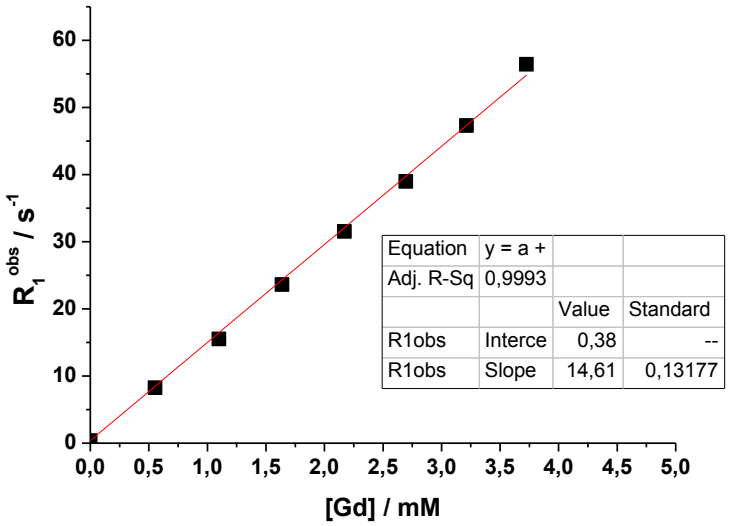

Figure 2.6. Complexometric titration of L with $GdCl_3$, followed by ^1H relaxometric measurements at 298 K and 20 MHz.

To get more insight, the1 H nuclear magnetic relaxation dispersion (NMRD) profiles of Gd_2**L** were recorded in aqueous solution at pH 7 and at 298 K (Figure 2.7).

The relaxivity per gadolinium atom is comparable to or even higher than that of other Gd^{3+} dimers [25–27], and is almost unchanged over a large range of magnetic fields, as expected, thus being interesting for applications in high-field MRI studies.

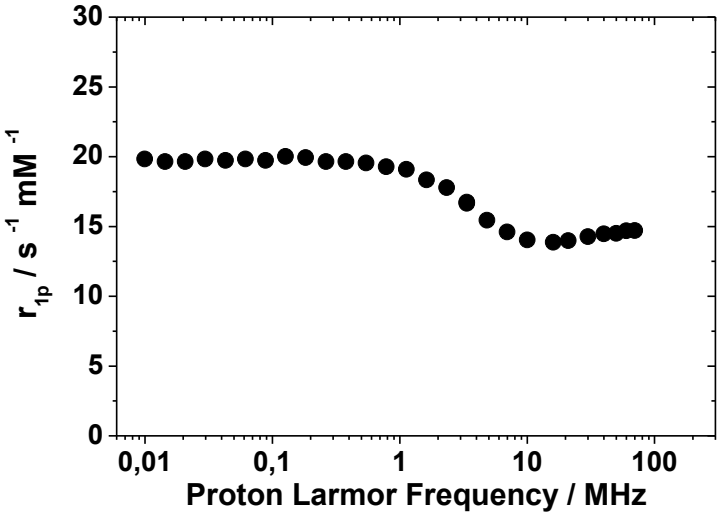

Figure 2.7. ^1H NMRD profile of Gd_2L, at pH 7, 298 K and [Gd]=1.07 mM.

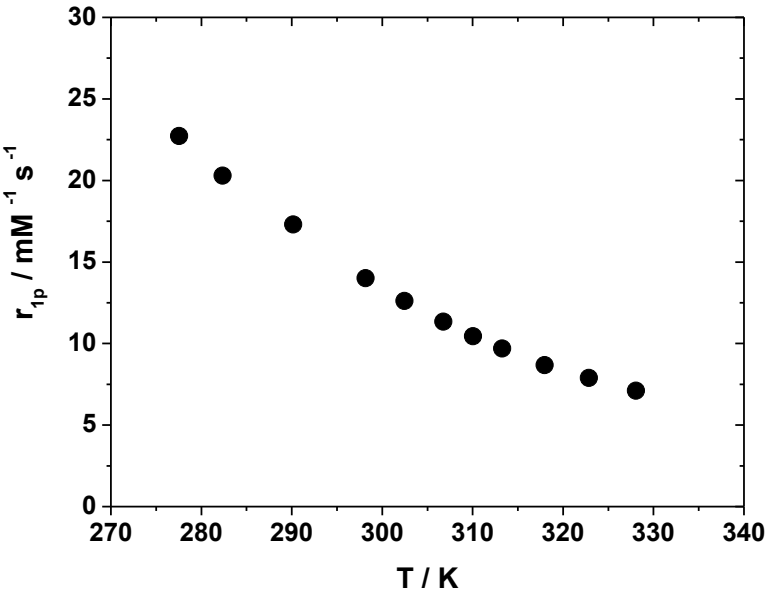

Figure 2.8. r_{1p} as a temperature function, measured at pH 7, 20 MHz and [Gd]= 3.9 mM.

The AAZTA cage is characterized by a fast water exchange rate- regime[ref]. In order to confirm that this feature is maintained also in the dimeric Gd_2**L** system a temperature-dependence measurement of r_{1p} was performed.

As reported in Figure 2.8, the r_{1p} behave as a lorentzian function of temperature, as usual for fast water exchange regime systems.

2.5 Conclusions

The dimeric AAZTA-like complex Gd_2**L** was synthesized and purified in good yelds. The thermodynamic and kinetic properties of the paramagnetic complex were investigated in order to determine if the complex has enough stability and kinetic inertness to allow a safe *in vivo* administration.

A ^{1}H relaxometric investigation was also performed, showing how Gd_2**L** seems to be a promising starting point for the development of high-relaxivity systems. His dimeric

and quite-rigid structure results in a good outcome in terms of r_{1p} (14.07 mM^{-1} s^{-1} at 25°C and 20 MHz), maintained also at higher magnetic fields.

Eventually, the nitro-group on **L** aromatic ring allows an easy functionalization of the ligand, in order to achieve any structural feature required for a wide range of covalent and non-covalent interactions, as reported in the following chapters of this thesis.

2.6 Experimental part

1-Nitro-3,5-benzenedicarbonyldiazide.

A solution of 1-nitroisophthaloyl dichloride (2.890 g; 11.7 mmol) in dry CH_2Cl (20 mL) was added drop wise in 2 min to an ice-bath cooled mixture of NaN_3 (7.6 g; 117 mmol) in and CH_2Cl_2 (30 mL), under vigorous magnetic stirring. The ice-bath was removed after 5 min and the mixture was stirred for overnight at room temperature. The mixture was washed with water (3 x 20 mL); then, the organic phase was collected, dried over $NaSO_4$, filtered and evaporated to yield a white solid (2.615 g, 85%).

^{1}H-NMR: ($CDCl_3$) 400 MHz δ = 9.0 (d, 2H, J = 1.8 Hz), 8.9 (t, 1H, J =1.8 Hz). ^{13}C-NMR: ($CDCl_3$) 100 MHz δ = 169.7 (CO), 148.8 (C), 135.1 (CH), 133.3 (2C), 128.8 (2CH).

II

1-Nitro-3,5-benzenedicarbonyldiazide (303 mg; 1.15 mmol) was heated to reflux for 3 h in dry toluene, under N_2. After cooling to room temperature, a solution of AAZTA-OH (1.385 g; 2.30 mmol) in dry CH_2Cl_2 (3 mL) was added under N_2 atmosphere. The reaction mixture was stirred overnight at rt, and then evaporated in vacuo. The crude product was purified on a silica gel chromatography column (petroleum ether/ethyl acetate 70/30) yielding pure **II** as a pale yellow solid (1.478 g, 91%).

TLC (silica gel 60 F254, petroleum ether/EtOAc 8 : 2, detection: UV 254 nm): Rf 0.35. ^{1}H-NMR ($CDCl_3$) 500 MHz δ = 8.03 (s, 2H, CH), 7.93 (bs, 2H, NH), 7.79 (s, 1H, CH), 4.23 (s, 4H, CH_2OCO), 3.68 (s, 8H, CH_2CO), 3.25 (s, 4H, CH_2CO), 3.24 (s, 4H, CH_2CO), 3.08 (d, 4H, J = 14.3 Hz, CH_2C), 2.78 (d, 4H, J = 14.3 Hz, CH_2C), 2.80–2.63 (m, 8H, CH_2CH_2), 1.42 (s, 36H, CH3), 1.41 (s, 36H, CH_3). 13C-NMR ($CDCl_3$) 125 MHz δ = 172.8, 170.7 (CO), 153.2 (NHCOO), 149.3 (C), 140.0 (2C), 113.0 (CH), 107.6 (2CH), 81.0, 80.8 (CCH_3), 68.1 (CH_2OCO), 63.3 (C), 62.3, 62.1 (CH_2CO), 59.0, 51.7 (CH_2cyclo), 28.3, 28.2 (CH_3). ESI-MS (m/z): 1408.78 (M + H+); calc for $C_{68}H_{114}N_9O_{22}$: 1408.81.

L

TFA (3 mL) was added dropwise to a solution of II (350 mg, 0.248 mmol) in CH_2Cl_2 (3 mL). The mixture was stirred at room temperature overnight and then evaporated in vacuo. The solid residue was washed twice with Et_2O (10 mL) and isolated by centrifugation. Then it was dried in vacuo, resulting in **L** as its trifluoroacetate salt.

References

1) S. Aime, L. Calabi, C. Cavallotti, E. Gianolio, G. B. Giovenzana, P. Losi, A. Maiocchi, G. Palmisano, M. Sisti, *Inorg. Chem.*, **2004**, *43*, 7588 – 7590.

2) Zs. Baranyai, F. Uggeri, G. B. Giovenzana, A. Bényei, E. Brücher, S. Aime; *Chem. Eur. J.*, **2009**, *15*, 1696-1705.

3) Zs. Baranyai, F. Uggeri, A. Maiocchi, G. B. Giovenzana, C. Cavallotti, A. Takács, I. Tóth, I. Bányai, A. Bényei, E. Brucher, S. Aime , *Eur. J. Inorg. Chem.*, **2013,** 147 – 162.

4) G. Gugliotta, M. Botta, L. Tei, *Org. Biomol. Chem.* **2010**, *8*, 4569-4574.

3. AAZTA-dimer functionalization with an adamantyl moiety and formation of supramolecular inclusion compounds

As detailed in the introduction chapter, according to the established theory of paramagnetic relaxation, large longitudinal relaxivity (r_1) enhancements can be mainly pursued by:

(1) increasing the hydration number (q),

(2) optimizing the mean residence lifetime (τ_M) of the coordinated water molecule(s),

(3) lengthening the rotational molecular correlation time (τ_R) [1–3].

It was recognized very early that the rotational dynamics is the main factor controlling the efficiency of the low molecular weight Gd^{3+} chelates. The reversible formation of adducts with human serum albumin (HSA) has been one of the major routes to achieve high relaxation enhancement for Gd^{3+} complexes as a result of the reduced rotational tumbling rate ($1/\tau_R$) of the macromolecular adduct [4, 5].

Slow-tumbling systems with large τ_R can be obtained through different approaches:

(i) contrast agents covalently bound to dendrimers, polymers, proteins, or virus capsids [1, 6–9];

(ii) aggregated systems, such as micelles or liposomes [1, 10–12];

(iii) suitably functionalized probes that can interact noncovalently with proteins or other types of macromolecules [1, 4, 5].

The large array of molecular recognition pathways provided by supramolecular chemistry allows one to exploit several systems for attaining large aggregates with high binding constants. For example, HSA has been largely used for the formation of adducts with Gd^{3+} chelates bearing hydrophobic functionalities, taking advantage not

only of the relaxivity enhancement generated by the noncovalent interaction, but also of the lengthening of the lifetime of the contrast agent in the bloodstream [1, 4, 5, 13, 14]. The latter issue plays a relevant role in the development of magnetic resonance angiography probes.

In the case of Gd^{3+} -based contrast agents, a well established and attractive approach to attain large τ_R values relies on the reversible formation of adducts between suitably functionalized complexes and macromolecular substrates [4, 5]. An optimized Gd^{3+} probe bearing a hydrophobic moiety, able to form supramolecular adducts with a given substrate, would be a promising system to achieve high relaxivities. For this purpose we chose GdAAZTA [15, 16] as a complex that combines high thermodynamic and kinetic stabilities with the presence of two water molecules in the inner coordination sphere (q = 2) in fast exchange with the bulk (see Chapter 2). Moreover, the use of the recently reported [17] dimeric bifunctional chelating agent bearing two AAZTA units and an isothiocyanate group for conjugation allows further optimization owing to the higher relaxivity (per Gd atom) of the dimeric complex with respect to the monomer as a consequence of its higher molecular weight, which translates into slower rotational dynamics.

A host–guest type of interaction widely explored to obtain large supramolecular structures involves cyclodextrins (CDs) and poly(β-CD)s (poly- β-CDs). CDs are naturally occurring, water-soluble, toroidally shaped oligosaccharides with a truncated cone-shaped hydrophobic cavity that can host a variety of organic compounds, especially those carrying a lipophilic group. Gd^{3+} complexes bearing hydrophobic substituents such as adamantyl, cyclohexyl, or phenyl moieties in their structure have been shown to be able to form inclusion adducts with β-CD (β-CD is a CD made up of seven sugar units) with high binding constants and remarkable relaxivity enhancement[18–21].

The ditopic Gd^{3+} complex was specifically designed to form host–guest adducts with β-CDs and poly-β-CDs, as the adamantyl moiety is known to interact strongly with the β-CD cavity [22, 23]. To the best of our knowledge, only a few Gd^{3+} chelates bearing an adamantyl moiety have been reported[18,24]. A detailed relaxometric

characterization of the complex was performed in aqueous solution by investigating the ^{1}H relaxivity dependence on pH, temperature, and magnetic field strength. The noncovalent interaction with both β -CD and poly-β-CD was evaluated by using the proton relaxation enhancement (PRE) method, and a detailed relaxometric study on the resulting host–guest adducts was conducted. Furthermore, to assess the possible application of such a system as an MRI contrast agent, and thus its stability in the presence of endogenous competitive species, the interaction with HSA was also investigated. Moreover, an in vivo test on B16-tumorbearing mice was performed by acquiring magnetic resonance images at 1 T over a period of 24 h.

3.1 Synthetic procedure

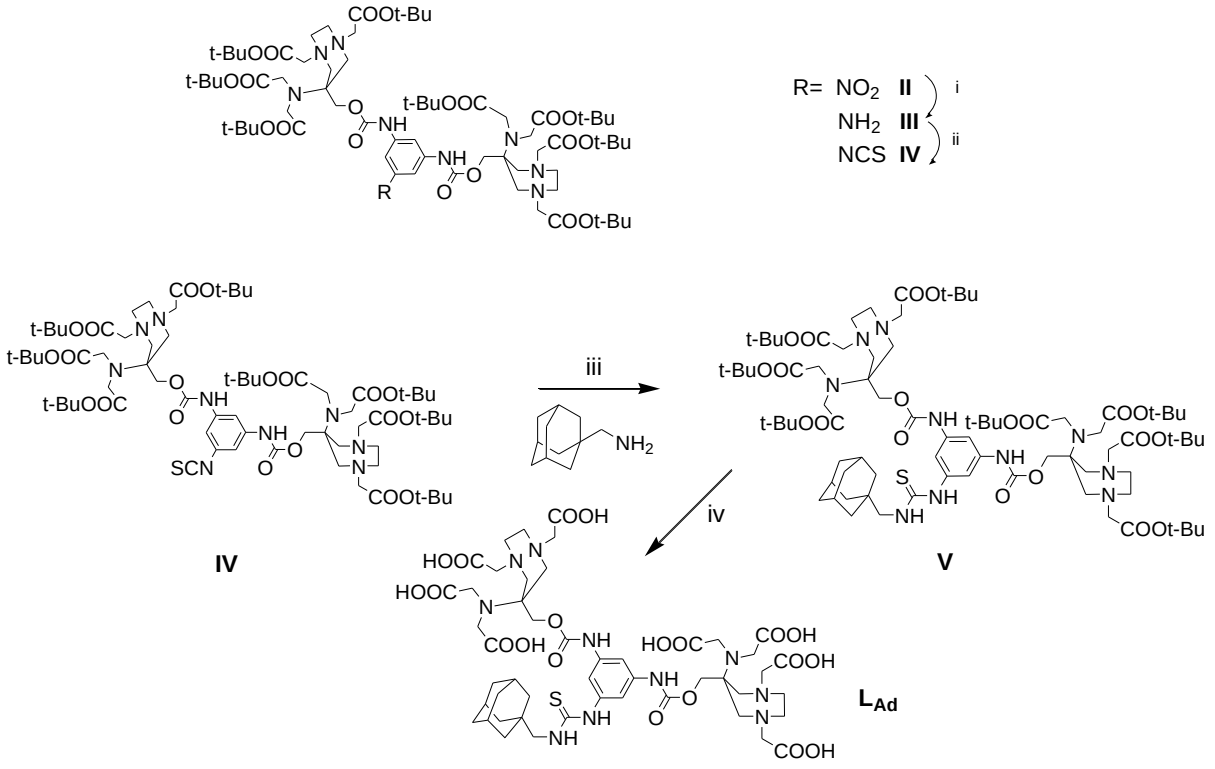

Scheme 3.1: Synthesis procedure to obtain L_{Ad}; i) H_2, Pd/C 10%, MeOH, rt; ii) Cl_2CS, CH_2Cl_2/NaOH 1 M, rt; iii) CH_2Cl_2, rt; iv) TFA, CH_2Cl_2, rt.

Starting from the AAZTA-like dimer **II**, described in the previous chapter, we used it as a bifunctional chelating agent for the development of larger assemblies [17]. The synthetic route towards the desired ditopic $Gd_2\mathbf{L_{Ad}}$ complex (Scheme 1) starts from the reduction of the nitro-group of **I** to amine (**II**), and then with the amine conversion into an isothiocyanate group using thiophosgene, obtaining **IV**. Finally, the reaction between **IV** and (1-adamantyl) methylamine in CH_2Cl_2 under mild basic conditions to afford **V**. The intermediate **V** was then deprotected by using a 1:1 mixture of trifluoroacetic acid (TFA) and CH_2Cl_2, yielding the final ligand $\mathbf{L_{Ad}}$. Both $\mathbf{L_{Ad}}$ and its protected form **V** were fully characterized by mass spectrometry and NMR spectroscopy. Although ditopic and/or multimeric Gd^{3+} complexes are widely investigated [25–27], not many of them are functionalized with a reactive or a target-specific moiety [17, 28–32]. For example, we have recently reported a series of ditopic Gd^{3+} complexes bearing hydrophobic moieties or a functional group obtained through a Ugi four-component reaction, including a study of the interaction between the octadecyl derivative and HSA [32]. However, in that case, the use of the less efficient GdDOTA-monoamide complexes led to results hampered by the presence of only one coordinated water molecule in slow exchange with the bulk.

3.2 ^{1}H relaxometric study

The Gd^{3+} complex was prepared by adding small volumes of a stock solution of $Gd(NO_3)_3$ to a solution of $\mathbf{L_{Ad}}$ while maintaining the pH at 6–7 with dilute NaOH. The complexation process was monitored by measuring the change in the longitudinal water proton relaxation rate (R_1) as a function of the amount of Gd^{3+} added. The slope of the straight line obtained corresponds to the relaxivity (r_1) of the complex, i.e., the R_1 enhancement per millimolar concentration of paramagnetic metal at a given temperature and magnetic field strength (typically 298 K/310 K and 20 MHz). The r_1 value of the ditopic complex at 20 MHz and 298 K was found to be 16.7 mM^{-1} s^{-1} (per

Gd atom), over two times greater than that of the corresponding monomeric GdAAZTA complex [15, 16]. This corresponds to an enhancement of 135 %, which can be largely attributed to the increase in molecular size, which translates into a corresponding increase of τ_R. In fact, the short linkers connecting the two metal chelates and the adamantly moiety to the central aromatic group are expected to minimize the flexibility of the system and favor long rotational correlation times in both the free form and the bound form.

To get more insight, the ^{1}H nuclear magnetic relaxation dispersion (NMRD) profiles of Gd_2L_{Ad} were recorded in aqueous solution at pH 7 and at 283, 298, and 310 K (Fig. 1, left). The relaxivity per gadolinium atom is comparable to or even higher than that of other Gd^{3+} dimers [25–27], and is almost unchanged over a large range of magnetic fields ($r_{40\ MHz}$ = 17.6 mM^{-1} s^{-1} ; r_{70MHz} 17.4 mM^{-1} s^{-1}), thus being interesting for applications in high-field MRI studies.

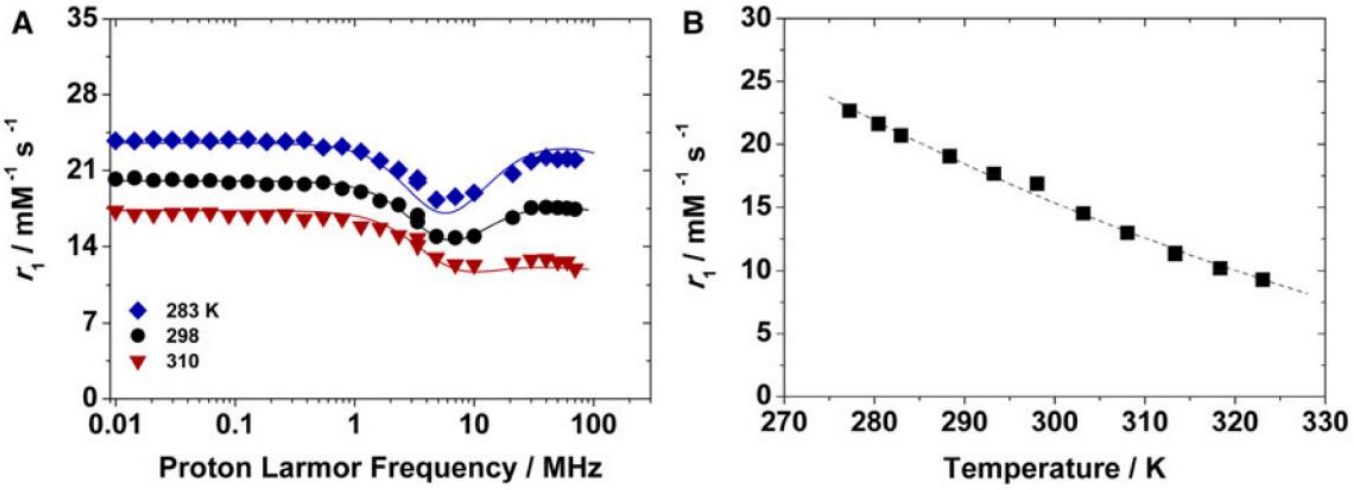

Figure 3.1: left) ^{1}H nuclear magnetic relaxation dispersion (NMRD) profiles of Gd_2L_{Ad} (see Scheme 3.1 for the structure) at 283, 298, and 310 K; right) r_1 as a function of temperature for Gd_2L_{Ad} (20 MHz, pH 7). The dashed line represents a simple fit to a monoexponential function to confirm the fast-exchange conditions.

Moreover, the r_1 value (20 MHz, 298 K) remains constant over a large pH range (4–11; Figure 3.2), indicating its stability towards acid-catalyzed and base-catalyzed dissociation.

The experimental data were then analyzed by fitting the data to the established theory for paramagnetic relaxation, using the well-known Solomon–Bloembergen–Morgan (SBM) equations and Freed's model for innersphere and outer-sphere contributions to the proton relaxivity, respectively [2, 3].

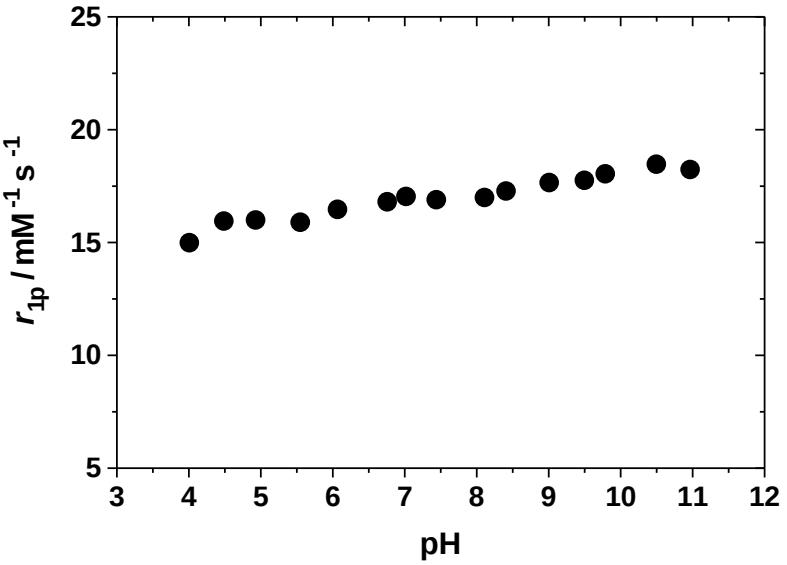

Figure 3.2: Dependence of the relaxivity of Gd_2L_{Ad} on pH (20 MHz; [Gd_2L_{Ad}] = 0.105 mM).

There are several parameters that enter in the description of the magnetic field dependence of r_1, but some of these can be set at standard values. The number of coordinated water molecules (q) was fixed to two, the distance of closest approach of the outer-sphere water molecules to Gd^{3+} was set to 4.0 Å a typical value for small metal chelates, and for the relative diffusion coefficient (D) the standard value of 2.24 x 10^{-5} cm^2 s^{-1} (298 K) was used. The Gd–water proton distance (r_{Gd-H}) and τ_R are parameters that are strongly correlated, and then the former is generally fixed. According to a pulsed electron–nuclear double resonance study by Caravan et al. [33],

the r_{Gd-H} values for selected DTPA- and DOTA-like Gd^{3+} complexes fall in the range 3.0–3.2 Å. The best results were obtained by fixing r_{Gd-H} at 3.0 Å.

As a function of temperature, r_1 follows an exponential dependence, as typical for gadolinium-based systems under a fast-water exchange regime (Fig. 1, right). We then used for the exchange lifetime the same value reported for $[Gd(AAZTA)(H2O)2]^-$, i.e., 298 sM = 90 ns [15, 16]. Nevertheless, the relaxivity is not affected by this parameter, and the result of the fit does not change for values of sM in the range 50–150 ns. We then used as adjustable parameters Δ^2 , sV, and sR. The electronic relaxation parameters, Δ^2 and sV, are rather similar to those of the monomer, indicating that the typical coordination cage of AAZTA is retained in the ditopic complex. The rotational correlation time is of the order of 220 ps (at 298 K), about three times longer. Although the fit can be considered rather satisfactory, it is not of very high quality, especially for the data at 283 K.

Much better results are obtained using the Lipari–Szabo approach for the description of the rotational dynamics. This model allows one to take into account the presence of a certain degree of internal rotation superimposed on the overall tumbling motion [34, 35]. These two types of motion, a relatively fast local rotation of the coordination cage about the linker to the central aromatic scaffold superimposed on the global reorientation of the complex, are characterized by different correlation times: τ_{RL} and τ_{RG}, respectively. The degree of correlation between global and local rotations is given by the parameter S^2 , which takes values between 0 (completely independent motions) and 1 (entirely correlated motions). A five-parameter (Δ^2, τ_V, τ_{RL}, τ_{RG}, and S^2) least-squares fit of the data was performed. The best-fit parameters for $Gd_2\mathbf{L_{Ad}}$ are listed in Table 1 and are compared with those for the parent complex $[Gd(AAZTA)(H_2O)_2]^-$. The correlation times for the local and global rotations differ by only a factor of 3, hence confirming the low level of rotational flexibility of theditopic complex. This is also evidenced by the large value of the order parameter S^2 .

3.2.1 Supramolecular adducts with β-CD and poly-β-CD

As mentioned already, an alternative route for increasing the relaxivity consists in the formation of host–guest noncovalent interactions between suitably functionalized complexes and slowly tumbling substrates. A major advantage is that the structural integrity of the complex is preserved, and then the unbound form can be easily separated from the free from. In addition, the association constant can be modulated as it depends on the physicochemical properties of the targeting group. The relaxivity of the supramolecular structure depends on several properties of the paramagnetic guest: the number of bound water molecules (q), their rate of exchange with the bulk, and the degree of rotational mobility of the complex in the bound form, which is also correlated with the compactness and stereochemical rigidity of the free complex. Finally, also the nature of the pendant group dictates the strength of the interaction.

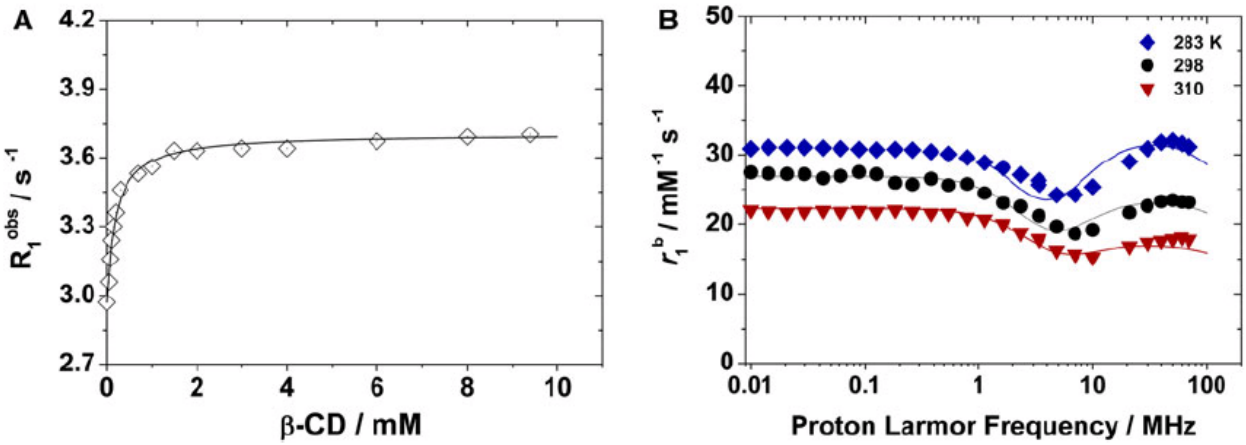

Figure 3.3. Left: Water proton relaxation rate of a 0.08 mM aqueous solution of Gd_2L_{Ad} as a function of increasing amounts of b-cyclodextrin (β-CD) (20 MHz, 298 K). Right: ^{1}H NMRD profiles of Gd_2L_{Ad}-β-CD at 283, 298, and 310 K.

The presence of an adamantyl moiety in the ditopic $Gd_2\mathbf{L_{Ad}}$ complex allows its strong interaction with the hydrophobic cavity of β-CDs: for such adducts, high affinity constants (K_A = 10^3–10^4 M^{-1}) have often been reported [13]. In the context of this work, the properties of the adducts between $Gd_2\mathbf{L_{Ad}}$ and either monomeric β-CD or high molecular weight poly-β-CD were investigated through the well-established ^{1}H PRE technique. This consists in measuring the variation in R_1 for increasing concentrations

of the host. With this method, the binding parameters K_A, n (the number of equivalent and independent binding sites), and r^b_1(the relaxivity of the resulting supramolecular adducts) can be assessed. To this end, a dilute solution of $Gd_2\mathbf{L_{Ad}}$ was titrated with β-CD, at 20 MHz and 298 K, and the least-squares fit of the R_1 versus β-CD concentration binding isotherm (Figure 3.3, left) enabled us to calculate the affinity constant [K_A = (1.05 ± 0.09) x 10^4 M^{-1}] and the relaxivity of the adduct (r^b_1 = 21.4 ± 0.1 mM^{-1} s^{-1}). The formation of the inclusion compound was then accompanied by an increase of r_1 of 29 % relative to the isolated complex, which reflects the slowing down of molecular tumbling. The analysis of the NMRD profiles indicates that both the local rotational correlation time and the global rotational correlation time (Table 1) are more than doubled as compared with the free dimer, whereas the S^2 value is sensibly reduced (from 0.66 to 0.23), suggesting great flexibility of the adamantly moiety in the β-CD cavity.

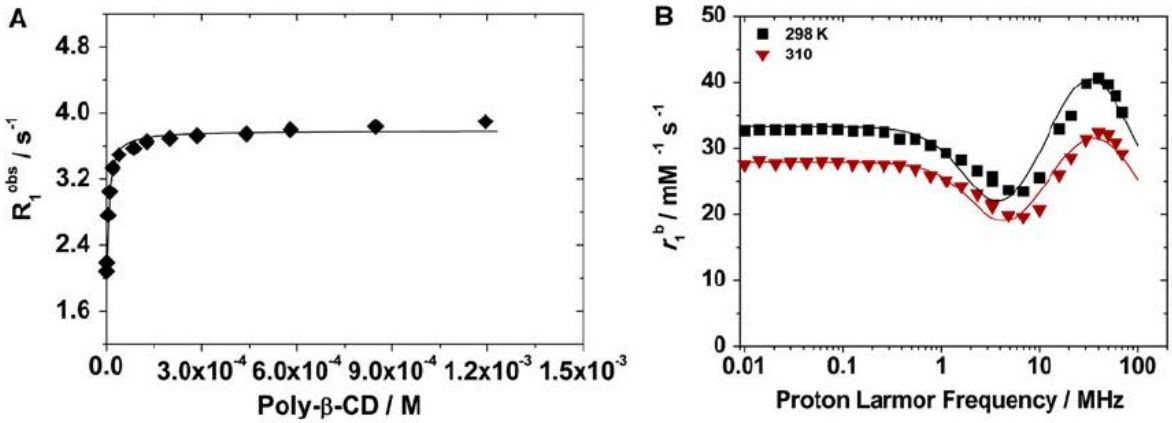

Figure 3.4: Left) Water proton relaxation rate of a 0.05 mM aqueous solution of Gd_2L_{Ad} as a function of increasing amounts of poly-β-CD (20 MHz, 298 K). Right) NMRD profiles of Gd_2L_{Ad}–poly-β-CD at 298 and 310 K.

An analogous binding interaction was exploited to form larger supramolecular assemblies using as the host a polymer of β-CD with a molecular mass of approximately 15 kDa. In this case up to 13 $Gd_2\mathbf{L_{Ad}}$ units can be loaded into the β-CD cavities to form a final system ($Gd_2\mathbf{L_{Ad}}$–poly- β-CD) with a molecular mass of about 34 kDa. Each of the 13 β-CD units of poly- β-CD can bind the adamantyl moiety of $Gd_2\mathbf{L_{Ad}}$. This linear polymer is characterized by nearly equivalent binding sites and,

as a consequence, will affect the rotational dynamics of each bound chelate approximately equivalently.

Consequently, the interaction of $Gd_2\mathbf{L_{Ad}}$ with poly-β-CD reproduces, to a first approximation, a simple 1:1 binding model (Figure 3.4). The data were fitted to a simple model that considers the presence of 13 equivalent and independent binding sites, yielding the values of the association constant [K_A = (1.27 ± 0.13) x 10^4 M^{-1}] and the relaxivity (r^b_1 = 33.9 ± 0.3 mM^{-1} s^{-1}) for the bound ditopic complex.

The relaxivity enhancement is then of the order of 100 % over the dimer and 61 % as compared with $Gd_2\mathbf{L_{Ad}}$–β-CD. It is worth stressing that the r^b_1 value represents an average value and not the absolute value of a well-identified ditopic chelate. The NMRD profiles were recorded at two temperatures under conditions ensuring that more than 98 % of the chelate was bound to the macromolecular substrate (Figure 3.4, right). Fitting the profiles to the SBM theory (including the Lipari–Szabo model) affords the parameters listed in Table 3.1.

The marked decrease in molecular tumbling is reflected in the formation of relaxivity peaks centered at about 40 MHz, distinctive of slowly rotating systems. However, an increase of the local degree of rotation of the discrete dimer at the binding site also occurs, which limits the relaxivity.

This is shown by the decrease of S^2 (from 0.29 for $Gd_2\mathbf{L_{Ad}}$–β-CD to 0.17 for $Gd_2\mathbf{L_{Ad}}$ – poly-β-CD) and by the larger difference between τ_{RG} (2.3 ns) and τ_{RL} (410 ps).

A comparison between the relaxivity values of the supramolecular adducts $Gd_2\mathbf{L_{Ad}}$–β-CD and $Gd_2\mathbf{L_{Ad}}$–poly-β-CD and those measured for related paramagnetic systems underlines the fact that the r^b_1 values reported here are the highest for chelates functionalized with a single hydrophobic group [18, 20]. On the other hand, Gd^{3+} complexes of DTPA, DOTA, or DO3A bearing three cyclohexyl or benzyloxy groups were found to form inclusion compounds with β-CD or poly-β-CD of even higher relaxivity [19]. This can be explained on the basis of an increased rigidity of the systems (greater τ_{RL}) due to multisite interactions that cannot occur in the case of the monoadamantyl-substituted bimetallic chelate.

3.2.2 Interaction with HSA

The presence of a hydrophobic pendant arm on the Gd^{3+} complex makes possible noncovalent interactions with hydrophobic binding sites on HSA. The noncovalent binding with plasma proteins is generally exploited to increase the lifetime of the paramagnetic probe in the vascular system, for angiographic MRI applications, and to expand the time window for imaging. The interaction is accompanied by a strong relaxivity enhancement associated with the reduced tumbling rate (lengthening of τ_R) of the adduct [1, 4, 5, 13]. Like for the case of β-CD, the binding parameters were determined according to the PRE method by measuring R_1 as a function of the concentration of added protein (Figure 3.5, left). Fitting of the experimental data was performed assuming the presence of one equivalent and independent binding site (*n* = 1), even though the presence of multiple affinity sites on HSA cannot be excluded.

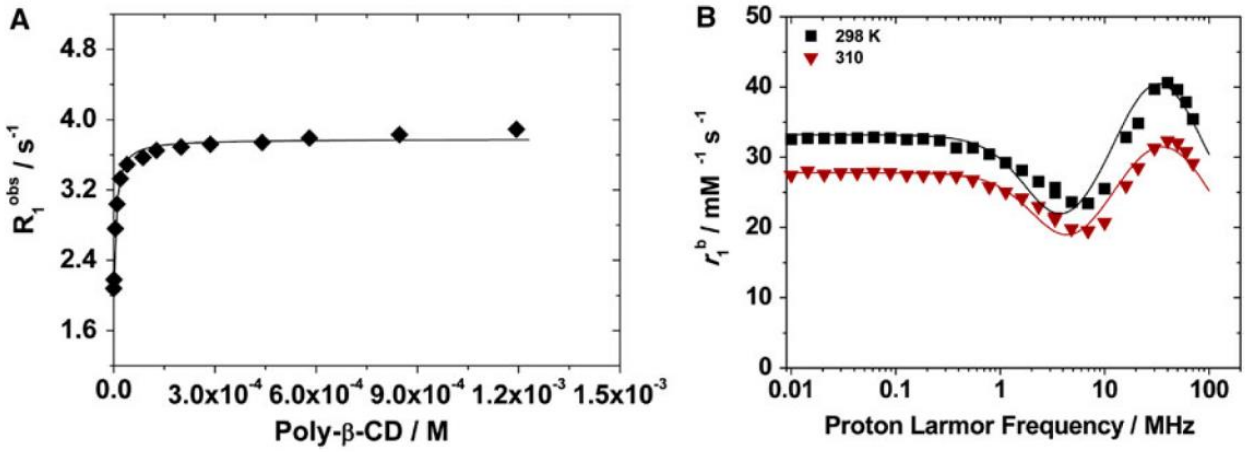

Figure 3.5: Left) Water proton relaxation rate of a 0.05 mM aqueous solution of Gd_2L_{Ad} as a function of increasing amounts of poly-β-CD (20 MHz, 298 K). Right: NMRD profiles of Gd_2L_{Ad}–poly-β-CD at 298 and 310 K.

In this way, we could estimate the value of the thermodynamic association constant, which was rather similar to that with β-CD [KA = (1.2 ± 0.8) x 104 M^{-1}], and the relaxivity of the resulting paramagnetic metalloprotein (r^b_1 = 41.4 ± 1.1 mM^{-1} s^{-1}). The NMRD profiles of the Gd_2**L**$_{Ad}$ –HSA adduct were measured at 298 and 310 K (Figure 3.5, right) for a 0.07 mM solution of Gd_2**L**$_{Ad}$ in the presence of 1.0 mM HSA. Under this condition, more than 99 % of the ditopic complex is bound to the protein. The data were analysed only in the high field region because of the known limitations of the SBM theory to completely account for the behavior of slowly rotating systems at low magnetic field strengths [13]. The r^b_1 value represents an additional increase of about 20 % compared with the relaxivity of Gd_2**L**$_{Ad}$–poly-β-CD and is comparable to that reported for the commercial blood pool contrast agent MS-325 (r^b_1 = 49 mM^{-1} s^{-1}) [36]. The best-fit parameters (Table 3.1) indicate that the relaxivity of the adduct is markedly limited by the poor correlation between global and local rotational motions. A more pronounced degree of immobilization by protein binding would make it possible to attain a further, large relaxivity enhancement. It is worth noting that even a nonoptimal rate of exchange could hamper the achievement of higher relaxivity; however, the decrease of r^b_1 with increasing temperature suggests that this parameter is not a dominant factor.

Paramter	Gd_2L_{Ad}	Gd_2L_{Ad}-β-CD	Gd_2L_{Ad}-poly-β-CD	Gd_2L_{Ad}-HSA	GdAAZTA[a]
$^{298}r_{1p}$ **(mM^{-1} s^{-1})[b]**	16.7	21.6	33.9	41.4	7.1
Δ^2 **(10^{19} s^{-2})**	2.5	1.2	1.3	1.4	2.2
$^{298}\tau_V$ **(ps)**	31	44	37	21	31
$^{298}k_{ex}$ **(10^6 s^{-1})**	11.1[c]	11.1[c]	11.1[c]	11.1[c]	11.1
$^{298}\tau_{RG}$ **(ns)**	0.29	0.62	2.3	28	0.074

$^{298}\tau_{RL}$ (ps)	107	227	410	479	-
S^2	0.66	0.29	0.17	0.10	-
q^c	2	2	2	2	2
r_{GdH} (Å)^c	3.0	3.0	3.0	3.0	3.1
a (Å)^c	4.0	4.0	4.0	4.0	4.0
^{298}D (10^{-5} cm^2 s^{-1})^c	2.24	2.24	2.24	2.24	2.24

Table 3.1: Best-fit parameters obtained by analysis of the ^{1}H nuclear magnetic relaxation dispersion profiles for Gd_2L_{Ad} (See scheme 3.1 for the structure) and his adducts with β-CD, poly-β-CD and human serum albumin (HSA); [a] From [6,7]; [b] at 20 MHz; [c] fixed in the fitting procedure.

3.3 *In vivo* MRI analysis

In vivo tumor, liver, and kidney accumulation of Gd_2L_{Ad} was investigated by Dr Eliana Gianolio and Francesca Arena through a 24-h acquisition of magnetic resonance images at 1 T of B16-tumor-bearing mice at the Department of Molecular Biotechnology and Health Sciences,Molecular Imaging Center, Università di Torino.

Control experiments were conducted by using the commercial nonspecific contrast agent ProHance© [gadolinium 10-(2-hydroxypropyl)-DO3A] at the same time intervals and concentration (Figure 3.5). We subcutaneously injected approximately 1 x 10^6 B16 murine melanoma cells into C57Bl/6 female mice (6–7 weeks old). Tumor growth was monitored, and the mice underwent MRI analysis 10–12 days after inoculation, when

the tumor dimensions were about a few hundred cubic millimeters. A strong signal enhancement in the tumor region was noted up to 50 min after the administration of Gd_2L_{Ad} (0.05 mmol/kg), which was not observed when ProHance© was administered.Moreover, the signal enhancement in the tumor appears to be significantly high (approximately 40 %) even 24 h after the administration of the probe. The enhanced tumor retention observed after the administration of Gd_2L_{Ad} is likely related to its high affinity towards serum albumin.

The binding with serum proteins allows prolonged retention of the paramagnetic probe in the vascular system and its gradual accumulation in the tumor region on the basis of the well-known enhanced permeability and retention effect [37]. Albumin-bound MRI contrast agents pass through the highly permeable blood vessels in tumor, but not in normal tissues, and do not diffuse back into blood capillaries or end up in the lymphatic system. In contrast, the neutral and nonspecific ProHance© complex, which is not able to bind to serum proteins, is rapidly eliminated from the vascular system and does not accumulate in the tumor region. The signal enhancements observed for liver and kidney suggest a preferential renal elimination of Gd_2L_{Ad}, as expected for low molecular weight gadolinium-based contrast agents.

The mean signal enhancement percentage in kidneys reaches a peak during the first 30 min, with a subsequent decrease after 6 and 24 h due to the renal elimination (see the electronic supplementary material).

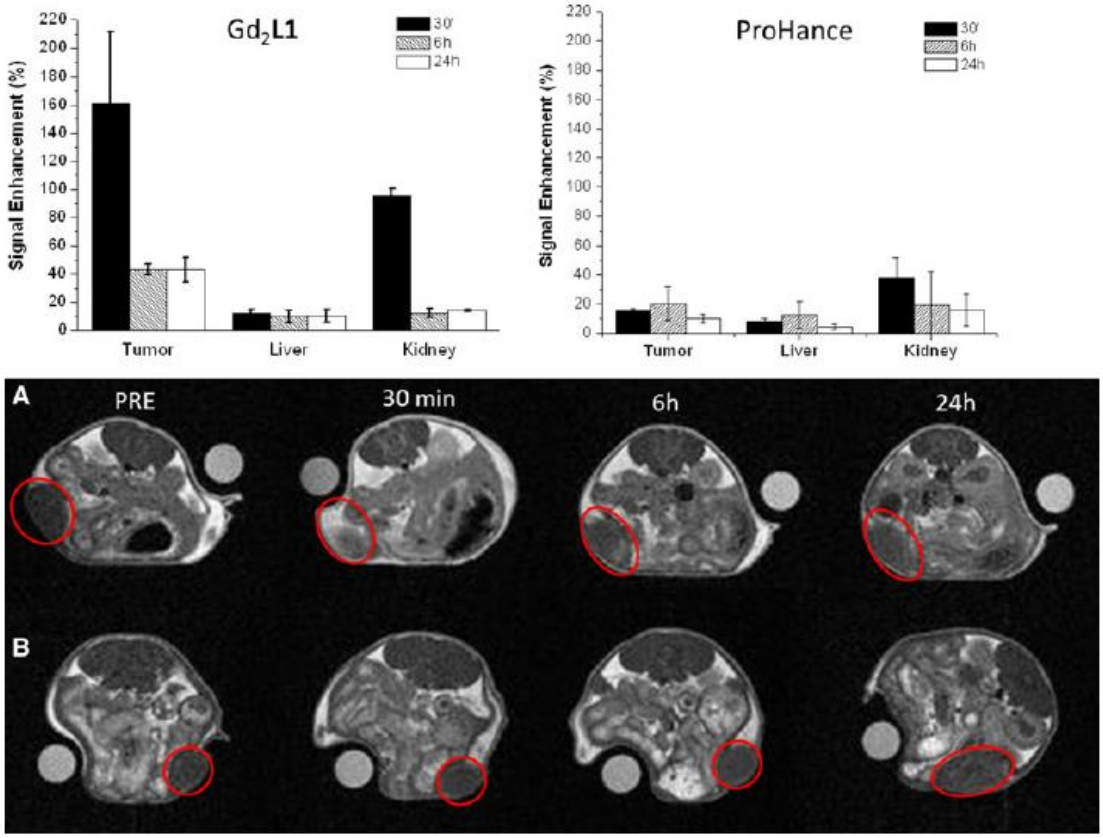

Figure 3.5: Top) Comparison of the signal enhancement in tumor, liver, and kidneys, calculated from the mean signal in the region of interest with respect to the precontrast images, after intravenous injection of 0.05 mmol/kg Gd_2L_{Ad} (top left) and ProHance (top right). Bottom) Axial T_1-weighted magnetic resonance images recorded at 1 T on a mouse before (proton relaxation enhancement, PRE) and after (30 min, 6 h, and 24 h) the administration of 0.05 mmol/kg Gd_2L_{Ad} (A) and ProHance (B). The tumor region is highlighted with a red circle.

Despite the lipophilic properties of Gd_2L_{Ad} and its quite strong interaction with serum albumin, a very low hepatic accumulation has been observed [38].

3.4 Conclusions

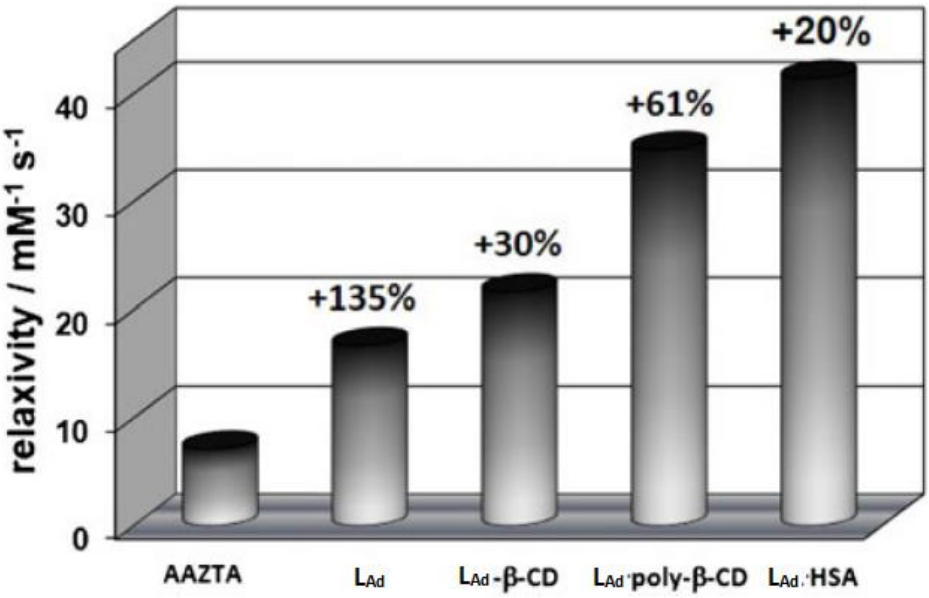

Figure 3.6: ^{1}H relaxivity values of GdAAZTA and Gd_2L_{Ad} and its supramolecular adducts with b-CD, poly-b-CD, and HSA (20 MHz, 298 K)

A novel ditopic Gd^{3+} complex bearing a hydrophobic adamantly moiety, based on two stable and q = 2 GdAAZTA-like complexes, has been synthesized and characterized. The ^{1}H relaxometric properties and the ability to form supramolecular adducts with CD, poly-β-CD, and HSA have been investigated in detail. Gd_2L_{Ad} has several excellent properties which make it a promising highly efficient MRI probe: (1) each Gd^{3+} ion possesses two inner-sphere water molecules characterized by a sufficiently fast rate of exchange; (2) it is stable over a wide pH range; (3) it has a good degree of compactness and limited rotational flexibility, which results in a τ_R value nearly ideal for MRI applications at high field strengths (1.5–3.0 T); (4) it is endowed with a strong ability to interact noncovalently with a number of substrates of increasing complexity ($K_A \sim 10^4$ M^{-1}), thus affording large relaxivity enhancements. The relaxivity values per gadolinium atom show a constant increase from Gd_2L_{Ad} to Gd_2L_{Ad}–HSA, corresponding to an enhancement of up to approximately 250 %, as illustrated in Figure 3.6. In conclusion, as the CD cavity may also host drug molecules, properly

functionalized targeting vectors, or optical dyes, the optimized Gd_2L_{Ad} complex has good potential to be used in CD-based probes in association with a vector or a dye for molecular imaging applications or in association with a drug for theranostic or pharmaceutical uses.

3.5 Experimental part

Synthesis of **III**

10% Pd/C (15 mg) suspended in water (1 mL) was added to a solution of **II** (150 mg; 0.106 mmol) in MeOH (10 mL). The mixture was stirred overnight under H_2 atmosphere and then filtered. The filtrate was evaporated in vacuo affording pure **III** (136 mg; 93%). TLC (silica gel 60 F254, petroleum ether/EtOAc 8 : 2, detection: UV 254 nm): Rf 0.05. ^{1}H-NMR ($CDCl_3$) 500 MHz d = 7.12 (bs, 2H, NH), 6.79 (bs, 1H, CH), 6.61 (bs, 2H, CH), 4.14 s, 4H, CH_2OCO), 3.66 (s, 8H, CH_2CO), 3.22 (s, 8H, CH_2CO), 3.04 (d, 4H, J = 14.3 Hz, CH_2C), 2.74 (d, 4H, J = 14.3 Hz, CH_2C), 2.87–2.61 (m, 8H, CH_2CH_2), 1.37 (s, 36H, CH_3), 1.36 (s, 36H, CH_3). ^{13}C-NMR ($CDCl_3$) 125 MHz d = 172.8, 170.6 (CO), 153.2 (NHCOO), 148.4 (C), 139.5 (2C), 100.1 (2CH), 98.7 (CH), 81.0, 80.8 (CCH3), 67.5 (CH_2OCO), 63.1 (C), 62.1–62.0 (CH_2CO), 58.7, 51.4 (CH_{2cycle}), 28.2, 28.1 (CH_3). ESI$^+$-MS (m/z): 1379.43 $[M + H]^+$; calc for $C_{68}H_{116}N_9O_{20}$: 1378.83.

Synthesis of **IV**

A solution of thiosphogene (10.5 µL; 0.138 mmol) in dry CH_2Cl_2 (2 mL) was added drop wise in 2 min to a ice-bath cooled mixture of **III** (98.5 mg; 0.106 mmol) in saturated $NaHCO_3$ (5 mL) and CH_2Cl_2 (5 mL), under vigorous magnetic stirring. The ice-bath was removed after 5 min and the suspension was stirred for 2 h at room temperature. The organic phase was separated and extracted with water (3 x 10 mL); then the organic phase was dried over Na_2SO_4, filtered and evaporated to yield a yellow solid. TLC (silica gel 60 F254, petroleum ether/EtOAc 8 : 2, detection: UV 254

nm): Rf 0.29. ^{1}H-NMR ($CDCl_3$) 500 MHz d = 7.41 (bs, 2H, CH), 7.20 (bs, 1H, CH), 7.15 (bs, 2H, NH), 4.21 (s, 4H, CH_2OCO), 3.69 (s, 8H, CH_2CO), 3.25 (s, 8H, CH_2CO), 3.09 (d, 4H, J = 14.3 Hz, CH_2C), 2.87 (d, 4H, J = 14.3 Hz, CH_2C), 2.70–2.64 (m, 8H, CH_2CH_2), 1.43 (s, 36H, CH_3), 1.42 (s, 36H, CH_3). ^{13}C-NMR ($CDCl_3$) 100 MHz d = 172.8, 170.4 (CO), 153.1 (NHCOO), 140.0 (C), 128.0 (C), 110.3 (CH), 106.7 (CH), 81.3, 81.0 (CCH_3), 67.5 (CH_2OCO), 63.2 (C), 62.3, 62.1 (CH_2CO), 59.0, 51.6 (CH_{2cycle}), 28.2, 28.0 (CH_3). ESI$^+$-MS (m/z): 1421.38 $[M + H]^+$; calc for $C_{69}H_{114}N_9O_{20}S$: 1420.79.

Synthesis of **V**

A solution of (1-adamantyl)methylamine (33 mg, 0.199 mmol) in dry CH_2Cl_2(2 mL) was added to a solution of **IV** (243 mg, 0.153 mmol) and Et_3N (97 µL, 0.701 mmol) in dry CH_2Cl_2 (10 mL) under an N_2 atmosphere. The mixture was stirred overnight at room temperature, and then it was evaporated in vacuo. The crude product was purified by column chromatography (SiO_2, 7:3 petroleum ether/EtOAc), yielding **V** as a yellow oil (124 mg, 0.109 mmol, 71 % yield). ^{1}H NMR (500 MHz, CD_3Cl): d 7.58 (br s, 2H, CH_{Ar}), 7.29 (s, 1H, CH_{Ar}), 7.17 (br s, 2H, NHCO), 6.47 (br s, 2H, NHCS), 4.22 (s, 4H, CH2O), 3.25 (s, 16H, CH2C=O), 3.10–2.64 (m, 16H, CH_2^{Cy}), 2.04–1.51 (m, 13H, CH_{Ad}), 2.02 (s, 2H, CH_2^{Ad}), 1.42 (br s, 72H, CH_3). ^{13}C NMR (125 MHz, $CDCl_3$): d 172.0, 170.8 ($COO_{t\text{-}Bu}$), 153.1 (NCO), 140.4 (C^{Ar}_q), 108.2 (CH_{Ar}), 105.9 (CH_{Ar}), 81.0, 80.9 (CCH_3), 67.9 (CH_2O), 63.3 (C^{Cy}_q), 62.3, 62.1 (CH_2CO), 59.0, 51.6 (CH_2^{Cy}), 41.9 (CH_2^{Ad}), 37.1, 34.1, 21.1, (C^{Ad}), 28.3, 28.2 (CH_3). ESI$^+$-MS: m/z 1,587 = $[M + H]^+$, 794 = $[M + 2H]^{2+}$ calc for $C_{80}H_{133}N_{10}O_{20}S$, 1,587.02).

Synthesis of L_{Ad}

TFA (3 mL) was added dropwise to a solution of **V** (124 mg, 0.0782 mmol) in CH_2Cl_2 (3 mL). The mixture was stirred at room temperature overnight and then evaporated in vacuo. The solid residue was washed twice with Et_2O (10 mL) and isolated by centrifugation. Then it was dried in vacuo, resulting in $\mathbf{L_{Ad}}$ as its trifluoroacetate salt. HPLC analysis: H_2O/0.1 % TFA (solvent A) and CH_3OH/0.1 % TFA (solvent B)

starting from 100 % solvent A for 5 min and then with a gradient to 100 % in 11 min at a flow rate of 1 mL min-1 over a total run of 20 min; retention time 15.9 min. ^{1}H NMR (500 MHz, D_2O) d 7.37 (br s, 2H, CH_{Ar}), 7.19 (br s, 1H, CH_{Ar}), 4.18 (s, 4H, CH_2O), 5.28 (s, 16H, $CH_2C{=}O$), 2.80–2.57 (m, 16H, cycle), 1.96 (s, 2H, CH_2^{Ad}), 1.93–1.51 (m, 13H,CH/CH_2^{MeAd}). ^{13}C NMR (125 MHz, D_2O): d 181.0 (CS), 180.5, 179.3 (COOH), 155.3 (NCO), 137.8, 120.1 (C_{Ar}), 118.2, 115.4 (CH_{Ar}), 66.2 (CH2O), 64.3 ($CH_2C{=}O$), 63.0 (C_q^{Cy}), 60.6, 56.6 (CH_2^{Cy}), 57.9 (CH_2^{Ad}), 39.9, 39.7, 36.6, 36.5, 28.1 (C_{Ad}). ESI$^+$-MS: m/z 1,138 $[M + H]^+$, 569 $[M + 2H]^{2+}$ (calc for $C_{48}H_{69}N_{10}O_{20}S$, 1,138.17).

References

1) Botta M, Tei L (2012) Eur J Inorg Chem 1945

2) Caravan P, Ellison JJ, McMurry TJ, Lauffer RB (1999) Chem Rev 99:2293

3) Aime S, Botta M, Terreno E (2005) Adv Inorg Chem 57:173

4) Aime S, Botta M, Fasano M, Terreno E (2001) In: Merbach AE,Tòth E (eds) The chemistry of contrast agents in medical magnetic resonance imaging. Wiley, Chichester, chap 5

5) Caravan P (2009) Acc Chem Res 42:851–862

6) Villaraza AJL, Bumb A, Brechbiel MW (2010) Chem Rev 110:2921–2959

7) Delli Castelli D, Gianolio E, Geninatti Crich S, Terreno E, Aime S (2008) Coord Chem Rev 252:2424–2443

8) Schladt TD, Schneider K, Schild H, Tremel W (2011) Dalton Trans 40:6315–6343

9) Khemtong C, Kessinger CW, Gao J (2009) Chem Commun 3497–3510

10) Mulder WJM, Strijkers GJ, Van Tilborg GAF, Cormode DP, Fayad ZA, Nicolay K (2009) Acc Chem Res 42:904–914

11) Accardo A, Tesauro D, Luigi A, Pedone C, Morelli G (2009) Coord Chem Rev 253:2193–2213

12) Terreno E, Delli Castelli D, Cabella C, Dastru ` W, Sanino A, Stancanello J, Tei L, Aime S (2008) Chem Biodivers 5:1901–1912

13) Dumas S, Jacques V, Sun W-C, Troughton JS, Welch JT, Chasse JM, Schmitt-Willich H, Caravan P (2010) Invest Radiol 45:600–612

14) Caravan P, Parigi G, Chasse JM, Cloutier NJ, Ellison JJ, Lauffer RB, Luchinat C, McDermid SA, Spiller M, McMurry TJ (2007) Inorg Chem 46:6632–6639

15) Aime S, Calabi L, Cavallotti C, Gianolio E, Giovenzana GB, Losi P, Maiocchi A, Palmisano G, Sisti M (2004) Inorg Chem43:7588–7590

16) Gugliotta G, Botta M, Giovenzana GB, Tei L (2009) Bioorg Med Chem Lett 19:3442–3444

17) Gugliotta G, Botta M, Tei L (2010) Org Biomol Chem 8:4569–4574

18) Battistini E, Gianolio E, Gref R, Couvreur P, Fuzerova S, Othman M, Aime S, Badet B, Durand P (2008) Chem Eur J 14:4551–4561

19) Aime S, Botta M, Fedeli F, Gianolio E, Terreno E, Anelli PL (2001) Chem Eur J 7:5261–5269

20) Aime S, Gianolio E, Arena F, Barge A, Martina K, Heropoulosc G, Cravotto G (2009) Org Biomol Chem 7:370–379

21) Martinelli J, Fekete M, Tei L, Botta M (2011) Chem Commun 47:3144–3146

22) Eftink MR, Andy ML, Bystrom K, Perlmutter HD, Kristolt DS (1989) J Am Chem Soc 111:6765-6772

23) Harries D, Rau DC, Parsegian VA (2005) J Am Chem Soc 127:2184–2190

24) Wang Y-M, Lin S-T, Wang Y-J, Sheu R-S (1998) Polyhedron 17:2021–2028

25) Ranganathan RS, Fernandez ME, Kang SI, Nunn AD, Ratsep PC, Pillai KMR, Zhang X, Tweedle MF (1998) Invest Radiol 33:779

26) Gianolio E, Ramalingam K, Song B, Kalman F, Aime S, Swenson R (2010) Inorg Chem Commun 13:663–665

27) Rudovsky J, Botta M, Hermann P, Koridzec A, Aime S (2006) Dalton Trans 2323–2333

28) Mastarone DJ, Harrison VSR, Eckermann AL, Parigi G, Luchinat C, Meade TJ (2011) J Am Chem Soc 133:5329–5337

29) Martin VV, Ralston WH, Hynes MR, Keana JFW (1995) Bioconjug Chem 6:616

30) Nair SA, Kolodziej AF, Bhole G, Greenfield MT, McMurry TJ, Caravan P (2008) Angew Chem Int Ed 47:4918

31) Zhang Z, Kolodziej AF, Qi J, Nair SA, Wang X, Case AW, Greenfield MT, Graham PB, McMurry TJ, Caravan P (2010) New J Chem 34:611

32) Tei L, Gugliotta G, Avedano S, Giovenzana GB, Botta M (2009) Org Biomol Chem 7:4406–4414

33) Caravan P, Astashkin AV, Raitsimring AM (2003) Inorg Chem 42:3972–3974

34) Lipari G, Szabo S (1982) J Am Chem Soc 104:4546–4559

35) Lipari G, Szabo S (1982) J Am Chem Soc 104:4559–4570

36) Muller RN, Raduchel B, Laurent S, Platzek J, Pierart C, Mareski P, Vander Elst L (1999) Eur J Inorg Chem 1999:1949–1955

37) Fang J, Nakamura H, Maeda H (2011) Adv Drug Deliv Rev 63:136–151

38) Parac-Vogt TN, Kimpe K, Laurent S, Vander Elst L, Burtea C, Chen F, Muller RN, Ni Y, Verbruggen A, Binnemans K (2005) Chem Eur J 11:3077–3086

4. AAZTA-dimer functionalization as a multimodal optical-MRI imaging reporter

The prevalence of age-associated neurodegenerative diseases is increasing rapidly. About 40 million people worldwide are affected by diseases like Alzheimer's Disease (AD) or Parkinson's Diseases (PD). Due to the ageing population, their incidence is expected to triple in the next forty years. This creates an urgent need for early diagnosis of the disease to enable treatment at an early stage. In spite of extensive research in the field, the cause and progression of such diseases is still not well understood.

Neurodegenerative processes are closely related to the alterations of the brain network, for example reduced connectivity between the hippocampus and other regions such as prefrontal cortex and cingulate cortex [1]. One possible approach to successful therapy refers to the brain's remarkable ability to change and reorganize itself, termed brain plasticity. It was long thought that brain plasticity declined with age. However, recent studies demonstrated that this is not the case, even in the early stages of disease [2]. Consequently more extensive studies are needed to understand the mechanisms underlying these processes. The methodology to investigate brain connectivity and plasticity has made substantial progress in the last few years. Newly developed animal models for neurodegenerative diseases in combination with improved neuroimaging technologies now provide researchers with unique tools to study disease processes and to investigate preclinically the effects of potential treatments in order to acquire knowledge that will ultimately inform clinical practise [3,4]. In addition to the current post-mortem techniques scientists will be able to take advantages of different less- or non-invasive modalities.

Nevertheless, none of the developed methods is so far able to deliver complete information on this issue. The most commonly used in vivo imaging techniques in animal models are positron emission tomography (PET) and MRI, each of which has its own advantages and disadvantages. Whereas the former suffers from poor spatial resolution, the latter is more limited in the functional and neurochemical

measurements it is currently capable of. [5,6]. Diffusion tensor imaging (DTI) is the most popular MRI technique widely used in the clinic and providing a sensitive method to detect white matter changes in subjects with AD. Unfortunately, it seems that the method is not reliable for the investigation of the grey matter for example the neuronal connections present in the brain cortex [7].

An ideal strategy would be to develop methods that combine spatiotemporally-resolved MR imaging with other invasive neuroscientific modalities. Manganese-enhanced MRI (MEMRI) represents one of the approaches undertaken towards in vivo studying of neuronal connectivity by means of MR imaging [8]. However, difficulties in understanding manganese transport processes, due to their multi-synaptic nature, as well as the potential toxicity of the Mn^{2+} in the tissue, restricts its applicability [9,10]. Another promising approach which could be developed is one where paramagnetic tracers share transport properties with traditional monosynaptic histological markers. Recent attempts to conjugate paramagnetic Gd^{3+} complexes with classical neuroanatomical tracers such as biocytin, cholera toxin subunit B (CTB) or dextran amine have demonstrated the potential of such systems to act as contrast agents, thus offering an excellent alternative to MEMRI [11-13].

In this chapter we discuss the development of a multi-track methodology for longitudinal investigations of the monosynaptic connections between specific brain areas using MR and optical imaging techniques in combination with the other neuroscientific modalities. In particular, we used dextran amine as it is extensively used in neuroanatomical research as a core molecule conjugated to MR and optical reporters and because of two other important properties [14]. First, unlike CTB and other retrograde tracers, dextran is transported predominantly anterogradely (labelling begins at the dendrites and cell bodies and the dye is transported out to the axons and their terminals). Very often this type of transport is preferable in neuroanatomical research because it enables the projection targets of individual or groups of cells to be charted within the central nervous system. Second, in contrast to biocytin and many other "fast" tracers where the labelling occurs in 24 h, dextran belongs to the group of "slow" transported agents. Such types of neuronal tracing could be preferable for different kinds of longitudinal studies in vivo.

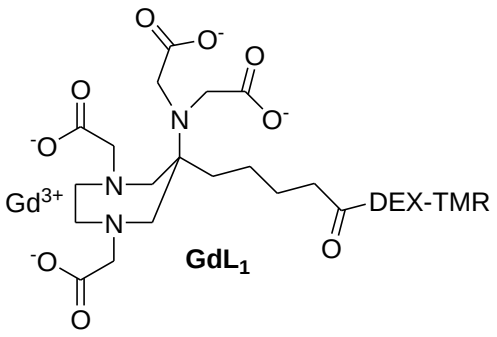

Scheme 4.1: Structure of GdL_1.

Tetramethylrhodamine was used as an optical reporter for the evaluation of the cellular uptake via fluorescence microscopy and additional histological control of cellular transport. The bimetallic Gd^{3+} AAZTA-like ligand already discussed in Chapter 3 was attached to a dextranerhodamine conjugate through a thiourea linkage (Scheme 4.1). The relaxometric behaviour of the dual-imaging probe was compared with the one relative to the monetallic Dextran-TMR-GdL_1 developed by Mamedov *et al* [13].

4.1 Synthetic procedure

Conjugation of the fluorescent dye to dextran was carried out by the reaction of dextran amine with 2 eq of tetramethylrhodamine isothiocyanate in water/DMF solution at pH 8.5 resulting in Dextran tetramethylrhodamine (Dextran-TMR). An excess of the fluorophore was used to avoid or reduce the amount of the unreacted dextran which is difficult to separate from the reaction mixture. The conjugate was purified using a Minimate ultrafiltration device (Pall Life Science.) to remove excess of TMR. This part of the synthesis was performed in Tubingen by Dr. Mamedov group.

For the synthesis of Dextran-TMR-Gd_2L_2, isothiocyanate containing dimer [15] was conjugated to Dextran-TMR in DMF/carbonate buffer at pH 9. In particular, to a solution of Dextran-TMR (30 mg, 0.003 mmol) in DMF (5 mL) and K_2CO_3 1M (5 mL), DIPEA (5,2 mL, 0.03 mmol) and HCl 1M were added to bring the pH to 9. Then, solid

Gd_2L_2 (38,5 mg, 0.03 mmol) was added to the reaction mixture which was stirred at room temperature for 36 h. The solution was then purified by ultracentrifugation using Vivaspin© (cut-off 5000 Da) and dried by lyophilisation obtaining pure Dextran-TMR-Gd_2L_2 as a purple solid (47 mg). The Gd^{3+} concentration in the probes was calculated using the bulk magnetic susceptibility (BMS) shift method [16,17] and confirmed by ICP-MS. Dextran:Gd^{3+} ratio was estimated to be 1:3.4 for Dextran-TMR-Gd_2L_2 (on average 1.7 eq of complex per 1 eq dextran).

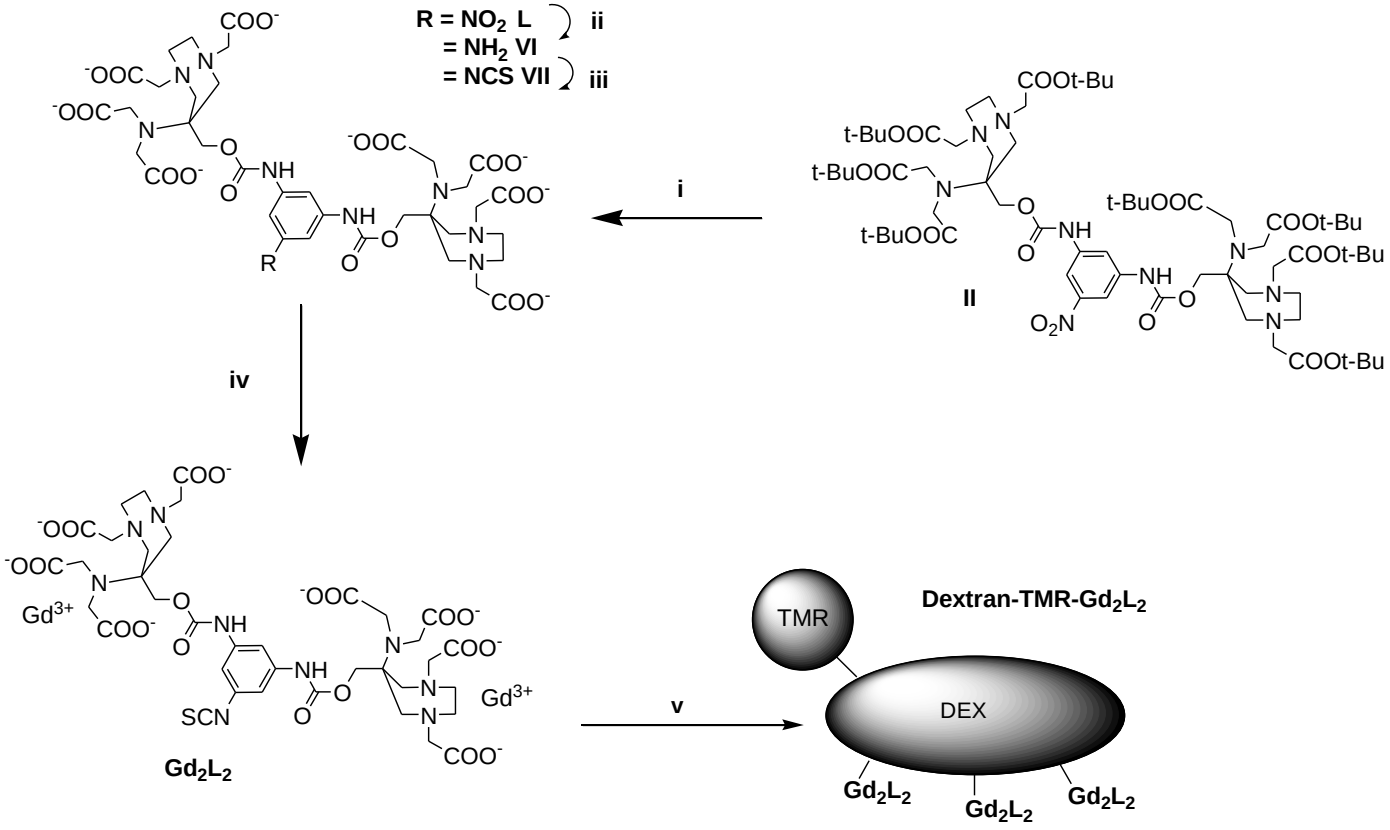

Scheme 4.2: Synthesis of the dual-imaging probe Dextran-TMR-Gd_2L_2; i) TFA, CH_2Cl_2, rt, overnight; ii) Pd/C 10%, H_2, MeOH, rt, 3h; iii) Cl_2CS, CH_2Cl_2, $NaHCO_3$ sat, rt, 3h; iv) $GdCl_3$, H_2O, rt; v) DEX-TMR, DiPEA, DMF, K_2CO_3 1 M, rt, 48h.

4.2 Relaxometric measurements

Two different probes were studied, containing a monomeric GdAAZTA system (GdL_1) (ref Mamedov) in case of Dextran-TMR-GdL_1 and dimeric (Gd_2L_2) in case of Dextran-TMR-Gd_2L_2 . The two probes resulted also in different dextran: Gd^{3+} ratio that was estimated to be ~1:3 for Dextran-TMR-GdL_1 and 1:3.4 for Dextran-TMR-Gd_2L_2 (on average 1.7 eq of dimeric complex per 1 eq dextran).

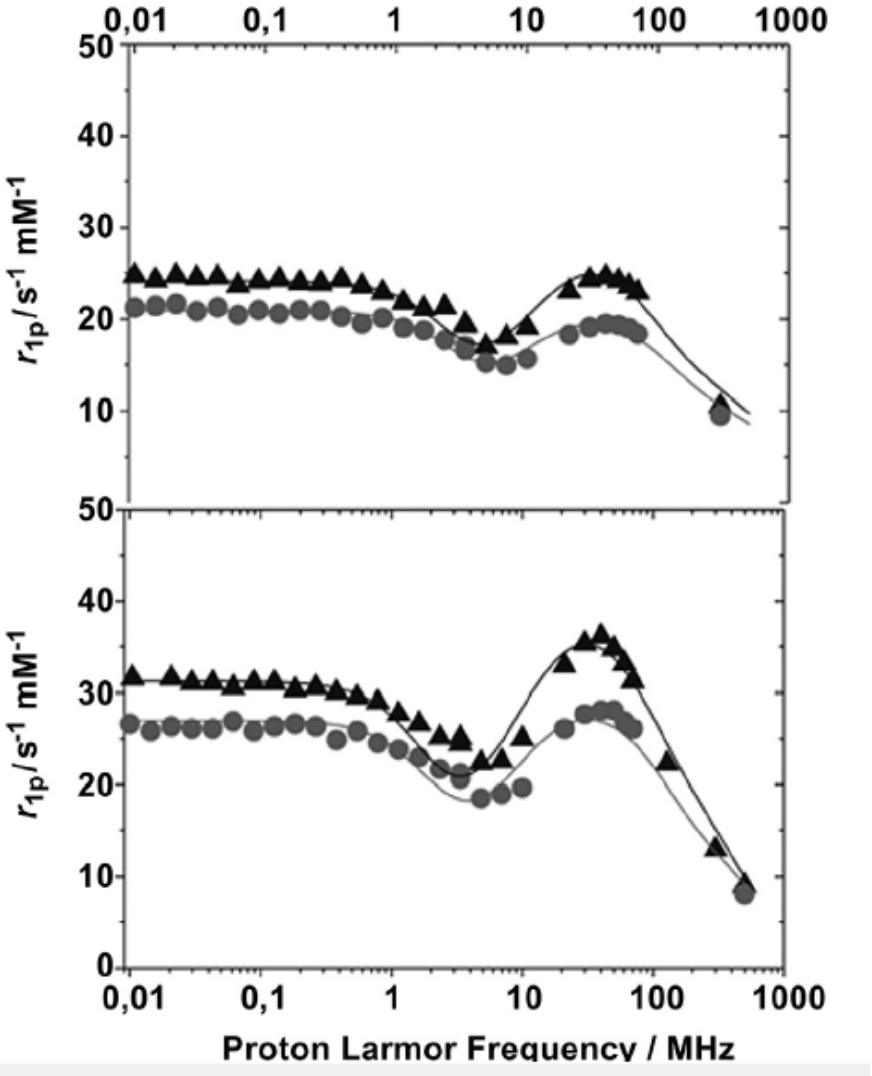

Figure 4.1. $1/T_1$ NMRD profiles of aqueous solutions (pH = 7.4) of Dextran-TMR-GdL_1 (upper) and of Dextran-TMR-Gd_2L_2 (lower) at 298 K (triangles) and 310 K (circles).

The efficacy of the paramagnetic systems as MRI reporters was assessed by evaluating the magnetic field dependency of the relaxivity (r_{1p}, the longitudinal relaxation enhancement of the water protons induced by a 1 mM concentration of the paramagnetic metal ions) in water at pH 7.4. The NMRD profiles (Figure 4.1) were measured at 298 and 310 K over a wide range of values, from 0.00024 to 11.7 T (corresponding to 0.01-500 MHz proton Larmor frequencies). The shape and amplitude of the profiles are characteristic of slowly tumbling Gd-based systems: a low fields region where r_{1p} assumes a nearly constant value (~0.01-0.8 MHz), a dispersion around 1-3 MHz and a high field broad peak associated with the occurrence of a restricted molecular tumbling [18].

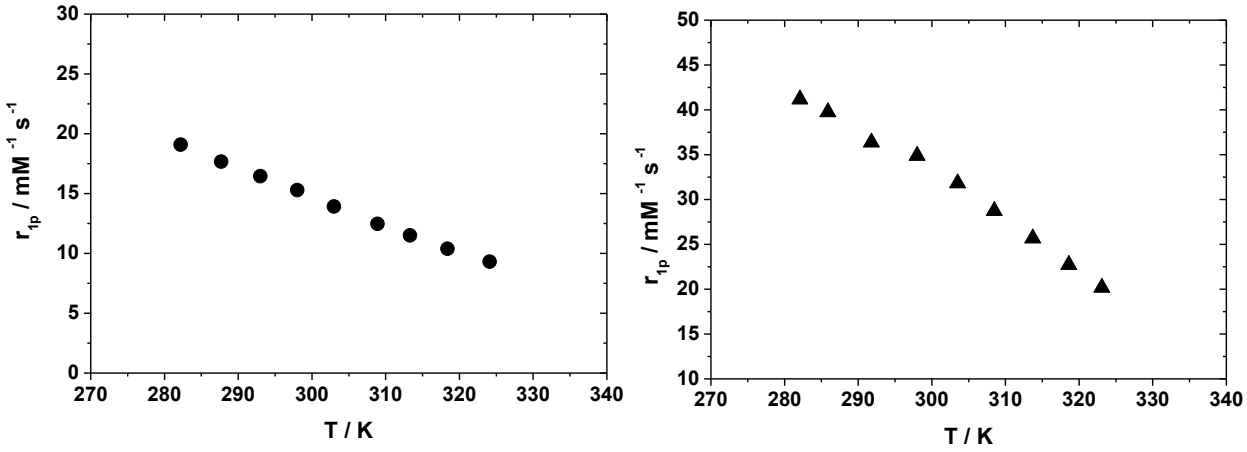

Figure 4.2: r_1 as a function of temperature for Dextran-TMR-GdL$_1$ (*left*) and Dextran-TMR-Gd$_2$L$_2$ (*right*) (40 MHz, pH 7). For both the probes the behaviour is consistent with a fast water exchange regime system.

	Dextran-TMR-GdL$_1$			Dextran-TMR-Gd$_2$L$_2$		
Field	r_1	r_2	r_2/r_1	r_1	r_2	r_2/r_1
7 T	10.8	25.0	2.3	12.9	52.7	4.1

Table 4.1: r1, r2 and r2/r1 (mM 1 s1) data measured in PBS buffer at 298 K.

The maxima are centred at about 40 MHz (1 T) for both systems and correspond to $^{298}r_{1p}$ values of 36.1 mM^{-1} s^{-1} for Dextran-TMR-Gd_2L_2 and 24.6 mM^{-1} s^{-1} for Dextran-TMR-GdL_1 . The greater high field relaxivity enhancement and sharper peak for Dextran-TMR-Gd_2L_2 is indicative of a slower rotational dynamics. Longitudinal and transverse relaxation rates (R_1 and R_2) for both MRI probes were also measured at 7 T in PBS buffer (298 K; pH = 7.4) and the corresponding values are reported in Table 4.1

	Dextran-TMR-GdL_1	Dextran-TMR-Gd_2L_2
Δ^2 (10^{19} s^{-2})	1.2 ± 0.1	1.0 ± 0.1
$^{298}\tau_V$ (ps)	47 ± 3	44 ± 2
$^{298}\tau_{Rg}$ (ns)	1.7 ± 0.2	1.7 ± 0.1
$^{298}\tau_{RI}$ (ns)	0.32 ± 0.06	0.44 ± 0.03
S^2	0.10 ± 0.01	0.22 ± 0.02
$^{298}\tau_M$ (ns)[b]	80	80

Table 4.2: Selected best-fit relaxation parameters obtained from the analysis of the $1/T_1$ NMRD profiles for Dextran-TMR-GdL_1 and for Dextran-TMR-Gd_2L_2.

4.3 Cell study

Efficient cell internalization, effective labelling and transporting properties are essential for the tracer molecule to mark the neuronal tract. According to published data and the long experience of the neuroanatomists, dextran based markers are among the best tracers because of their detailed labelling properties [19]. However, there is strong dependence of cellular uptake and transporting properties on the nature of the applied fluorophore [20]. Most obviously the structure of the MR reporter should also influence the tracing ability of the final molecule. Therefore, in our cell studies we

examined how the MR reporter modifications would affect the labelling characteristics of the final molecules containing the same type of fluorophore.

To investigate the cellular uptake of Dextran-TMR-Gd_2L_2 in comparison with Dextran-TMR-GdL_1 , differentiated mouse N18 neuroblastoma cells were incubated with solutions of tracers under physiological conditions in serum-containing medium for 18 h. The results obtained by fluorescence microscopy clearly demonstrated that the nature of the MR reporter does indeed influence the uptake properties of the tracer (Figure 4.3).

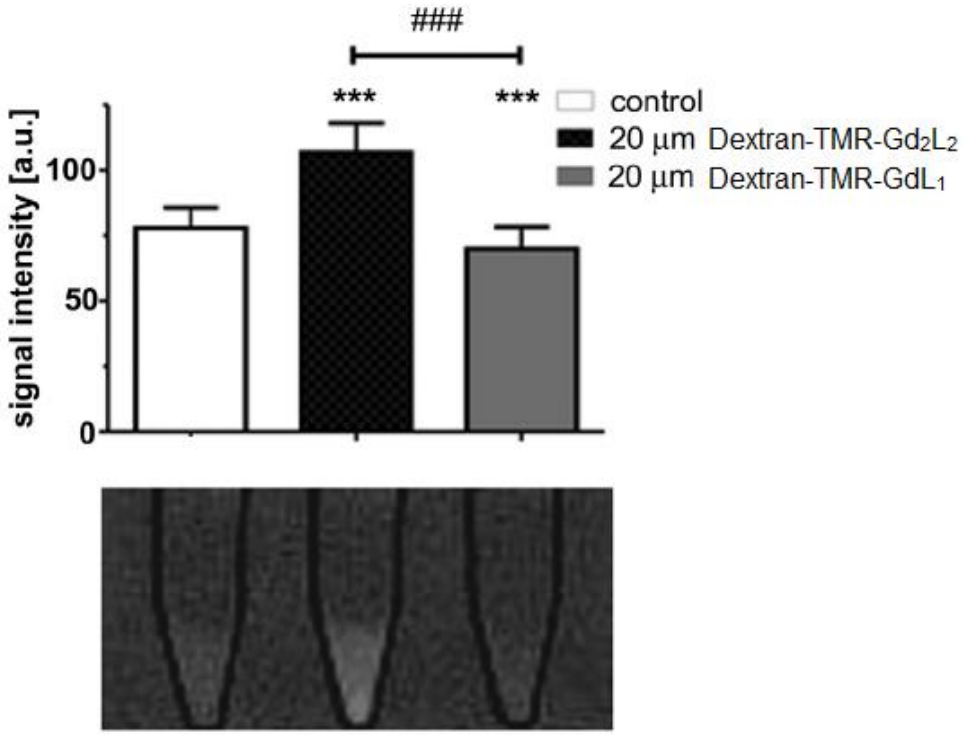

Figure 4.3: T_1-weighted MR images of the differentiated N18 cells labelled with 20 µM [Gd^{3+}] of Dextran-TMR-GdL_1 and Dextran-TMR-Gd_2L_2 (down) and analysis of the corresponding signal intensities (up). (Values represent mean ± SD, n = 76 voxels. ***p < 0.001 statistically different compared to control, ***p < 0.001 statistical difference between both probes; ANOVA, Tukey's post test.)

Although both tracer molecules were taken up by the cells, they were located in different compartments. In fact, while Dextran-TMR-GdL_1 was mainly concentrated in

cell bodies, Dextran-TMR-Gd_2L_2 was mainly observed in vesicles surrounding the nucleus and along the cell membrane.

We assume that one of the reasons for such different behaviour could be the changes in lipophilicity due to the additional aromatic ring in the case of Dextran-TMR-Gd_2L_2 which can influence the mechanism of uptake and accumulation.

The spin-lattice relaxation times (T_1) of N18 cells incubated with 20 mM solutions of each paramagnetic tracer were measured at a 3T horizontal scanner. The control cells were treated in the same way, but without the tracers. Cells were placed into Eppendorf tubes and T_1 weighted images were acquired. Significant positive contrast enhancement was observed for the Dextran-TMR-Gd_2L_2 loaded cells in comparison to the control experiment (Figure 4.3).

For Dextran-TMR-GdL_1 the signal intensity was not much differing from the control. To explain the obtained results, the Gd^{3+} content of the cells from the MR experiments was determined in mineralised cell lysates by ICP-MS. Only a small amount could be found for Dextran-TMR-GdL_1 (~0.07 nmol/10^6 cells). This is significantly above the detection limit of ICP-MS for such cell lysates (~0.01 nmol/10^6 cells) but obviously not sufficient to enhance contrast in the corresponding MR images. However, our previous experiments demonstrated considerable enhancement of the MR signal after incubation of the cells with 50 mM of Dextran-TMR-GdL_1 [13]. In contrast, about 20-fold more Gd^{3+} was seen for 20 mM Dextran-TMR-Gd_2L_2 (1.41 nmol/10^6 cells) in the present study. Thus, Dextran-TMR-Gd_2L_2 not only provides better signal enhancement due to its increased longitudinal relaxivity but also is internalised much better than Dextran-TMR-GdL_1 into the cells.

The exact reason for this behaviour remains unclear but the altered lipophilicity of the molecule might be involved as mentioned above. The in cellulo MR results indicate that the bis-macrocyclic derivative was able to deliver a stronger signal and thus might be better suited for in vivo experiments than the mono-macrocyclic tracer.

4.4 Conclusions

Multimodal paramagnetic neuronal tracers with variable MR reporting moieties were developed. Physico-chemical characteristics were compared with *in vivo* behaviours, investigated by Dr. Mamedov group in Tubingen, between mono and bimetallic derivatives. It was found that the derivative containing the dimeric AAZTA moiety demonstrated stronger paramagnetic properties and as a result had a greater influence on the MR signal. It was also showed that as with the nature of the fluorophore, the structure of the MR reporter can influence cellular uptake and transport properties of dextran-based tracers. In spite of some differences in transport behaviour, both compounds resulted in MR signal enhancement in known targets of the primary motor cortex after an optimal 10 days post injection. Taking advantage of the multimodality of the developed tracers, MR results were confirmed by optical microscopy of the histological slices from the same animals. These encouraging results re-assure us that such optimized compounds can be used for particular neuroanatomical investigations. Depending on the final application, this technique can also be combined with other methods used in neuroscience (DTI, electrophysiology) providing essential information for in vivo whole brain longitudinal studies of monosynaptic connections under physiological and pathophysiological conditions.

References

1) Filippi M, Agosta F. Structural and functional network connectivity breakdown in Alzheimer's disease studied with magnetic resonance imaging techniques. J Alzheimers Dis 2011;24:455-74.

2) Belleville S, Clément F, Mellah S, Gilbert B, Fontaine F, Gauthier S. Trainingrelated brain plasticity in subjects at risk of developing Alzheimer's disease. Brain 2011; 134:1623-34.

3) Strome EM, Doudet DJ. Animal models of neurodegenerative disease: insights from in vivo imaging studies. Mol Imaging Biol 2007; 9:186-95.

4) Yanga J, Wadghirib YZ, Hoangb DM, Tsuic W, Suna Y, Chunga E, et al. Detection of amyloid plaques targeted by USPIO-A beta 1-42 in Alzheimer's disease transgenic mice using magnetic resonance microimaging. Neuroimage 2011; 55:1600-9.

5) Brust P, Patt JT, Deuther-Conrad W, Becker G, Patt M, Schildan A, et al. In vivo measurement of nicotinic acetylcholine receptors with [^{18}F]norchloro-fluorohomoepibatidine. Synapse 2008; 62:205-18.

6) Dagher A, Nagano-Saito A. Functional and anatomical magnetic resonance imaging in Parkinson's disease. Mol Imaging Biol 2007; 9:234-42.

7) Stebbins GT, Murphy CM. Diffusion tensor imaging in Alzheimer's disease and mild cognitive impairment. Behav Neurol 2009; 21:39-49.

8) Lee JH, Koretsky AP. Manganese enhanced magnetic resonance imaging. Curr Pharm Biotechnol 2004; 5:529-37.

9) Eschenko O, Canals S, Simanova I, Beyerlein M, Murayama Y, Logothetis NK. Mapping of functional brain activity in freely behaving rats during voluntary running using manganese-enhanced MRI: implication for longitudinal studies. Neuroimage 2010; 49:2544-55.

10) Chuang KH, Koretsky AP. Accounting for nonspecific enhancement in neuronal tract tracing using manganese enhanced magnetic resonance imaging. Magn Reson Imaging 2009; 27:594-600.

11) Wu CW-H, Vasalatiy O, Liu N, Wu H, Cheal S, Chen D-Y, et al. Development of a MR-visible compound for tracing neuroanatomical connections in vivo. Neuron 2011; 70:229-43.

12) Mishra A, Schüz A, Engelmann J, Beyerlein M, Logothetis NK, Canals S. Biocytin-derived MRI contrast agent for longitudinal brain connectivity studies. ACS Chem Neurosci 2011; 2:578-87.

13) Mamedov I, Engelmann J, Eschenko O, Beyerlein M, Logothetis NK. Dualfunctional probes towards in vivo studies of brain connectivity and plasticity.

ChemComm 2012; 48:2755-7.

14) Reiner A, Veenman L, Medina L, Jiao Y, Del Mar N, Honig MG. Pathway tracing using biotinylated dextran amines. J Neurosci Methods 2000; 103:23-37.

15) Gugliotta G, Botta M, Tei L. AAZTA-based bifunctional chelating agents for the synthesis of multimeric/dendrimeric MRI contrast agents. Org Biomol Chem 2010; 8:4569-74.

16) Peters J, Huskens J, Raber DJ. Lanthanide induced shifts and relaxation rate enhancements. Prog Nucl Magn Reson Spectrosc 1996; 28:283-350.

17) Corsi DM, Platas-Iglesias C, van Bekkum H. Determination of paramagnetic lanthanide(III) concentrations from bulk magnetic susceptibility shifts in NMR spectra. J Magn Res Chem 2001; 39:723-6.

18) Botta M, Tei L. Relaxivity enhancement in macromolecular and nanosized GdIII -based MRI contrast agents. Eur J Inorg Chem 2012; 5:1945-60.

19) Kobberta C, Appsb R, Bechmannc I, Lanciegod JL, Meye J, Thanosa S. Current concepts in neuroanatomical tracing. Prog Neurobiol 2000; 62:327-51.

20) Nance DM, Burns J. Fluorescent dextrans as sensitive anterograde neuroanatomical tracers: applications and pitfalls. Brain Res Bull 1990; 25:139-45.

5. Lipid nanoparticles including multimeric Gd^{3+} complexes

As thoroughly debated in the introductive chapter, lipid nanoparticles as micelles and liposomes have been widely investigated and employed for the development of slow tumbling, and thus high relaxivity MRI probes. The aim of the work presented in this chapter is to synthesize mono- and multimeric amphiphilic AAZTA-based paramagnetic complexes, and investigate the capability of these systems of generating lipid nanoparticles. The relaxometric study on these lipidic nanoparticles was carried out in order to compare the ability of the different multimeric anphiphilic probes to generate contrast with respect to the monomer. Moreover, this approach was aimed at understanding the rotational dynamics of these nanoprobes that have not been investigated so far.

The critical point is the degree of correlation between local motion of the complex and global rotation of the nanoparticle. The idea was to design a slow tumbling system (slow global rotation), in which the paramagnetic amphiphilic probes are encapsulated into the nanoparticle (self-assembling micelles, mixed micelles, liposomes etc.) maintaining as higher as possible the local rigidity of the systems. This is because often slow tumbling systems doesn't show the appropriate increase in terms of relaxivity expected for them, because of the decrease of local rigidity that affects this kind of systems.

The synthesis and characterization of the probes described in this chapter (monomer, dimer and tetramer) is directed to investigate the possibility to increase the relaxivity of slow tumbling systems using multimeric paramagnetic complexes (higher local rigidity) instead of monomeric complexes and using a double aliphatic chain to allow

a more tight interaction between hydrophobic groups and thus a slower local rotation of the complexes.

5.1 Synthetic procedure

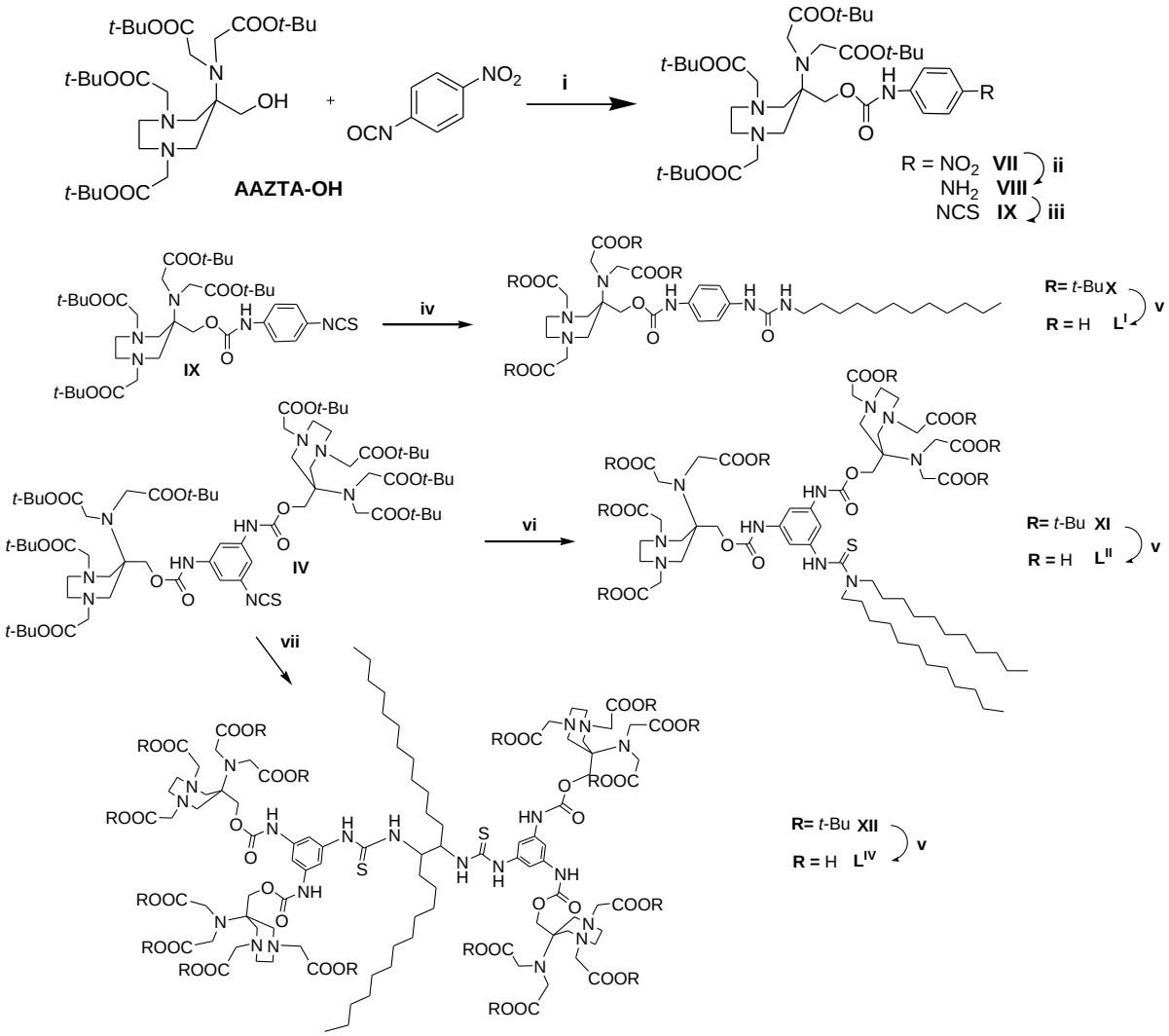

Scheme 5.1: Syntethic procedure to obtain the three mono- and multimeric amphiphilic probes; i) CH_2Cl_2, N_2, 3h, rt; ii) H_2, Pd/C 10%, MeOH, 3h, rt; iii) Cl_2CS, CH_2Cl_2, $NaHCO_3$ sat., 3h, rt; iv) $H_2NC_{12}H_{25}$, CH_2Cl_2, overnight, rt; v) TFA, CH_2Cl_2,

overnight, rt; vi) $HN(C_{12}H_{25})_2$, CH_2Cl_2, N_2 overnight, rt; vii) $(CNH_2CNH_2)(C_{12}H_{25})_2$, TEA, CH_2Cl_2, 40 °C, overnight.

While the monomeric AAZTA-like bifunctional agent **IX** was employed for the synthesis of $\mathbf{L^I}$, the AAZTA-like dimer **IV** was used for the synthesis of $\mathbf{L^{II}}$ and $\mathbf{L^{IV}}$. [1] In the all three cases the formation of the amphiphilic compounds was achieved through the formation of a thiourea bond between the isothiocyanate group of **IX** and **IV** and the amino group of 1-dodecilamine (for $\mathbf{L^I}$), 1,1-didodecilamine (for $\mathbf{L^{II}}$) and 1,2-didodecil-1,2-ethylendiamine (for $\mathbf{L^{IV}}$). The reactions were carried out with a slight excess of the corresponding amines in dichloromethane and in mild basic conditions (pH 8-9) at room temperature for the synthesis of $\mathbf{L^I}$ and $\mathbf{L^{II}}$ and in a slight excess of **IV** and warm temperature (40 °C) to obtain $\mathbf{L^{IV}}$. Products **X** and **XI** were purified by column chromatography and deprotected with trifluoroacetic acid in dichloromethane yielding the final ligands $\mathbf{L^I}$ and $\mathbf{L^{II}}$, while $\mathbf{L^{IV}}$ was purified after *t*-butyl esters deprotection directly as free ligand trough dialysis. All the intermediate products and the final ligands obtained were fully characterized by ^1H and ^{13}C NMR.

All the Gd^{3+} complexes were obtained through relaxometric titration with $GdCl_3$, obtaining the three amphiphilic complexes $\mathbf{GdL^I}$, $\mathbf{Gd_2L^{II}}$ and $\mathbf{Gd_4L^{IV}}$ (Figure 5.1).

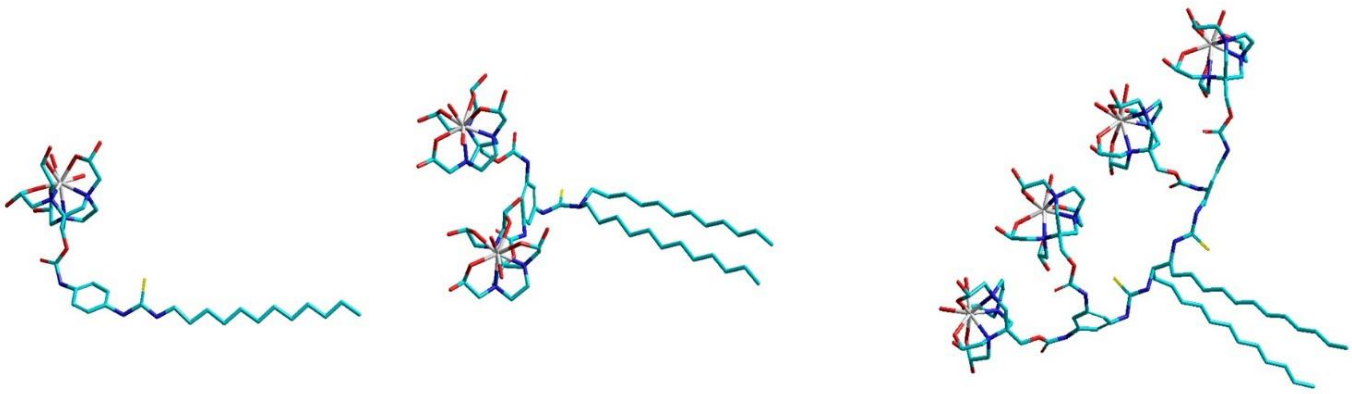

Figure 5.1: Structures of GdL^I (*left*), Gd_2L^{II} (*centre*) and Gd_4L^{IV} (*right*), obtained with Hyperchem software.

5.2 Relaxometric and DLS study

5.2.1 Self-aggregated systems

The relaxivity of **GdL^{I}**, measured at 20 MHz and 310 K, shows a value of 29.0 mM^{-1} s^{-1}, consistent with comparable systems reported in literature[2]. The ^{1}H NMRD profiles were recorded in aqueous solution at pH 7 and at 298 and 310 K (Figure 5.2).

Is easy to see how the dependence of the relaxivity on magnetic field shows a peak that reach its maximum around 40-50 MHz. This kind of peak is typical of slow tumbling systems, and in this case, jointly with the high r_{1p} for a monomeric complex, gives us the proof of the formation of a self-aggregated system.

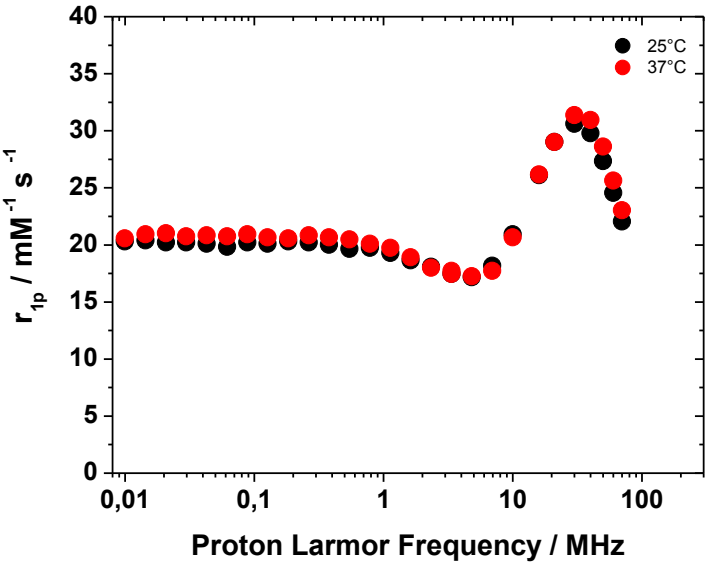

Figure 5.2: The ^{1}H NMRD profiles of GdL^{I}, pH 7, 298 (*black dots*) and 310 K (*red dots*), [Gd] = 1.09 mM.

This consideration was also confirmed trough Dynamic Light Scattering (DLS) analysis that display a value of 9.24 nm for the micelles in water solution (Figure 5.3).

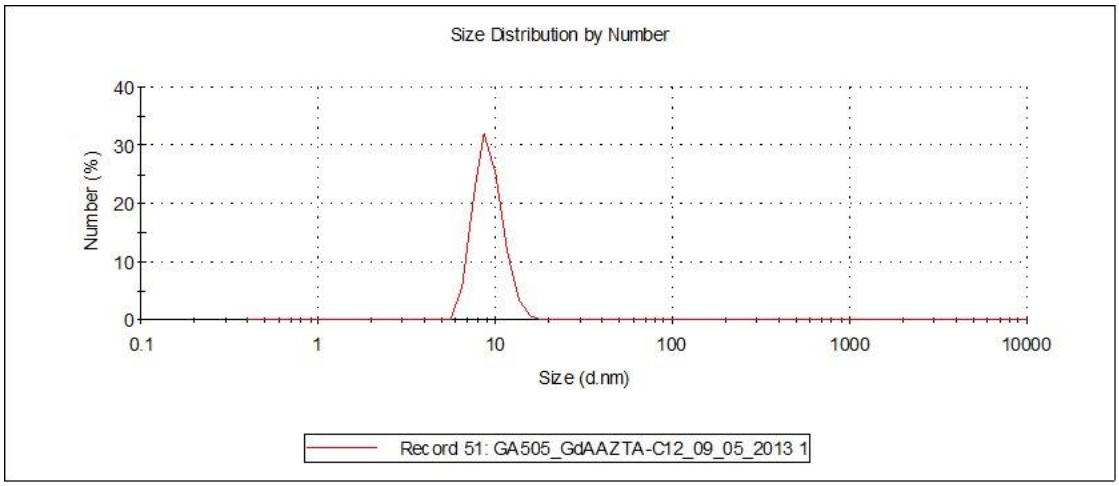

Figure 5.3: DLS analysis of a GdL^{I} solution.

The relaxometric data were analyzed using the Lipari-Szabo approach for the rotational dynamics. The presence of a local motion (τ_{RL}) superimposed to a global rotation (τ_{RG}) and the degree of correlation between them (S^2 ($0 \leq S^2 \leq 1$)) are the most important parameter to consider. The results are shown in Table 5.1.

Parameter	GdL^{I}
$^{298}r_{1p}$ (mM-1 s^{-1})[b]	29.0
$\Delta^2 / 10^{19}$ s^{-2}	1.50
$^{298}\tau_V$ / ps	44.2
$^{298}k_{ex} / 10^6$ s^{-1}	12.5
$^{298}\tau_{Rg}$ (ns)	2.4
$^{298}\tau_{RI}$ (ps)	130
S^2	0.43
q [a]	2
r / Å [a]	3.0
a / Å [a]	4.0
$^{298}D / 10^{-5}$ cm^2 s^{-1} [a]	3.1

Table 5.1: Best fit parameters obtained from the analysis of ^{1}H NMRD profiles of GdL^I.

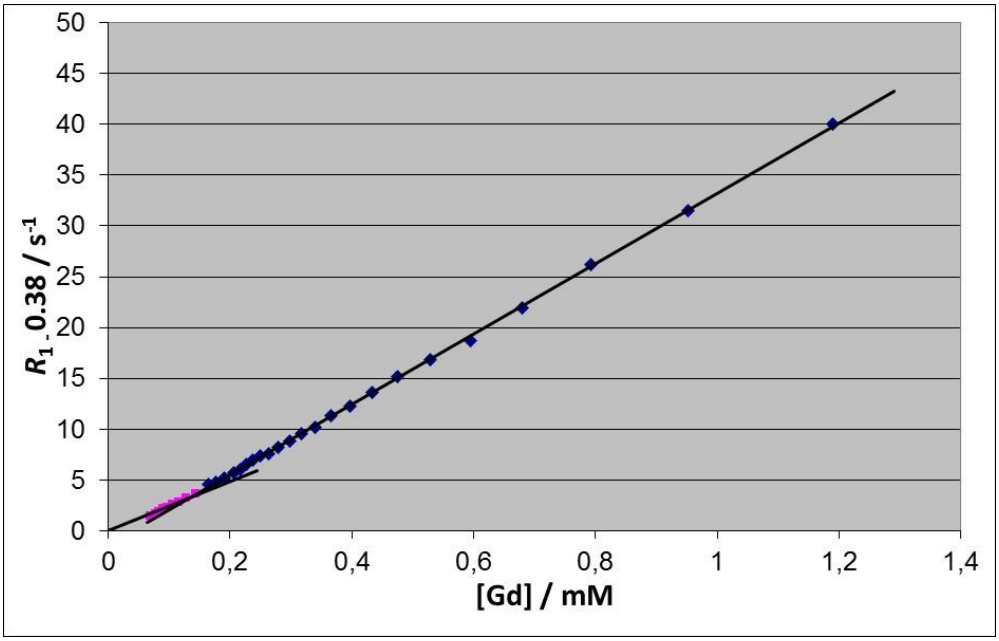

Figure 5.4: Relaxivity decrease diluting a GdL^I solution.

We then tried to identify the critical micellar concentration (cmc) of this system, trough the measure of R_1 in dilutedsolutions of the complex. Unfortunately, it was not possible to identify the cmc because, as shown in Figure 5.4, there's not a significant change in the slope of the straight line that defines the relaxivity dependence to [Gd]. The cmc value for this system is likely too low to be measured.

Even if the relaxivity of this system is in line with literature data, the behaviour of the r_{1p} as a function of temperature was not expected. As clearly showed in Figure 5.2, the NMRD profiles recorded at two different temperatures (298 and 310 K) are almost superimposed. This behaviour may indicate some variation in the coordinated water molecules exchange rate. The AAZTA cage is characterized by a fast water exchange regime,[ref aazta] and for this reason a substantial decrease of the relaxivity with increasing temperature was expected. This phenomenon could be due to different factors, as the proximity of the self-aggregated paramagnetic complexes [2], or the decrease of the water exchange rate caused by structural features.

The next step of the study was the relaxometric characterization of **Gd_2L^{II}** , and its comparison with the monomeric **GdL^{I}**.

In Figure 5.5 the ^{1}H NMRD profiles of a **Gd_2L^{II}** solution, at 298 and 310 K, are shown.

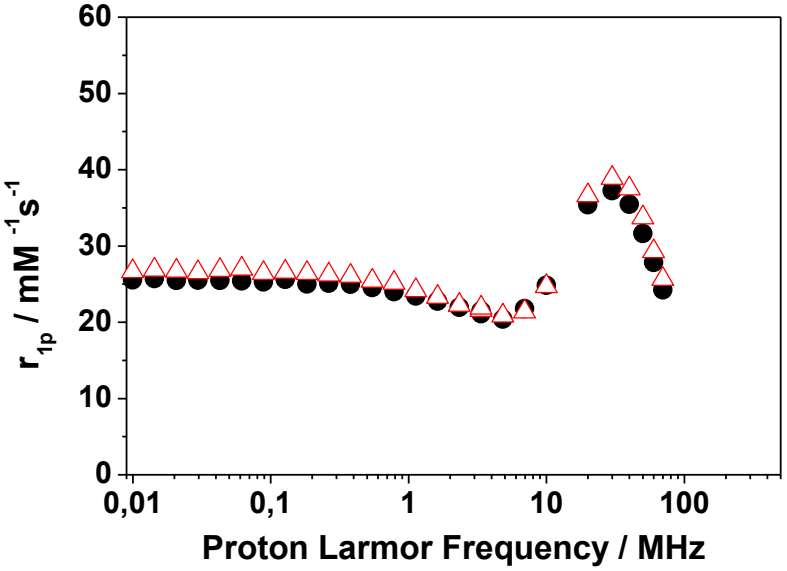

Figure 5.5: NMRD profiles of Gd_2L^{II} at 298 (*circles*) and 310 K (*triangles*), pH 7, [Gd] = 0.44 mM.

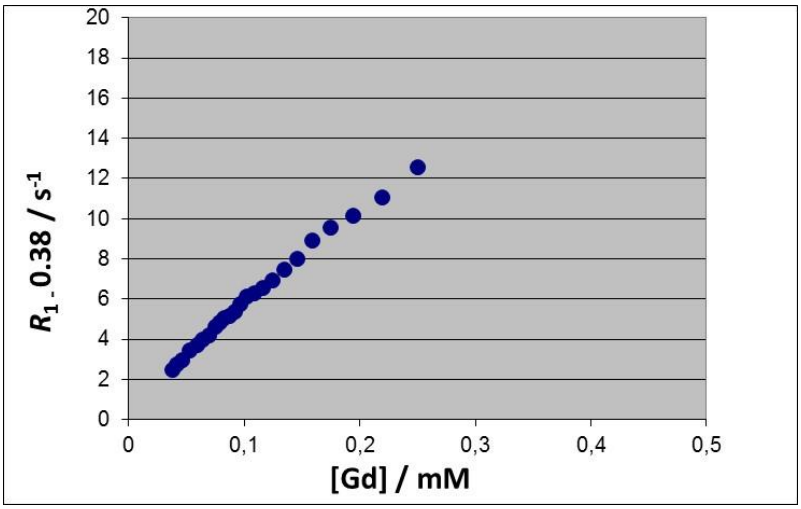

Figure 5.6: Relaxivity decrease diluting a Gd_2L^{II} solution.

For **Gd_2L^{II}** a r_{1p} value of 36.6 mM^{-1} s^{-1} was obtained at 310K and 20 MHz. The value is slightly higher than that one obtained for **GdL^{I}**, as expected for a dimeric complex. The relaxivity increase is probably due to the increased local rigidity of the system, caused by the dimeric structure and the double aliphatic chain.

The profiles are quite similar to those for **GdL^{I}**, showing a peak in the 40-50 MHz region, as expected for the self-aggregated system. Also for **Gd_2L^{II}** the profiles at two different temperatures are almost superimposed, likely implying some variation in the coordinated water molecules exchange rate. Also in this case the cmc of **Gd_2L^{II}** (Figure 5.6), could not be determined as there is no significant change in the slope of the straight line at low concentrations.

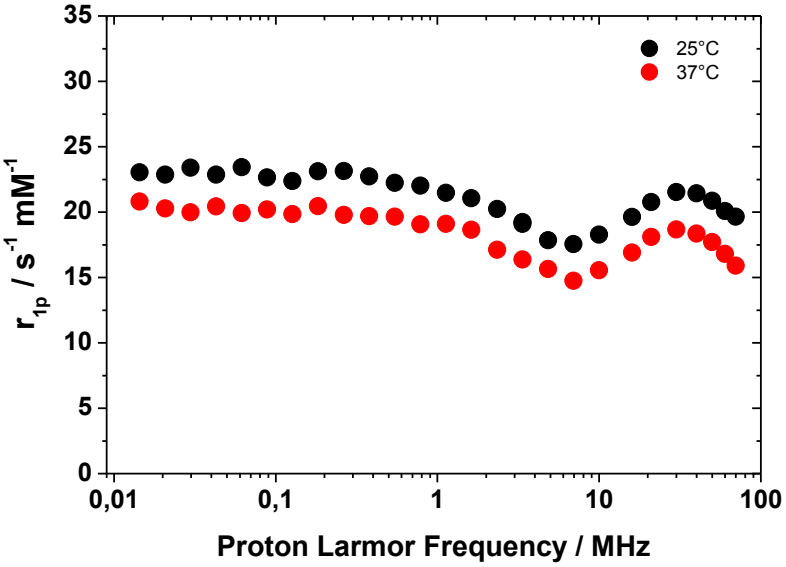

Figure 5.7: NMRD profiles of Gd_4L^{IV} at 298 (*black dots*) and 310 K (*red dots*), pH 7, [Gd] = 0.375 mM.

Finally the NMRD profiles of **Gd_4L^{IV}** were measured, at 298 and 310 K (Figure 5.7). The r_{1p} value obtained for **Gd_4L^{IV}** at 310 K and 20 MHz is 18.1 mM^{-1} s^{-1}, quite low if compared to the two complexes previously discussed. Probably, at this Gd^{3+} concentration ([**Gd_4L^{IV}**] = 0.375 / 4 = 0.0937 mM) the complex doesn't show any self-aggregation, as confirmed also by the shape of the NMRD profiles, lacking of the typical peak for slow tumbling systems at 40-50 MHz.

Moreover, the variation of r_{1p} with temperature is largely different to those measured for **GdL^{I}** and **Gd$_2$L^{II}**. In this case increasing the temperature gives rise to a significant relaxivity decrease, as clearly showed in Figure 5.8. At the moment we cannot say if the lack of self-aggregation is due to the low complex concentration or, basically, to the structure of ligand. It is possible that, for a large complex with a bulky hydrophilic head, a double C_{12} aliphatic chain is too short to allow a micellar aggregation.

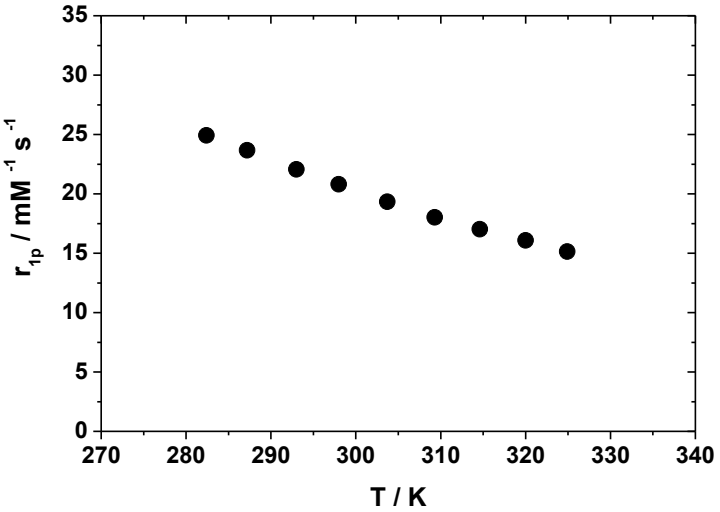

Figure 5.8: r_{1p} as a function of temperature for Gd$_4$L^{IV}, 20 MHz and [Gd] = 0.375 mM.

5.2.2 Interaction with HSA

Aliphatic chains are a widely exploited hydrophobic group for the formation supramolecular host-guest adducts with serum albumin. Thus, the capability of our amphiphilic Gd-complexes to generate inclusion compounds with HSA was investigated.

Using the previously described Proton Relaxation Enhancement method, it was possible to determine the binding parameters K_A, n, and r^b_1. To this end, a dilute solution of **GdL^{I}** was titrated with HSA, at 20 MHz and 298 K (Figure 5.9). The least-squares fit of the R_1 versus HSA concentration binding isotherm enabled us to calculate

the affinity constant (K_A = 7.94 x 10^4 M^{-1}) and the relaxivity of the adduct (r_1^b = 56.9 mM^{-1} s^{-1}, 298K and 20 MHz), fixing the *n* value to 1.

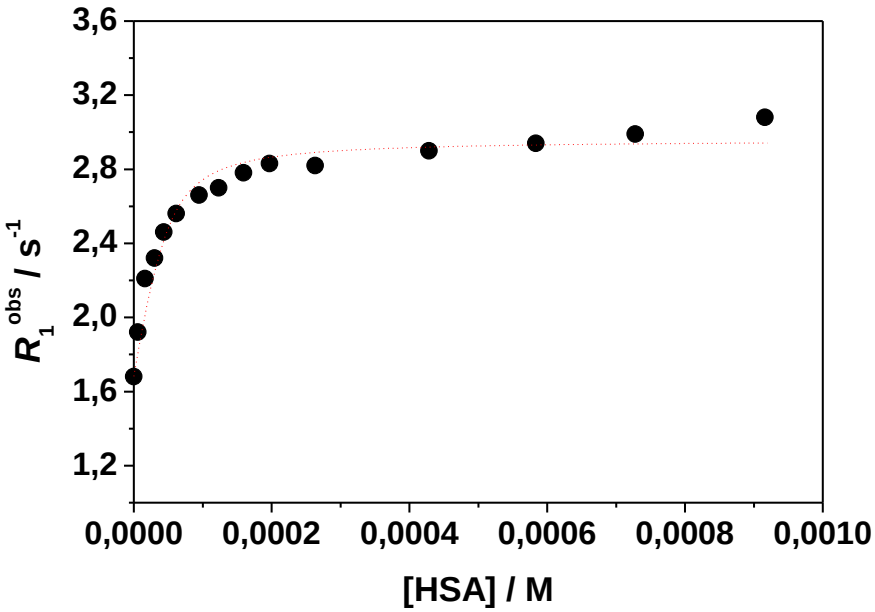

Figure 5.9: Water proton relaxation rate of a 0.046 mM aqueous solution of GdL^I as a function of increasing amounts of HSA (20 MHz, 298 K).

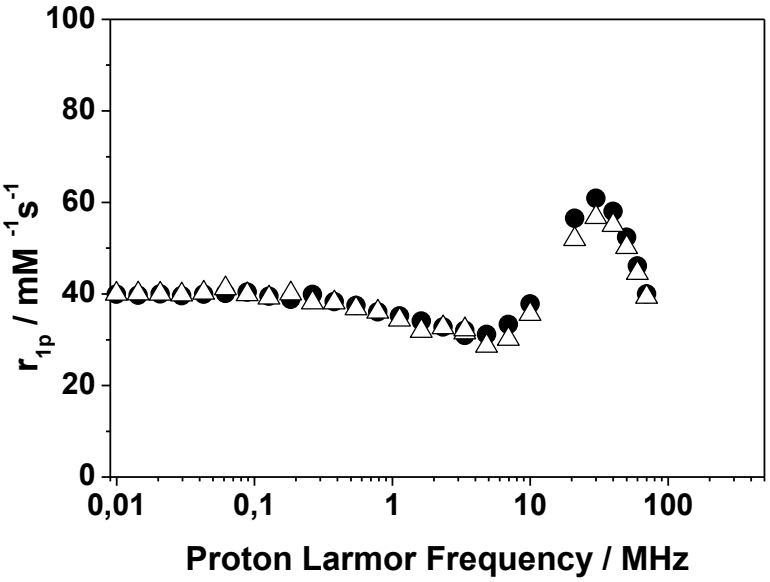

Figure 5.10: NMRD profiles of the GdL^I-HSA inclusion compound at 298 (*black circles*) and 310 K (*white triangles*), pH 7 and [Gd] = 0.046 mM.

The formation of the inclusion compound was accompanied by an increase of r_1 of 96% with respect to the isolated complex which reflects the slowing down of molecular tumbling.

In Figure 5.10 the NMRD profiles of the GdL^{I}-HSA inclusion compound are reported. A peak with maximum around 40-50 MHz can be clearly seen, suggesting the formation of the slow tumbling adduct. The trend of r_1 vs temperature is still anomalous, as the profiles at two different temperatures are almost superimposed.

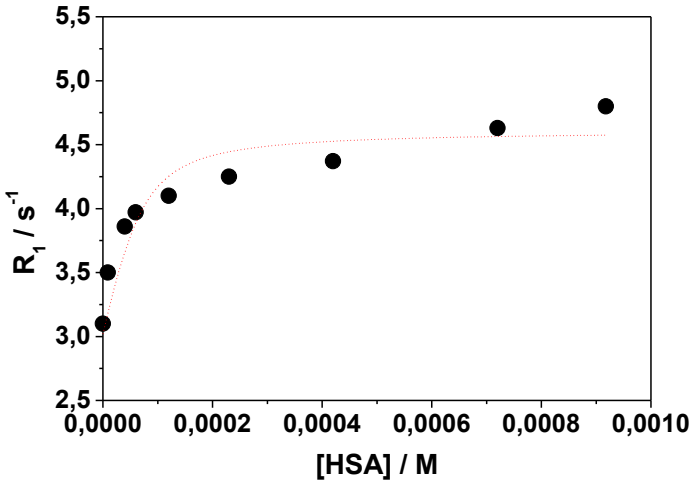

Figure 5.11: Water proton relaxation rate of a 0.066 mM aqueous solution of Gd_2L^{II} as a function of increasing amounts of HSA (20 MHz, 298 K).

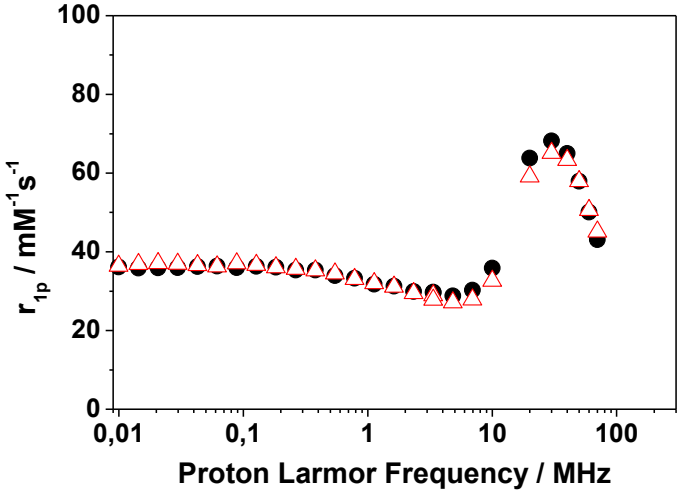

Figure 5.12: NMRD profiles of the Gd_2L^{II}-HSA inclusion compound at 298 (*black dots*) and 310 K (*triangles*), pH 7 and [Gd] = 0.066 mM.

Also the interaction between **Gd_2L^{II}** and HSA was investigated, as reported in Figure 5.11 and 5.12.

A dilute solution of **Gd_2L^{II}** was titrated with HSA, at 20 MHz and 298 K, and the fit of the R_1 versus HSA concentration binding isotherm allowed the determination of the affinity constant (K_A = 5.04 x 10^4 M^{-1}) and the relaxivity of the adduct (r_1^b = 64.1 mM^{-1} s^{-1}, 298K and 20 MHz), fixing the *n* value to 1. The formation of the inclusion compound was accompanied in this case by an increase of r_1 of 81% with respect to the self-aggregated form. The enhancement in terms of r^b_1 was remarkable, but the affinity constant for the inclusion compound is lower than for **GdL^I-HSA**, although in this case the guest group is represented by a double aliphatic chain instead of a single one. Likely, some steric problems are responsible of this lower interaction. Finally, also the **Gd_2L^{II}-HSA** inclusion compound shows no significant change in relaxivity at variable temperatures.

The interaction of **Gd_4L^{IV}** with HSA was also performed, but doesn't resulted in any significant relaxivity enhancement probably because the aliphatic chains are not sufficiently available for interaction with the hydrophobic pocket of HSA.

5.2.3 Mixed micelles and inclusion into liposome bi-layer

Aliphatic chains can be used to include amphiphilic paramagnetic complexes in liposomes or combined with phospholipids to give mixed micelles. For all the three compounds the mixed micelles were prepared with the following procedure: the dry complex was suspended in a 1:1 chloroform / methanol solution and mixed with 1,2-distearoyl-*sn*-glycero-3-phosphoethanolamine-N-[amino(polyethyleneglycol) 2000 (DSPE-PEG2000) then slowly evaporated in vacuo, to form the lipidic film, and dried.

Then, the film was rehydrated with water and filtered, obtaining the final mixed-micelles suspension.

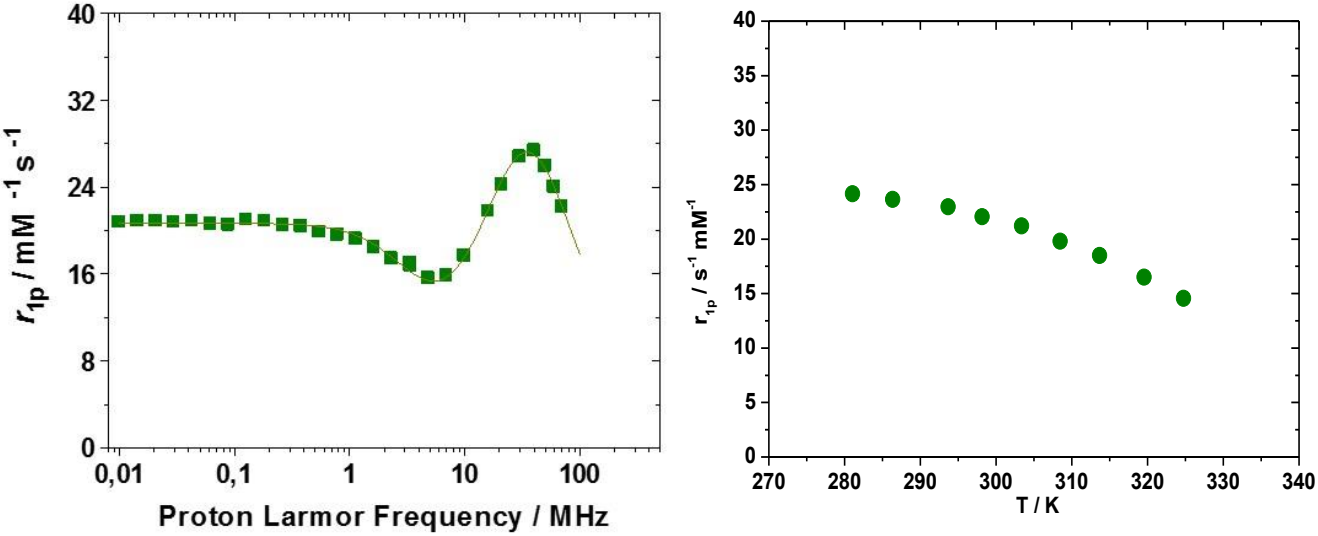

Figure 5.13: left) NMRD profile of the GdL^{I}-DSPE-PEG2000 50:50, 298 K and [Gd] = 0.776 mM; right) r_{1p} as a function of temperature, measured at 20 MHz.

In Figure 5.13 the NMRD profile of the solution containing the **GdL^{I}-DSPE-PEG2000 50:50** mixed micelles at 298 K and the r_{1p} dependence from temperature are reported. The shape of the peak in the profile is quite similar with that one related to the self-assembled complex, with slightly lower relaxivity (24.2 mM^{-1} s^{-1}) with respect to the micelles 100% made of **GdL^{I}** (29.0 mM^{-1} s^{-1}). The behaviour of relaxivity as a function of temperature is another significant difference with the self-assembled micelles, as in this case it shows the exponential decay trend typical of systems in the fast water exchange regime. The NMRD profile was also fitted with the Lipari-Szabo approach, obtaining the best-fit parameters reported in Table 5.2.

parameter	GdL^{I}-DSPE-PEG2000 50:50
$^{298}r_{1p}$ (mM-1 s^{-1})[b]	27.7
$\Delta^2 / 10^{19}$ s^{-2}	1.78
$^{298}\tau_V$ / ps	35.6
$^{298}k_{ex} / 10^6$ s^{-1}	12.5
$^{298}\tau_{Rg}$ (ns)	2.3

$^{298}\tau_{RI}$ (ps)	123
S^2	0.41
q [a]	2
r / Å [a]	3.0
a / Å [a]	4.0
$^{298}D / 10^{-5}\ cm^2\ s^{-1}$ [a]	3.1

Table 5.2: Best-fit parameters obtained from the analysis of ^{1}H NMRD profiles of GdL^I-DSPE-PEG2000 50:50.

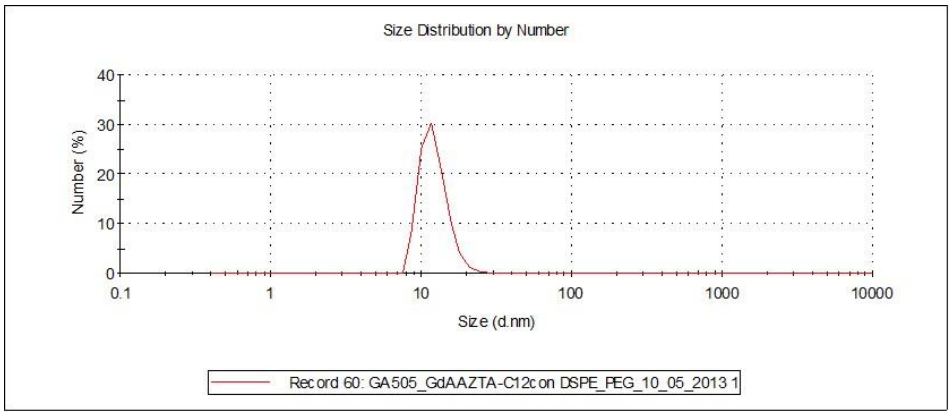

Figure 5.14: DLS analysis of the GdL^I-DSPE-PEG2000 50:50 suspension.

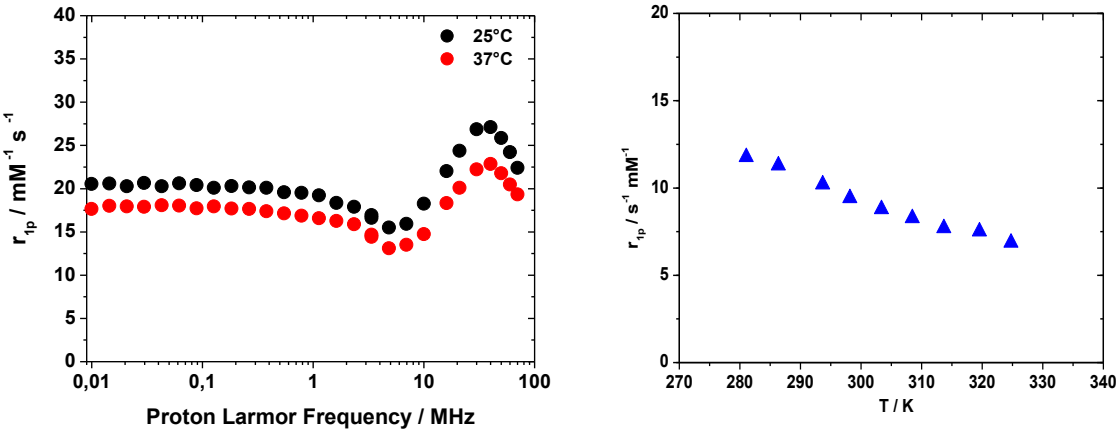

Figure 5.15: left) NMRD profile of the Gd$_2$L^{II}-DSPE-PEG2000 40:60, 298 K and [Gd] = 0.306 mM; right) r_{1p} as a function of temperature, measured at 20 MHz.

DLS analysis of the mixed micelles suspension was also performed, obtaining particles dimension of 12.2 nm (Figure 5.14).

A mixed micelles suspension was also prepared using **Gd_2L^{II}**, mixed with DSPE-PEG2000 in a different ratio (40:60).

Also in this case, r_{1p} of **Gd_2L^{II}-DSPE-PEG2000 40:60** mixed micelles (Figure 5.15) is lower than that of the pure complex (20.1 mM^{-1} s^{-1} compared to 36.6 mM^{-1} s^{-1}, at 310 K and 20 MHz), and the trend of r_{1p} as a function of temperature is again compatible with a fast water exchange regime.

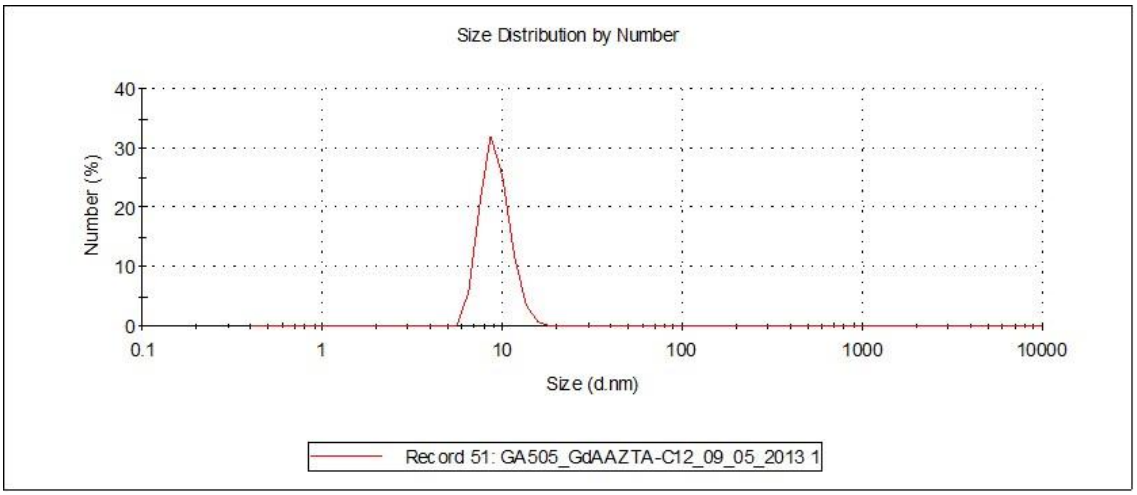

Figure 5.16: DLS analysis of the Gd_2L^{II}-DSPE-PEG2000 40:60 suspension.

In Figure 5.16 the DLS analysis for the **Gd_2L^{II}-DSPE-PEG2000 40:60** mixed micelles is reported, showing particles dimension of 9.24 nm.

Finally, micelles including **Gd_4L^{IV}** mixed with DSPE-PEG2000 in 20:80 ratio were prepared. In this case the r_{1p} value obtained for the mixed micelles suspension solution was 25.8 mM^{-1} s^{-1}, higher than the value of 20.1 mM^{-1} s^{-1} relative to the pure complex (Figure 5.17). Once again r_{1p} as a function of temperature shows a fast water regime system.

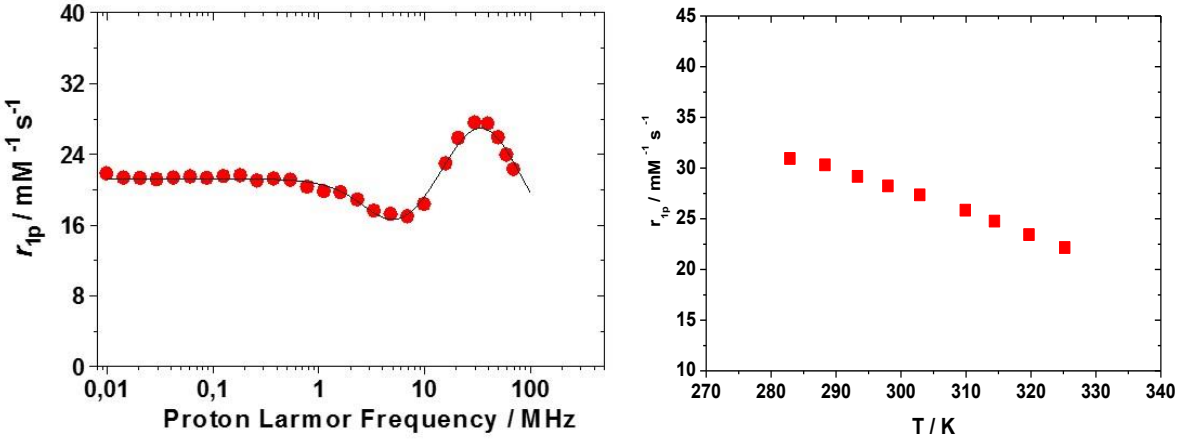

Figure 5.17: left) NMRD profile of the Gd_4L^{IV}-DSPE-PEG2000 20:80, 298 K and [Gd] = 2.7 mM; right) r_{1p} as a function of temperature, measured at 20 MHz.

The increase in relaxivity compared with the micelles 100% made by the Gd-complex is likely attributable to a more ordered disposition of the amphihilic complex on the micelle surface, maybe avoiding some interferences between near paramagnetic centres in the coordinated water molecules exchange. The NMRD profile was also fitted using the Lipari-Szabo approach and the best-fit parameters obtained this way are reported in Table 5.3.

parameter	Gd_4L^{IV}-DSPE-PEG2000 20:80
$^{298}r_{1p}$ (mM-1 s^{-1})[b]	28.1
$\Delta^2 / 10^{19}$ s^{-2}	1.77
$^{298}\tau_V$ / ps	41
$^{298}k_{ex} / 10^6$ s^{-1}	12.5
$^{298}\tau_{Rg}$ (ns)	2.3

$^{298}\tau_{RI}$ (ps)	196
S^2	0.35
q [a]	2
r / Å [a]	3.0
a / Å [a]	4.0
$^{298}D / 10^{-5}\ cm^2\ s^{-1}$ [a]	3.1

Table 5.3: Best-fit parameters obtained from the analysis of ^{1}H NMRD profiles of Gd_4L^{IV}-DSPE-PEG2000 20:80.

DLS analysis of the **Gd_4L^{IV}-DSPE-PEG2000 20:80** mixed micelles suspension was also performed, defining a particles dimension of 13.3 nm, as showed in Figure 5.18.

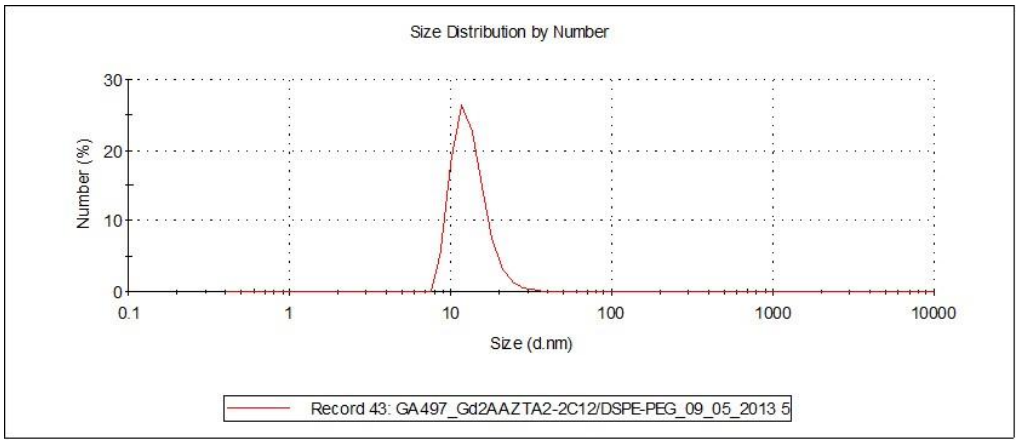

Figure 5.18: DLS analysis of the Gd_4L^{IV}-DSPE-PEG2000 20:80 suspension.

As last system presented in this work, the preparation of a liposome made of **Gd_4L^{IV}**, DSPE-PEG2000 and 1,2-dipalmitoyl-sn-glycero-3-phosphocholine (DPPC) in 20:5:25 ratio was carried out.

After preparation of the lipidic film and drying, the rehydrated film (using HEPES buffer) was extruded using first a 400 µm and then a 200 µm membrane, obtaining the final liposomal suspension. The NMRD profiles were measured, obtaining a r_{1p} value of 33.2 mM^{-1} s^{-1} at 310 K and 20 MHz (Figure 5.19), higher than that of the self-aggregated and mixed micelles, as showed in Figure 5.20.

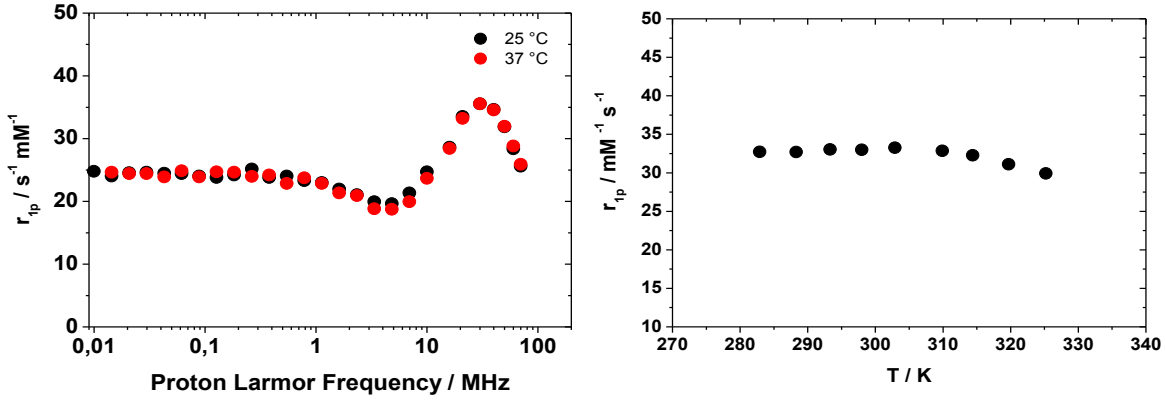

Figure 5.19: left) NMRD profile of the Gd_4L^{IV}-DSPE-PEG2000-DPPC 20:5:75 liposomes, 298 K and [Gd] = 1.34 mM; right) r_{1p} as a function of temperature, measured at 20 MHz.

r_{1p} as a function of temperature doesn't highlight any significant modification at variation of the temperature. However, in case of liposomes, typically half of the amphiphilic complexes point to the internal aqueous core and do not contribute to the overall relaxivity in the same amount that the complexes pointing outwards. The basic concept is that the Gd-complexes exposed on the external leaflet of the bilayer directly affect the nuclear magnetic relaxation rate of the bulk water protons, which are by far the predominant fraction of water in the liposomal suspension (>98% under the experimental conditions used). The relaxivity contribution of the complexes facing the internal aqueous core depends largely by the water permeability of the phospholipidic membrane. Being the water permeability directly proportional to the temperature, the contribution of the internal complexes should increase with the temperature. This could be the reason of the r_{1p} vs temperature trend of **Gd_4L^{IV}-DSPE-PEG2000-DPPC** liposomes.

Also a DLS analysis of the liposomal suspension was performed, defining a liposomes diameter of 100 nm (Figure 5.20).

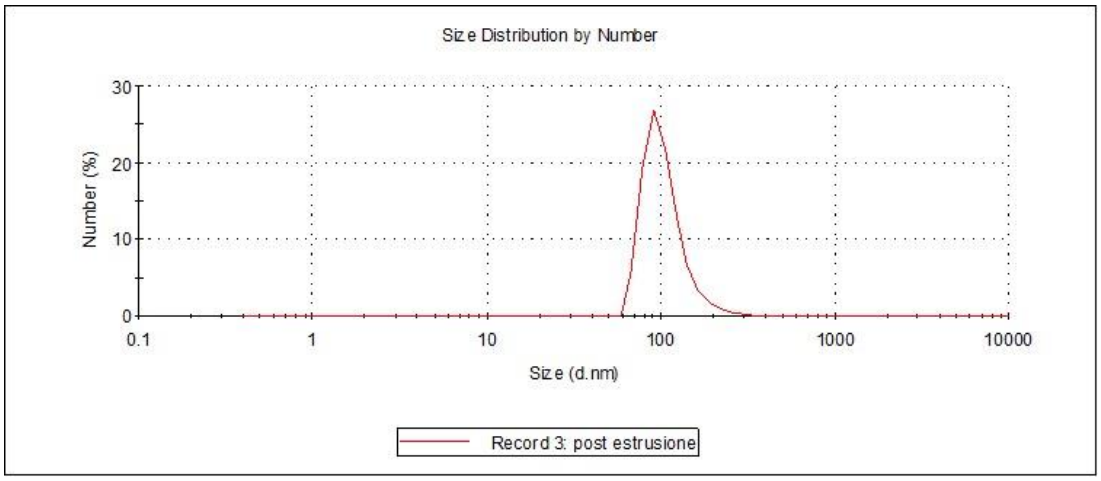

Figure 5.20: DLS analysis of the Gd_4L^{IV}-DSPE-PEG2000-DPPC 20:5:75 liposomes suspension.

5.3 Conclusions

In the literature there are only few examples of aggregated systems based on amphiphilic Gd^{3+} complexes with two coordinated water molecules, being Gd-AAZTAC17 one of them[ref]. Interestingly, the r_{1p} value for **GdL^{I}** at 20 MHz and 310 K is slightly higher than that reported for GdAAZTAC17 and almost double if compared with q = 1 systems.[3,4,5] High r_{1p} values were obtained also embedding **Gd_4L^{IV}** in liposomes, much higher than those observed for systems incorporating q = 1 complexes such as Gd-DOTAGAC12. The reason of this remarkable increase of relaxivity is mainly due to the presence of two coordinated water molecules and to their high rate of water exchange. The effects of the use of multimeric systems and of the increased local rigidity expected by using the double aliphatic chains

functionalization are less pronounced. A further, significant increase of r_{1p} requires a more detailed study on the dynamics of these systems and its dependence on the details of the molecular structure.

5.4 Experimental part

Synthesis of VII

A solution of AAZTA-OH (350 mg; 0.582 mmol) in dry CH_2Cl_2 (5 mL) was added under N_2 to a solution of p-nitrophenylisocyanate (115 mg; 0.699 mmol) in dry CH_2Cl_2 (5 mL). The reaction mixture was stirred for 2 hours at room temperature and then evaporated in vacuo. The crude product was purified on silica gel chromatography column (petroleum ether/ethyl acetate 8/2) yielding 1 as pale yellow solid (428 mg; 96%). TLC (silica gel 60 F254, petroleum ether/EtOAc 8 : 2, detection: UV 254 nm): Rf=0.45. ^{1}H-NMR ($CDCl_3$) 500 MHz d = 8.53 (bs, 1H, NH), 8.12 (d, 2H, J = 9.2 Hz, CH), 7.57 (m, 2H, CH), 4.21 (s, 2H, CH_2OCO), 3.65 (s, 4H, CH_2CO), 3.22 (s, 4H, CH_2CO), 3.05 (d, 2H, J = 14.3 Hz, CH_2C), 2.76–2.65 (m, 6H, CH_{2cycl}), 1.40 (s, 18H, CH_3), 1.39 (s, 18H, CH_3). ^{13}C-NMR ($CDCl_3$) 125 MHz d = 172.8, 170.7 (CO), 153.1 (NHCOO), 144.7, 142.7 (C), 125.2, 117.7 (CH), 81.0, 80.9 (CCH_3), 68.0 (CH_2OCO), 63.3 (C), 62.0, 60.4 (CH_2CO), 59.1, 51.8 (CH_{2cycl}), 28.2, 28.1 (CH_3). ESI-MS$^+$ (m/z): 766.55 $[M + H]^+$; calc for $C_{37}H_{60}N5O_{12}$: 766.42.

Synthesis of VIII

A suspension of 10% Pd/C (70 mg) in water (1 mL) was added to a solution of **VII** (115 mg; 0.15 mmol) in MeOH (10 mL). The mixture, under H_2 atmosphere, was stirred for 3 hours and then filtered over celite. The filtrate was evaporated in vacuo affording pure 2 (103 mg; 93%). TLC (silica gel 60 F254, petroleum ether/EtOAc 8 : 2, detection: UV 254 nm): Rf=0.13.^{1}H-NMR ($CDCl_3$) 500 MHz d = 7.22 (s, 2H, J = 5.9 Hz, CH), 6.64 (d, 2H, J = 5.9 Hz, CH), 4.16 (s, 2H, CH_2OCO), 3.71 (s, 4H, CH_2CO), 3.40 (bs), 2.88 (bs)

(12H, CH_2CO + CH_{2cycl}), 1.43 (s, 36H, CH_3). ^{13}C-NMR ($CDCl_3$) 125 MHz d = 172.7, 170.6 (bs) (CO), 153.6 (NHCOO), 140.0, 130.1 (C), 120.5, 115.7 (CH), 81.2 (bs) (CCH_3), 67.4 (bs) (CH_2OCO), 61.7 (bs), 58.8 (bs), 51.8 (bs) (C, CH_2CO, CH_{2cycl}), 28.2 (CH_3). ESI-MS$^+$ (m/z): 736.25 $[M + H]^+$; calc for $C_{37}H_{62}N_5O_{10}$: 736.45.

Synthesis of IX

A solution of thiosphogene (17 µL; 0.23 mmol) in dry CH_2Cl_2 (2 mL) was added drop wise in 2 minutes to an ice-bath cooled mixture of **VIII** (110 mg; 0.15 mmol) in saturated potassium bicarbonate (5 mL) and CH_2Cl_2 (5 mL), under vigorous magnetic stirring. The ice-bath was removed after 5 minutes and the suspension was stirred for 2 hours at room temperature. The organic phase was separated and extracted with water (3 x 10 mL); then the organic phase was dried over Na_2SO_4, filtered and evaporated to yield a yellow solid. TLC (silica gel 60 F254, petroleum ether/EtOAc 8 : 2, detection: UV 254 nm): Rf=0.41. ^{1}H-NMR ($CDCl_3$) 500 MHz d = 7.41 (bs, 2H, CH), 7.20 (bs, 2H, CH), 7.15 (bs, 1H, NH), 4.20 (s, 2H, CH_2OCO), 3.72 (s, 4H, CH_2CO), 3.21 (s, 4H, CH_2CO), 3.12 (d, 2H, J = 14.3 Hz, CH_2C), 2.87 (d, 2H, J = 14.3 Hz, CH_2C), 2.70–2.64 (m, 4H, CH_2CH_2), 1.44 (s, 18H, CH_3), 1.43 (s, 18H, CH3). ^{13}C-NMR ($CDCl_3$) 125 MHz d = 172.9, 170.4 (CO), 153.3 (NHCOO), 140.0 (C), 128.0 (C), 110.3 (CH), 106.7 (CH), 81.4, 81.2 (CCH_3), 67.6 (CH_2OCO), 63.4 (C), 62.2, 62.3 (CH_2CO), 59.0, 51.6 (CH_{2cycl}), 28.2, 28.0 (CH_3). ESI-MS$^+$ (m/z): 778.47 $[M + H]^+$; calc for $C_{38}H_{60}N_5O_{10}S$: 778.41.

Synthesis of X

A solution of **IX** (45 mg; 0.058 mmol) in dry CH_2Cl_2 (3 mL) was added under N_2 to a solution of dodecylamine (53 µL; 0.231 mmol) in dry CH_2Cl_2 (2 mL). The reaction mixture was stirred for overnight at room temperature and then evaporated in vacuo. The crude product was purified on silica gel chromatography column (petroleum ether/ethyl acetate 7/3) yielding 1 as pale yellow solid (50 mg; 90%). TLC (silica gel 60 F254, petroleum ether/EtOAc 7 : 3, detection: UV 254 nm): Rf=0.20. ^{1}H-NMR ($CDCl_3$) 500 MHz d = 7.41 (bs, 2H, CH), 7.20 (bs, 2H, CH), 7.15 (bs, 1H, NH), 4.20 (s,

2H, CH_2OCO), 3.72 (s, 4H, CH_2CO), 3.21 (s, 4H, CH_2CO), 3.12 (d, 2H, J = 14.3 Hz, CH_2C), 2.87 (d, 2H, J = 14.3 Hz, CH_2C), 2.70–2.64 (m, 4H, CH_2CH_2), 1.44 (s, 18H, CH_3), 1.43 (s, 18H, CH3). ^{13}C-NMR ($CDCl_3$) 125 MHz d = 172.9, 170.4 (CO), 153.3 (NHCOO), 140.0 (C), 128.0 (C), 110.3 (CH), 106.7 (CH), 81.4, 81.2 (CCH_3), 67.6 (CH_2OCO), 63.4 (C), 62.2, 62.3 (CH_2CO), 59.0, 51.6 (CH_{2cycl}), 28.2, 28.0 (CH_3). ESI-MS$^+$ (m/z): 965.62 [M + H]$^+$; calc for $C_{38}H_{60}N_5O_{10}S$: 965.91.

References

1) S. Aime, L. Calabi, C. Cavallotti, E. Gianolio, G. B. Giovenzana, P. Losi, A. Maiocchi, G. Palmisano, M. Sisti, *Inorg. Chem.*, 2004, *43*, 7588 – 7590.

2) Gianolio E, Giovenzana GB, Longo D, Longo I, Menegotto I, Aime S, Chem. Eur. J. 2007, 13, 5785 – 5797

3) A. Accardo, D. Tesauro, L. Aloj, C. Perdone, G. Morelli, Coord. Chem. Rev. 253, 2009, 2193-2213.

4) W. J. M. Mulder, G. J. Strijkers, G. A. F. Van Tilborg, A. W. Griffioen, K. Nicolay, NMR Biomed. 2006, 19, 142–164.

5) F. Kielar, L. Tei, E. Terreno, M. Botta, J. Am. Chem. Soc., 2010, 132, 7836-7837.